

ANNUAL REPORT 2017

INSTITUTE OF ION BEAM PHYSICS
AND MATERIALS RESEARCH

hzdr



HELMHOLTZ
ZENTRUM DRESDEN
ROSSENDORF

Wissenschaftlich-Technische Berichte
HZDR-084

Annual Report 2017

**Institute of Ion Beam Physics
and Materials Research**

Editors

J. Fassbender, V. Heera,
M. Helm, P. Zahn

HZDR

 **HELMHOLTZ**
ZENTRUM DRESDEN
ROSSENDORF

Cover Picture

The cover picture shows a schematic of a novel antiferromagnetic memory cell. The non-volatile information in the cell can be written very energy efficiently by applying a gate voltage pulse across the insulating antiferromagnet. The information persists as a dominance of one of the two magnetic domain types, red and green areas, respectively. The read-out of the stored information is performed by a 4-point resistance measurement in the top electrode, the grey area with the golden contact pads. Typical thicknesses of the used antiferromagnetic thin films are around 100 nanometers.

Image: © HZDR / S. Mönnich (designXpress dresden)

For further information see:

T. Kosub et al., Nature Communications **8**, 13985 (2017),
reprinted at pp. 16 – 22 of this Annual Report.

Many thanks for providing material and for technical assistance to: S. Gebel, S. Kirch,
J. v. Borany, P. Michel, and T. Kosub.

Print edition: ISSN 2191-8708

Electronic edition: ISSN 2191-8716

The electronic edition is published under Creative Commons License (CC BY-NC-ND 4.0):

[urn:nbn:de:bsz:d120-qucosa-235191](https://nbn-resolving.org/urn:nbn:de:bsz:d120-qucosa-235191)

www.hzdr.de/publications/Publ-27381

Published by Helmholtz-Zentrum Dresden - Rossendorf e.V.

This report is also available at <https://www.hzdr.de/FWI>.

Helmholtz-Zentrum Dresden - Rossendorf e.V.

Institute of Ion Beam Physics and Materials Research

Bautzner Landstraße 400

01328 Dresden

Germany

Directors

Prof. Dr. M. Helm

Prof. Dr. J. Fassbender

Phone

+ 49 (351) 260 2260

+ 49 (351) 260 3096

Fax

+ 49 (351) 260 3285

+ 49 (351) 260 3285

Email

m.helm@hzdr.de

j.fassbender@hzdr.de

www.hzdr.de/FWI

Preface by the directors

After one year without any evaluation-related activities, the year 2017 was again devoted to the preparation of an important evaluation in the framework of the Helmholtz Programme-Oriented Funding (POF). This was due to a change in the evaluation procedure decided by the Federal Ministry of Education and Research (BMBF) and the Helmholtz Association. From now on, the achievements of the individual “Research Units” (in our case: Institutes) are assessed within the running POF period; approximately two years later, towards the end of the POF period, there will be a strategic evaluation of the Research Programmes jointly for all participating Centers. This goes together with an extension of the POF funding period from 5 to 7 years. Although this implies a quite heavy preparation load at present, it may relieve us in the future from excessive administrative work. In any case, the evaluation finally took place in January 2018, and although this is already beyond the present reporting period, it is with great pleasure to say that our institute received the grade “outstanding”, the highest out of 7 possible grades. We would like to take this opportunity to thank all members of the institute for their tremendous efforts that have led to this fantastic outcome!

A highlight concerning third-party funding was certainly the granting of the CALIPSOplus project from the EU with a total volume of 10 million Euros. In this project, we are coordinating transnational access, networking, and joint research of all European synchrotron and free-electron laser facilities for the next four years. A number of other significant EU grants as well as more than 10 presently running projects from the German Science Foundation (DFG) – this despite our eligibility restrictions as a member of the Helmholtz Association – complement our success in the acquisition of third-party funding.

Our scientists demonstrated their excellence through a number of recognitions and awards. Dr. Arkady Krasheninnikov received the Research Award 2017 of HZDR for his theoretical work on the interaction of ion beams with two-dimensional materials. Dr. Tobias Kosub received the PhD Award 2017 of HZDR for his thesis “Ferromagnet-Free Magnetoelectric Thin Film Elements”. Finally, Toni Hache was honored with the Georg-Simon-Ohm Award 2018 of the German Physical Society (DPG) for his Master Thesis on the “Fabrication and Characterization of Spin-Hall-Effect based Nano-Microwave Oscillators”. We sincerely congratulate all prize winners!

The 22nd International Workshop on Inelastic Ion Surface Collisions organized by Dr. Stefan Facsko and colleagues from our Ion Beam Center has been a great success gathering 78 participants from 18 countries to discuss recent developments in the physics of ion surface interaction. For the first time in this series, a summer school preceded the workshop where 12 students from 8 countries followed tutorials on ion beam physics complemented by hands-on experience in ion beam analysis.

The so-called “High-Potential Programme”, initiated by the HZDR Board of Directors a few years ago to support hiring of high-profile scientists to HZDR, continues to be a great success for our institute: after Dr. Arkady Krasheninnikov and Dr. Denys Makarov (Dr. Tobias Kosub’s supervisor) had been hired in 2015, we attracted Dr. habil. Georgy Astakhov from University of Würzburg, who is well known for his work on defects in SiC for quantum information technology. He will integrate his activities in the Semiconductor Materials Department.

The end of 2017 represents a significant transition point for our ion-beam based semiconductor research. The head of the Semiconductor Materials Department, Dr. Wolfgang Skorupa, has retired after more than 40 years of working at Rossendorf. With nearly 600 entries in ISI Web of Science, he has been the most productive scientist of our institute. We sincerely thank him for his invaluable contributions and wish him all the best for the future! His successor is now Dr. Shengqiang Zhou, who has successfully led a Helmholtz Young Investigator Group at our institute. We wish him good luck and success for this new position!

Finally, we would like to cordially thank all partners, friends, and organizations who supported our progress in 2017. Special thanks are due to the Executive Board of the Helmholtz-Zentrum Dresden-Rossendorf, the Minister of Science and Arts of the Free State of Saxony, and the Ministers of Education and Research, and of Economic Affairs and Energy of the Federal Government of Germany. Numerous partners from universities, industry and research institutes all around the world contributed essentially, and play a crucial role for the further development of the institute. Last but not least, the directors would like to thank again all members of our institute for their efforts and excellent contributions in 2017.



Prof. Manfred Helm



Prof. Jürgen Fassbender

Contents

Selected Publications

Copyright remarks	9
Four-Wave Mixing in Landau-Quantized Graphene	11
König-Otto, J. C.; Wang, Y.; Belyanin, A.; Berger, C.; de Heer, W. A.; Orlita, M.; Pashkin, A.; Schneider, H.; Helm, M.; Winnerl, S.	
Purely Antiferromagnetic Magnetoelectric Random Access Memory	16
Kosub, T.; Kopte, M.; Hühne, R.; Appel, P.; Shields, B.; Maletinsky, P.; Hübner, R.; Liedke, M. O.; Fassbender, J.; Schmidt, O. G.; Makarov, D.	
Interplay between localization and magnetism in (Ga,Mn)As and (In,Mn)As	23
Yuan, Y.; Xu, C.; Hübner, R.; Jakiela, R.; Böttger, R.; Helm, M.; Sawicki, M.; Dietl, T.; Zhou, S.	
Two-dimensional MoS₂ under ion irradiation: from controlled defect production to electronic structure engineering	32
Ghorbani-Asl, M.; Kretschmer, S.; Spearot, D. E.; Krashennnikov, A. V.	
Chemical and Electronic Repair Mechanism of Defects in MoS₂ Monolayers	41
Förster, A.; Gemming, S.; Seifert, G.; Tománek, D.	

Statistics

User facilities and services	51
Ion Beam Center (IBC)	
	51
Free Electron Laser (FELBE)	
	53
Experimental equipment	54
Doctoral training programme	59
Publications and patents	60
Concluded scientific degrees	74
Appointments and honors	76
Invited conference contributions, colloquia, lectures and talks	77
Conferences, workshops, colloquia and seminars	83
Exchange of researchers	88
Projects	90
Organization chart	94
List of personnel	95

A grayscale micrograph showing a cross-section of a biological structure, likely a plant stem or a similar tissue. The image displays concentric layers of cells, with a central circular region containing a smaller, darker circular structure. The overall appearance is that of a highly organized, layered tissue.

Selected Publications


Copyright remarks

The following journal articles are reprinted with kind permission from:

Four-Wave Mixing in Landau-Quantized Graphene

König-Otto, J. C.; Wang, Y.; Belyanin, A.; Berger, C.; de Heer, W. A.; Orlita, M.; Pashkin, A.; Schneider, H.; Helm, M.; Winnerl, S.
Nano Letters Vol. 17, pp. 2184 – 2188
© American Chemical Society 2017
DOI: 10.1021/acs.nanolett.6b04665


Purely Antiferromagnetic Magnetoelectric Random Access Memory

Kosub, T.; Kopte, M.; Hühne, R.; Appel, P.; Shields, B.; Maletinsky, P.; Hübner, R.; Liedke, M. O.; Fassbender, J.; Schmidt, O. G.; Makarov, D.
Nature Communications Vol. 8, 13985
© The Authors 2017
 Creative Commons Attribution 4.0 International License
DOI: 10.1038/ncomms13985

Interplay between localization and magnetism in (Ga,Mn)As and (In,Mn)As

Yuan, Y.; Xu, C.; Hübner, R.; Jakiela, R.; Böttger, R.; Helm, M.; Sawicki, M.; Dietl, T.; Zhou, S.
Physical Review Materials Vol. 1, 054401
© American Physical Society 2017
DOI: 10.1103/PhysRevMaterials.1.054401

Two-dimensional MoS₂ under ion irradiation: from controlled defect production to electronic structure engineering

Ghorbani-Asl, M.; Kretschmer, S.; Spearot, D. E.; Krasheninnikov, A. V.
2D Materials Vol. 4, 025078
© The Authors 2017
 Creative Commons Attribution 3.0 License
DOI: 10.1088/2053-1583/aa6b17

Chemical and Electronic Repair Mechanism of Defects in MoS₂ Monolayers

Förster, A.; Gemming, S.; Seifert, G.; Tománek, D.
ACS Nano Vol. 11, pp. 9989 – 9996
© American Chemical Society 2017
DOI: 10.1021/acsnano.7b04162

Four-Wave Mixing in Landau-Quantized Graphene

Jacob C. König-Otto,^{*,†,‡,§} Yongrui Wang,[§] Alexey Belyanin,[§] Claire Berger,^{||,⊥} Walter A. de Heer,^{||} Milan Orlita,^{#,⊥} Alexej Pashkin,[†] Harald Schneider,[†] Manfred Helm,^{†,‡} and Stephan Winnerl[†]

[†]Helmholtz-Zentrum Dresden-Rossendorf, P.O. Box 510119, 01314 Dresden, Germany

[‡]Technische Universität Dresden, 01062 Dresden, Germany

[§]Texas A&M University, College Station, Texas 77843-4242, United States

^{||}Georgia Institute of Technology, Atlanta, Georgia 30332, United States

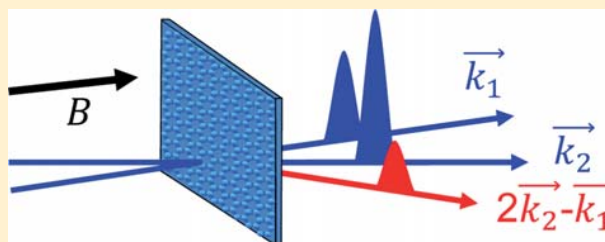
[⊥]Institut Néel, CNRS-Université Alpes, 38042 Grenoble, France

[#]LNCMI, CNRS-UGA-UPS-INSA, 38042 Grenoble, France

[⊥]Institute of Physics, Charles University in Prague, 12116 Prague, Czech Republic

ABSTRACT: For Landau-quantized graphene, featuring an energy spectrum consisting of nonequidistant Landau levels, theory predicts a giant resonantly enhanced optical nonlinearity. We verify the nonlinearity in a time-integrated degenerate four-wave mixing (FWM) experiment in the mid-infrared spectral range, involving the Landau levels LL_{-1} , LL_0 and LL_1 . A rapid dephasing of the optically induced microscopic polarization on a time scale shorter than the pulse duration (~ 4 ps) is observed, while a complementary pump-probe experiment under the same experimental conditions reveals a much longer lifetime of the induced population. The FWM signal shows the expected field dependence with respect to lowest order perturbation theory for low fields. Saturation sets in for fields above ~ 6 kV/cm. Furthermore, the resonant behavior and the order of magnitude of the third-order susceptibility are in agreement with our theoretical calculations.

KEYWORDS: Graphene, four-wave mixing, nonlinear optics, Landau-quantization



Graphene is a two-dimensional material with a gapless linear band structure in the vicinity of two Dirac points. It possesses unique mechanical, electrical, and optical properties, which have led to a high interest in a broad range of fields. An example for those outstanding features are the highly nonlinear optical properties of graphene in a wide spectral range from terahertz (THz) frequencies to visible light. The third-order nonlinear optical response has been investigated theoretically, both on a semiclassical and on a fully quantum mechanical basis.^{1–7} In the latter case, in particular the four-wave mixing (FWM) process is addressed. Experimentally FWM signals have been observed in the near-infrared spectral range^{7–12} and third-order nonlinear susceptibilities have been found to be in the order of $\chi^{(3)} \sim 10^{-25}–10^{-23}$ m³/V². At THz frequencies however, only pump-probe signals, but no FWM signals, have been found.¹³ When a magnetic field is applied perpendicular to the graphene layer the linear dispersion of graphene breaks up into a series of nonequidistant Landau levels.¹⁴ This offers the possibility to resonantly enhance the nonlinear-optical response and to tune the resonance frequency by adjusting the strength of the magnetic field. Recently, a giant nonlinear-optical response ($\chi^{(3)} \sim 10^{-19}$ m³/V²) has been predicted for Landau-quantized graphene.^{15,16} In this Letter, we present the first experimental investigation of this effect by studying transient, degenerate FWM. To this end, the $LL_{-1} \rightarrow LL_0$

and $LL_0 \rightarrow LL_1$ transitions are excited resonantly with radiation at 19 THz (78 meV). The experimental findings are in good agreement with our theoretical calculations based on the density-matrix formalism.

A multilayer epitaxial graphene sample (~ 50 layers) produced by thermal decomposition of SiC on the C-face of 4H-SiC is used in the experiments.¹⁷ Although the amount of graphene layers formed on the SiC substrate is large, the different layers behave like single layer graphene, because they are electronically decoupled.^{18,19} The Fermi level in the different graphene layers is determined by polarization doping of the substrate.²⁰ The majority of layers is slightly n-doped and only the layers at the interface to SiC exhibit a stronger doping²¹ and are therefore transparent at the used photon energy of 78 meV and a magnetic field of 4.5 T. The sample is kept in a split-coil superconducting magneto-cryostat at a temperature of 10 K in a cold helium gas atmosphere. The scheme of the experimental setup is depicted in Figure 1. The laser pulses from the free-electron laser FELBE are split into two separate paths and are focused with an off-axis parabolic mirror onto the sample inside the magneto-cryostat. A time

Received: November 8, 2016

Revised: February 24, 2017

Published: February 24, 2017

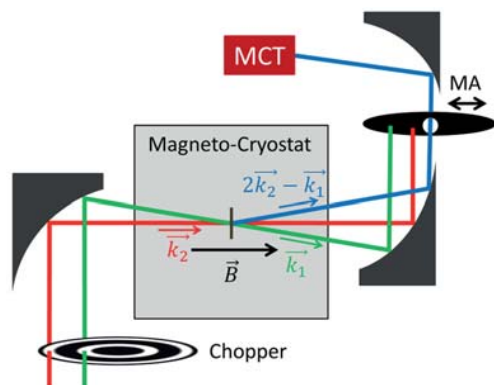


Figure 1. Experimental setup. The movable aperture (MA) is used to select the FWM signal in direction $2\vec{k}_2 - \vec{k}_1$ or to measure a pump–probe signal in \vec{k}_1 direction with the MCT detector.

delay Δt between the two pulses can be controlled with a motorized delay stage (not shown). The beams in direction \vec{k}_1 , \vec{k}_2 and the FWM signal in direction $2\vec{k}_2 - \vec{k}_1$ are simultaneously collimated by a second parabolic mirror. A movable aperture is used to select which beam is detected by the nitrogen cooled mercury–cadmium–telluride (MCT) detector. Both incident beams are modulated by a dual-slot optical chopper and the signals are detected by a lock-in amplifier at the sum of the modulation frequencies for both beams. This enables one to suppress a time-independent background caused by stray light.

If the sample is brought into a magnetic field of around 4.5 T with a direction perpendicular to the surface, the band structure of graphene breaks up into a system of Landau levels and the $LL_{-1} \rightarrow LL_0$ and $LL_0 \rightarrow LL_1$ transitions become resonant with the photon energy of 78 meV. For the almost intrinsic graphene layers LL_{-1} is fully occupied, LL_0 close to half filling and LL_1 is completely empty. In detail, we expect the filling of the zeroth Landau-level to be in the order of 0.52 at this magnetic field (corresponding to a carrier concentration of $8 \times 10^9 \text{ cm}^{-2}$ at zero field²²). In this work, both incident pulses are linearly polarized in the same direction. Thus, the excitation of both transitions is possible as indicated in Figure 2a. The transient change in transmission $\Delta T/T_0$ of the sample due to strong optical excitation is depicted in Figure 2b. For this kind of measurement, the movable aperture is set to transmit the \vec{k}_1 beam and the transient change in transmission of this beam caused by the absorption of photons from the \vec{k}_2 beam is recorded. The pump–probe signal features a fast decay and a slower component in the order of several hundreds of picoseconds. Recent studies already gave first insight into the population dynamics of this system.^{23–26} In particular, a rapid (faster than pulse duration of ~ 4 ps) depopulation of an optically pumped level via Auger scattering has been observed.²⁶ This Coulomb process leads to a fast thermalization of electrons. The slower time scale of the decay is attributed to cooling of the electronic system via phonon scattering.

While the pump–probe signal corresponds mostly to Pauli blocking and reveals the dynamics of the excited population, the FWM signal is sensitive to the induced polarization in the sample. The decay of the microscopic polarization is governed both by the relaxation of the population and by pure dephasing processes. In our FWM experiment, the beam in direction \vec{k}_1 induces a polarization in the sample. The \vec{k}_2 beam, arriving after the delay time Δt , interferes with the remnant \vec{k}_1 polarization

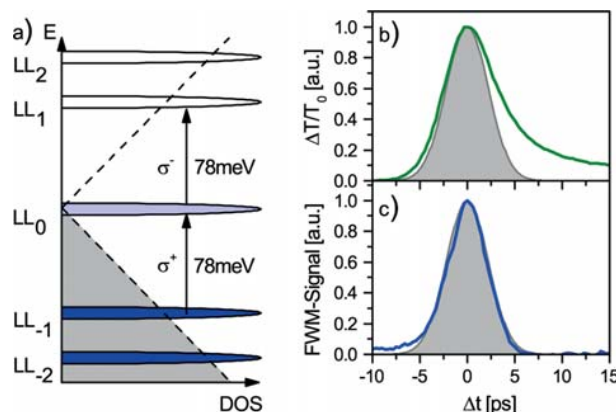


Figure 2. (a) The magnetic field of 4.5 T leads to a Landau-quantization in the graphene sample, whereas the transition from LL_{-1} (LL_0) to LL_0 (LL_1) is resonant to the photon energy of 78 meV. (b) The transient change in population is recorded by a degenerate pump–probe experiment, measuring the transient change of transmission of \vec{k}_1 (field: 6 kV/cm) caused by the absorption of \vec{k}_2 (field: 12 kV/cm). (c) The microscopic polarization is probed by detecting the FWM signal $2\vec{k}_2 - \vec{k}_1$ at the same incident fields. The shaded areas show the autocorrelation of the laser pulses calculated from spectra.

and creates a polarization grating with the wave vector $\vec{k}_2 - \vec{k}_1$. The second part of the \vec{k}_2 beam gets diffracted by this grating in the direction $2\vec{k}_2 - \vec{k}_1$. Thus, the decay time of the FWM signal is defined by the polarization dephasing processes and not by the population decay. Figure 2c depicts the FWM signal at the very same experimental conditions as for the pump–probe signal in Figure 2b. Comparing both types of signals one can see some clear differences. The FWM signal is basically symmetric apart from a small artifact, namely a baseline offset at negative delay times, which stems from pump–probe signals that are scattered as stray light into the detector. Note that the time delay relevant for the FWM signal is inverted with respect to the pump–probe signal.²⁷ The FWM signal is only observed during the temporal overlap of the pulses, indicating that the dephasing time is considerably shorter than the temporal resolution of our experiment set by the pulse duration of around ~ 4 ps. This result, together with the previous detailed study of the population dynamics,²⁶ suggests that Auger processes within the LL_{-1} , LL_0 and LL_1 subset of Landau levels cause a rapid dephasing of the microscopic polarization.

Next, we investigate the dependence of the FWM process on the electric fields of the beams in \vec{k}_1 and \vec{k}_2 direction. The electric field of the generated FWM signal can be estimated from the induced third-order polarization, which depends on the third-order nonlinear surface (2D) susceptibility $\chi^{(3)}$ (in SI units) and is given by

$$|\vec{E}_{\text{FWM}}| \simeq \frac{\omega}{2c} |\chi^{(3)} E^2(\vec{k}_2) E(\vec{k}_1)| \quad (1)$$

Here ω is the frequency, $E(\vec{k}_1)$ and $E(\vec{k}_2)$ the fields of the incident beams, and c is the velocity of light. The surface susceptibility $\chi^{(3)}$ for this process is a function of the magnetic field and the photon energy itself. We will have a closer look on this in the next section. Equation 1 indicates that the FWM field scales linearly with the field of the beam in direction \vec{k}_1 and quadratically with the field of the beam in direction \vec{k}_2 . Thus, if the field of both beams is tuned simultaneously, the FWM field should scale cubically. For a variety of different field

combinations of the two incident beams, FWM transients were recorded and the maxima of the transients were extracted. The incident peak fields were determined from the measured power, spot size and pulse duration. To determine E_{FWM} one has to consider the losses at the movable aperture and the calibration of the MCT detector additionally. Note that the inaccuracy of this procedure has no influence on the determined scaling behavior of the FWM field with respect to the incident fields. The quantitative values of the FWM field, however, are expected to be accurate only within a factor of 3, since the determined FWM intensities are estimated to be accurate within 1 order of magnitude. The FWM peak fields are plotted in Figure 3 as a function of the peak field of the beam in \vec{k}_2

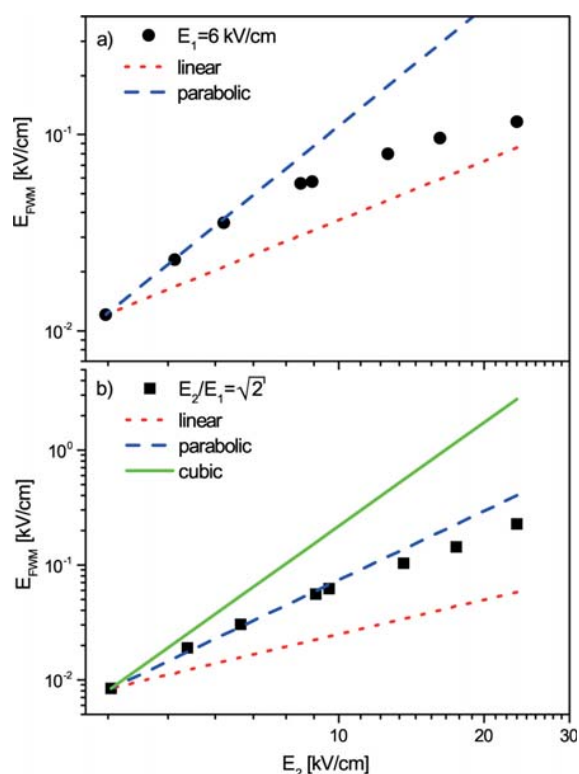


Figure 3. Saturation behavior of the FWM signal. (a) The field of beam one is kept at 6 kV/cm, while the field from beam two is varied. (b) Both fields are varied while keeping a constant ratio of $\sqrt{2}$.

direction. Figure 3a shows the field dependence when the field of the \vec{k}_1 beam is kept constant at 6 kV/cm (corresponding to a fluence of $\sim 0.2 \mu\text{J}/\text{cm}^2$) and only the field of the \vec{k}_2 beam is varied. Linear and quadratic power laws are indicated by the dotted red and blue dashed line, respectively. The three lowest data points are in agreement with a quadratic dependence. Note that in the case of a pump–probe signal one would only expect a linear scaling of the signal. This, together with the different temporal shapes of the signals (see Figure 2), allows one to clearly identify the FWM signal and distinguish it from potential stray pump–probe signals. Nevertheless, a clear saturation is noticeable in the measured field regime. A deeper analysis of saturation effects is beyond the scope of this work. However, in ref 16 saturation fields are calculated for FWM processes with a different level scheme in Landau-quantized graphene under continuous excitation. Despite the differences of the processes evaluated in this work and in ref 16, the

reported saturation behavior can serve as an estimation for the order of magnitude of the saturation field. For a magnetic field of 4.5 T and a dephasing time of 190 fs (this value is discussed later in this Letter), the saturation field is in the order of 4 kV/cm, which is consistent with the experiment, where a deviation from the square root dependence is observed for fields higher than 6 kV/cm. Pump–probe measurements under comparable conditions feature a saturation at comparable pumping fields, indicating that the observed saturation in the FWM experiment might be explained due to band filling.

In accord with the consideration that two photons of the beam in \vec{k}_2 direction interact with one photon of the beam in \vec{k}_1 direction, it is reasonable to choose a ratio of the two fields of $E_2/E_1 \approx \sqrt{2}$. The strength of the FWM signal for this constant ratio is depicted Figure 3b. Again the straight lines represent different power laws. The data points do not follow the green line that represents the expected cubic dependence of this case. However, the dependence is found to be superquadratic for the low fields. The observed saturation is not surprising. From Figure 3a, one can see that at the measured fields already the parabolic dependence on E_2 saturates. Saturation naturally occurs faster if both fields are varied. It was not possible to achieve sufficient signal-to-noise ratio at lower fields to clearly demonstrate the cubic dependence.

In the following, the resonant behavior of the FWM signal is studied by measuring transients at different magnetic fields, while keeping the photon energy fixed. In Figure 4 the peak

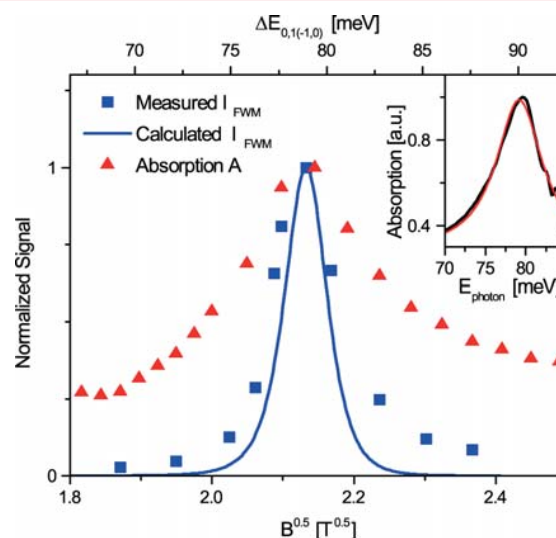


Figure 4. Linear absorption (red triangles) and maxima of FWM mixing signals (blue squares) for different magnetic fields. The field of beam two is 12 kV/cm and beam one 5.3 kV/cm. The blue line shows the calculated magnetic field dependency of the $\chi^{(3)}$ process. The inset shows a Lorentzian fit to the linear absorption spectra at 4.5 T to determine the line broadening.

FWM intensities are plotted on a \sqrt{B} -scale, that is, a scale that is linear in the energy of the optical transition $LL_{-1} \rightarrow LL_0$ and $LL_0 \rightarrow LL_1$.¹⁴ Additionally the linear absorption measured by Fourier transform spectroscopy, as described by Orlita et al. in ref 28, is shown. One can clearly see that the resonance of the $\chi^{(3)}$ process is much narrower as compared to the linear absorption. As mentioned before, the dependence of the FWM signal on the magnetic field stems from the nonlinear

susceptibility $\chi^{(3)}$. We derive an expression for $\chi^{(3)}$ using the density-matrix formalism similarly to refs 15 and 16. Here we only consider transitions that are close to resonance with the pump fields. By using this approximation, the linear and second-order density matrix elements are solely determined by the pump field E_2 , while the field E_1 only enters the third-order density matrix elements. For our specific case, that is, two incident fields with the same linear polarization, and under the assumption of equal line broadening factors for the different transitions, the surface susceptibility can be written as

$$\chi^{(3)}(\omega, 2\vec{k}_2 - \vec{k}_1) = \frac{1}{2\pi l_c^2 \hbar^3 \epsilon_0} \frac{e^4 v_f^4}{\omega \omega_c^3} \frac{i}{\omega + i\gamma - \omega_c} \times \frac{1}{2(2\omega + i\gamma - 2\omega_c)} \frac{(\rho_{-1} - \rho_0) - (\rho_0 - \rho_1)}{\omega + i\gamma - \omega_c} \quad (2)$$

Here v_f is the Fermi velocity in graphene, $\omega_c = v_f \sqrt{\frac{2eB}{\hbar}}$ is the resonance frequency, $l_c = \sqrt{\frac{\hbar}{eB}}$ the magnetic length, ρ_i is the occupation of the LL_i and γ is the line broadening. The numerator of the last fraction is in our case approximately -0.04 , because of the small doping. For intrinsic graphene $\chi^{(3)}$ would vanish in this configuration since contributions from the transitions $LL_{-1} \rightarrow LL_0$ and $LL_0 \rightarrow LL_1$ cancel each other. This reflects electron-hole symmetry of intrinsic graphene. The line broadening for the calculation was taken from the linear absorption measurement by applying a Lorentzian fit to the absorption line (see inset in Figure 4), which yielded $\gamma \simeq 3.5$ meV. Note that this corresponds to a total dephasing time of $\tau = \hbar/\gamma = 190$ fs, assuming a homogeneously broadened line. The fact that the decay of the FWM signal was faster than the pulse duration of 4 ps is consistent with this number. The experimental FWM resonance appears to be slightly broader than the calculated one (see Figure 4). This may have two possible reasons. First, eq 2 does not account for saturation effects. Taking them into account will broaden the calculated peak. Second, in fact, both Landau-level populations and relaxation rates in eq 2 can be viewed as time-dependent during the pulse. An increasing field amplitude of the incident pulse leads to an increase in the amount of nonequilibrium carriers and an accelerated Auger recombination, which has a strongly nonlinear dependence on the nonequilibrium carrier density. These effects contribute to the saturation of the FWM signal strength and an enhanced broadening of the FWM resonance. Furthermore, far away from the resonance the effect of scattered stray light is more dominant, as the pump-probe signal possesses a broader resonance. Consequently, the strength of the experimental FWM signal may be overestimated in the nearly off-resonant case.

It is instructive to compare the dephasing time estimated from the broadening of the LLs to scattering times discussed in literature. The latter are primarily momentum relaxation times obtained from transport measurements. In the simplest approach, the momentum relaxation time τ_m is related to the carrier mobility by the expression²⁹ $\mu = e\tau_m v_f^2/E_f$. From this expression, relaxation times of 4 and 50 fs can be extracted from quantum Hall effect measurements on monolayer graphene on the Si face of SiC and monolayer quasi-free-standing graphene prepared by hydrogen intercalation on the Si face of SiC, respectively.^{30,31} It has been pointed out that the momentum relaxation time can differ, depending on the predominant

scattering mechanism, by a factor of 1–5 from the time constant related to the quantum level broadening.³² Typical values for the level broadening of exfoliated graphene on SiO₂ are in the range from 30–50 fs,³² approximately three times higher values are found in graphene on hBN.³³ The comparably high value of 190 fs for our sample indicates the high structural quality. Finally we note that extremely pure graphene on graphite layers exhibit dephasing times of up to 20 ps.³⁴

Finally, we discuss the strength of the $\chi^{(3)}$ -process. According to eq 2, one layer of graphene with $\rho_0 = 0.52$ in a magnetic field resonant to the photon energy features a surface susceptibility of $4.9 \times 10^{-20} \text{ m}^3/\text{V}^2$. This corresponds to a bulk susceptibility of $1.6 \times 10^{-10} \text{ m}^2/\text{V}^2$, assuming a layer thickness of 0.3 nm. For comparison with the experiment, it is reasonable to select one of the lower excitation data points from Figure 3a, where the saturation is negligible. From the second point, where the incoming fields are set to $E_2 = 4.6$ kV/cm and $E_1 = 5.9$ kV/cm and $E_{\text{FWM}} = 0.023$ kV/cm is measured, we derive $\chi^{(3)} \sim 9.2 \times 10^{-20} \text{ m}^3/\text{V}^2$ using eq 1. Note that the experimental value is not the $\chi^{(3)}$ for one single layer of graphene, as our sample consists of roughly 50 layers. Considering the uncertainty in the experimental determination of E_{FWM} , experiment and theory are in reasonable agreement. For doped graphene, where the zeroth Landau-level is either completely filled or empty at a magnetic field of several Tesla, a much higher susceptibility is expected, as the numerator in eq 2 will be 25 times higher (i.e., $\chi^{(3)} \sim 10^{-18} \text{ m}^3/\text{V}^2$). Considering the small thickness of graphene, this is in fact a strong nonlinearity. The surface susceptibility of Landau-quantized graphene is comparable to the value observed for intersubband transitions in GaAs quantum wells with much larger thickness and 2D electron density. For example, the intersubband transition at 124 meV in a GaAs/AlGaAs superlattice results in $\chi^{(3)} \sim 1.3 \times 10^{-18} \text{ m}^3/\text{V}^2$, which is 3 orders of magnitude larger than the intraband nonlinearity due to nonparabolicity of the wells.³⁵ Coupled-quantum-well structures based on AlInAs/GaInAs are demonstrated with a susceptibility of $\chi^{(3)} \sim 1.4 \times 10^{-20} \text{ m}^3/\text{V}^2$ measured by third-harmonic generation.³⁶ Even higher third-order nonlinearities $\chi^{(3)} \sim 5 \times 10^{-17} \text{ m}^3/\text{V}^2$ are predicted in the THz range by utilizing impurity transitions in GaAs quantum well³⁷ but have not yet been verified experimentally.

In summary, the proposed large third-order nonlinearity in Landau-quantized graphene is experimentally demonstrated for the first time. The order of $\chi^{(3)}$, the resonance behavior, and the field dependencies are in good agreement with our theoretical predictions. Landau-quantized graphene represents a system with a strong optical nonlinearity and offers spectral tunability by variation of the magnetic field. These properties are attractive for a variety of mid-infrared nonlinear optical applications such as frequency multiplication, parametric generation, and sum-frequency generation.

■ AUTHOR INFORMATION

Corresponding Author

*E-mail: j.koenig-otto@hzdr.de.

ORCID

Jacob C. König-Otto: 0000-0002-2470-1261

Notes

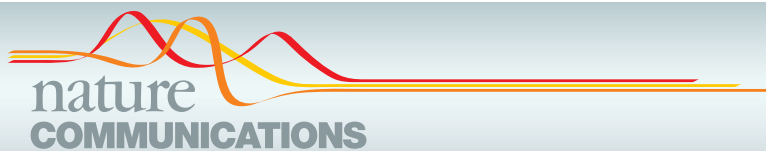
The authors declare no competing financial interest.

■ ACKNOWLEDGMENTS

We thank P. Michel and his team for their dedicated support. This work was financially supported by the SPP 1459 of the DFG and by the EC Graphene Flagship (Project No. 604391).

■ REFERENCES

- (1) Mikhailov, S. A.; Ziegler, K. *J. Phys.: Condens. Matter* **2008**, *20*, 384204.
- (2) Mikhailov, S. A. *Phys. Rev. B: Condens. Matter Mater. Phys.* **2016**, *93*, 085403.
- (3) Cheng, J. L.; Vermeulen, N.; Sipe, J. E. *New J. Phys.* **2014**, *16*, 053014.
- (4) Cheng, J. L.; Vermeulen, N.; Sipe, J. E. *Phys. Rev. B: Condens. Matter Mater. Phys.* **2015**, *91*, 235320.
- (5) Shareef, S.; Ang, Y. S.; Zhang, C. *J. Opt. Soc. Am. B* **2012**, *29*, 274.
- (6) Zhang, Z.; Voss, P. L. *Opt. Lett.* **2011**, *36*, 4569.
- (7) Hendry, E.; Hale, P. J.; Moger, J.; Savchenko, A. K.; Mikhailov, S. A. *Phys. Rev. Lett.* **2010**, *105*, 097401.
- (8) Ciesielski, R.; Comin, A.; Handloser, M.; Donkers, K.; Piredda, G.; Lombardo, A.; Ferrari, A. C.; Hartschuh, A. *Nano Lett.* **2015**, *15*, 4968.
- (9) Rao, S. M.; Lyons, A.; Roger, T.; Clerici, M.; Zheludev, N. I.; Faccio, D. *Sci. Rep.* **2015**, *5*, 15399.
- (10) Xia, C. Q.; Zheng, C.; Fuhrer, M. S.; Palomba, S. *Opt. Lett.* **2016**, *41*, 1122.
- (11) Xu, B.; Martinez, A.; Yamashita, S. *IEEE Photonics Technol. Lett.* **2012**, *24*, 1792.
- (12) Säynätjoki, A.; Karvonen, L.; Riikonen, J.; Kim, W.; Mehravar, S.; Norwood, R. A.; Peyghambarian, N.; Lipsanen, H.; Kieu, K. *ACS Nano* **2013**, *7*, 8441.
- (13) Woerner, M.; Kuehn, W.; Bowlan, P.; Reimann, K.; Elsaesser, T. *New J. Phys.* **2013**, *15*, 025039.
- (14) Goerbig, M. O. *Rev. Mod. Phys.* **2011**, *83*, 1193.
- (15) Yao, X.; Belyanin, A. *Phys. Rev. Lett.* **2012**, *108*, 255503.
- (16) Yao, X.; Belyanin, A. *J. Phys.: Condens. Matter* **2013**, *25*, 054203.
- (17) Berger, C.; Song, Z.; Li, X.; Wu, X.; Brown, N.; Naud, C.; Mayou, D.; Li, T.; Hass, J.; Marchenkov, A. N.; Conrad, E. H.; First, P. N.; de Heer, W. A. *Science* **2006**, *312*, 1191.
- (18) Hass, J.; Varchon, F.; Millán-Otoya, J. E.; Sprinkle, M.; Sharma, N.; de Heer, W. A.; Berger, C.; First, P. N.; Magaud, L.; Conrad, E. H. *Phys. Rev. Lett.* **2008**, *100*, 125504.
- (19) Sprinkle, M.; et al. *Phys. Rev. Lett.* **2009**, *103*, 226803.
- (20) Mammadov, S.; Ristein, J.; Koch, R. J.; Ostler, M.; Raidel, C.; Wanke, M.; Vasiliaskas, R.; Yakimova, R.; Seyller, T. *2D Mater.* **2014**, *1*, 035003.
- (21) Sun, D.; Divin, C. J.; Berger, C.; de Heer, W. A.; First, P. N.; Norris, T. B. *Phys. Rev. Lett.* **2010**, *104*, 136802.
- (22) Suess, R. J.; Winnerl, S.; Schneider, H.; Helm, M.; Berger, C.; de Heer, W. A.; Murphy, T. E.; Mittendorff, M. *ACS Photonics* **2016**, *3*, 1069.
- (23) Mittendorff, M.; Orlita, M.; Potemski, M.; Berger, C.; de Heer, W. A.; Schneider, H.; Helm, M.; Winnerl, S. *New J. Phys.* **2014**, *16*, 123021.
- (24) Plochocka, P.; Kossacki, P.; Golnik, A.; Kazimierczuk, T.; Berger, C.; de Heer, W. A.; Potemski, M. *Phys. Rev. B: Condens. Matter Mater. Phys.* **2009**, *80*, 245415.
- (25) Wendler, F.; Knorr, A.; Malić, E. *Nat. Commun.* **2014**, *5*, 4839.
- (26) Mittendorff, M.; Wendler, F.; Malic, E.; Knorr, A.; Orlita, M.; Potemski, M.; Berger, C.; de Heer, W. A.; Schneider, H.; Helm, M.; Winnerl, S. *Nat. Phys.* **2014**, *11*, 75.
- (27) Yajima, T.; Taira, Y. *J. Phys. Soc. Jpn.* **1979**, *47*, 1620.
- (28) Orlita, M.; Faugeras, C.; Plochocka, P.; Neugebauer, P.; Martinez, G.; Maude, D. K.; Barra, A.-L.; Sprinkle, M.; Berger, C.; de Heer, W. A.; Potemski, M. *Phys. Rev. Lett.* **2008**, *101*, 267601.
- (29) Tan, Y.-W.; Zhang, Y.; Bolotin, K.; Zhao, Y.; Adam, S.; Hwang, E. H.; Das Sarma, S.; Stormer, H. L.; Kim, P. *Phys. Rev. Lett.* **2007**, *99*, 246803.
- (30) Shen, T.; Gu, J. J.; Xu, M.; Wu, Y. Q.; Bolen, M. L.; Capano, M. A.; Engel, L. W.; Ye, P. D. *Appl. Phys. Lett.* **2009**, *95*, 172105.
- (31) Tanabe, S.; Takamura, M.; Harada, Y.; Kageshima, H.; Hibino, H. *Appl. Phys. Express* **2012**, *5*, 125101.
- (32) Hong, X.; Zou, K.; Zhu, J. *Phys. Rev. B: Condens. Matter Mater. Phys.* **2009**, *80*, 241415.
- (33) Dean, C. R.; Young, A. F.; Meric, I.; Lee, C.; Wang, L.; Sorgenfrei, S.; Watanabe, K.; Taniguchi, T.; Kim, P.; Shepard, K. L.; Hone, J. *Nat. Nanotechnol.* **2010**, *5*, 722.
- (34) Neugebauer, P.; Orlita, M.; Faugeras, C.; Barra, A.-L.; Potemski, M. *Phys. Rev. Lett.* **2009**, *103*, 136403.
- (35) Walrod, D.; Auyang, S. Y.; Wolff, P. A.; Sugimoto, M. *Appl. Phys. Lett.* **1991**, *59*, 2932.
- (36) Sirtori, C.; Capasso, F.; Sivco, D. L.; Cho, A. Y. *Phys. Rev. Lett.* **1992**, *68*, 1010.
- (37) Yıldırım, H.; Aslan, B. *Semicond. Sci. Technol.* **2011**, *26*, 08S017.



ARTICLE

Received 16 Jun 2016 | Accepted 16 Nov 2016 | Published 3 Jan 2017

DOI: 10.1038/ncomms13985

OPEN

Purely antiferromagnetic magnetoelectric random access memory

Tobias Kosub^{1,2}, Martin Kopte^{1,2}, Ruben Hühne³, Patrick Appel⁴, Brendan Shields⁴, Patrick Maletinsky⁴, René Hübner², Maciej Oskar Liedke⁵, Jürgen Fassbender², Oliver G. Schmidt¹ & Denys Makarov^{1,2}

Magnetic random access memory schemes employing magnetoelectric coupling to write binary information promise outstanding energy efficiency. We propose and demonstrate a purely antiferromagnetic magnetoelectric random access memory (AF-MERAM) that offers a remarkable 50-fold reduction of the writing threshold compared with ferromagnet-based counterparts, is robust against magnetic disturbances and exhibits no ferromagnetic hysteresis losses. Using the magnetoelectric antiferromagnet Cr_2O_3 , we demonstrate reliable isothermal switching via gate voltage pulses and all-electric readout at room temperature. As no ferromagnetic component is present in the system, the writing magnetic field does not need to be pulsed for readout, allowing permanent magnets to be used. Based on our prototypes, we construct a comprehensive model of the magnetoelectric selection mechanisms in thin films of magnetoelectric antiferromagnets, revealing misfit induced ferrimagnetism as an important factor. Beyond memory applications, the AF-MERAM concept introduces a general all-electric interface for antiferromagnets and should find wide applicability in antiferromagnetic spintronics.

¹Institute for Integrative Nanosciences, Institute for Solid State and Materials Research (IFW Dresden e.V.), 01069 Dresden, Germany. ²Helmholtz-Zentrum Dresden-Rossendorf e.V., Institute of Ion Beam Physics and Materials Research, 01328 Dresden, Germany. ³Institute for Metallic Materials, Institute for Solid State and Materials Research (IFW Dresden e.V.), 01069 Dresden. ⁴Department of Physics, University of Basel, 4056 Basel, Switzerland. ⁵Helmholtz-Zentrum Dresden-Rossendorf e.V., Institute of Radiation Physics, 01328 Dresden, Germany. Correspondence and requests for materials should be addressed to T.K. (email: t.kosub@hzdr.de) or to D.M. (email: d.makarov@hzdr.de).

In the effort to develop low-power data processing and storage devices, nonvolatile random access memory schemes have received considerable attention¹. Magnetic elements such as the magnetic random access memory (MRAM) (Fig. 1a) promise excellent speed, superior rewritability and small footprints, which has led to strong commercial interest in this technology for memory applications. In addition to ferromagnetic MRAM, two complementary approaches have recently emerged for advancing beyond conventional MRAM elements in terms of its writing power and data robustness. On the one hand, switching and reading the antiferromagnetic order parameter of metallic antiferromagnets with charge currents^{2,3} has enabled purely antiferromagnetic MRAM (AF-MRAM), granting superior data stability against large magnetic disturbances and potentially even faster switchability. On the other hand, magnetoelectric random access memory (MERAM) promises energy efficient writing of antiferromagnets, by eliminating the need for charge currents through the memory cell and instead relying on electric field-induced writing. Reading out the antiferromagnetic state from MERAM has presented a challenge to date as magnetoelectric antiferromagnets (for example, BiFeO₃ or Cr₂O₃) are dielectrics. Therefore, the readout signal of MERAM cells is conventionally acquired from a ferromagnet that is coupled with the magnetoelectric antiferromagnet by exchange bias^{4–8}. While ferromagnets enable readability, their presence strongly interferes with the magnetoelectric selection of the antiferromagnetic order parameter⁹. This is related to exchange bias and ferromagnetic hysteresis, both of which need to be overcome in the writing process of MERAM with ferromagnets.

Here we put forth the concept of purely antiferromagnetic MERAM (AF-MERAM) (Fig. 1a), which avoids the issues associated with the presence of ferromagnets by instead using polarizable paramagnets, for example, Pt, to probe the order parameter of the magnetoelectric antiferromagnet. As shown

schematically in Fig. 1b, the prototypical memory cell consists of an active layer of insulating magnetoelectric antiferromagnet, a bottom gate electrode for writing purposes and a top electrode that provides the readout interface via anomalous Hall measurements¹⁰. Using Cr₂O₃ as an AF element, we demonstrate a complete working AF-MERAM cell, proving that this concept yields substantial improvements in terms of magnetoelectric performance over comparable MERAM realizations with ferromagnets. In particular, by removing the ferromagnetic component from MERAM, we reduce the writing threshold by a factor of about 50. These characteristics render AF-MERAM a promising new member to the emerging field of purely antiferromagnetic spintronics^{3,11}. We show the magnetoelectric writing and all-electric reading operations of a cell at room temperature over hundreds of read–write cycles. While nonvolatile solid-state memory is one possible application of AF-MERAM cells, the concept is applicable to other fields of antiferromagnetic spintronics, such as logics, magnonics¹² and material characterization.

Results

Room temperature operation of AF-MERAM. To realize the memory cell, we use an epitaxial layer stack of Pt(20 nm)/ α -Cr₂O₃(200 nm)/Pt(2.5 nm) that is prepared on Al₂O₃(0001) substrates. Similar stacks with α -Cr₂O₃ have been extensively studied in the scope of traditional MERAM elements with ferromagnetic Co layers^{4,5,13–15}. The thicker bottom Pt film serves as the gate electrode and the thin Pt top layer is used to measure the AF order parameter all-electrically via zero-offset anomalous Hall magnetometry¹⁰ (hereafter zero-offset Hall). This readout approach makes use of the uncompensated boundary magnetization of α -Cr₂O₃(0001), which is rigidly coupled to the AF bulk and creates proximity magnetization in the Pt film^{16,17}.

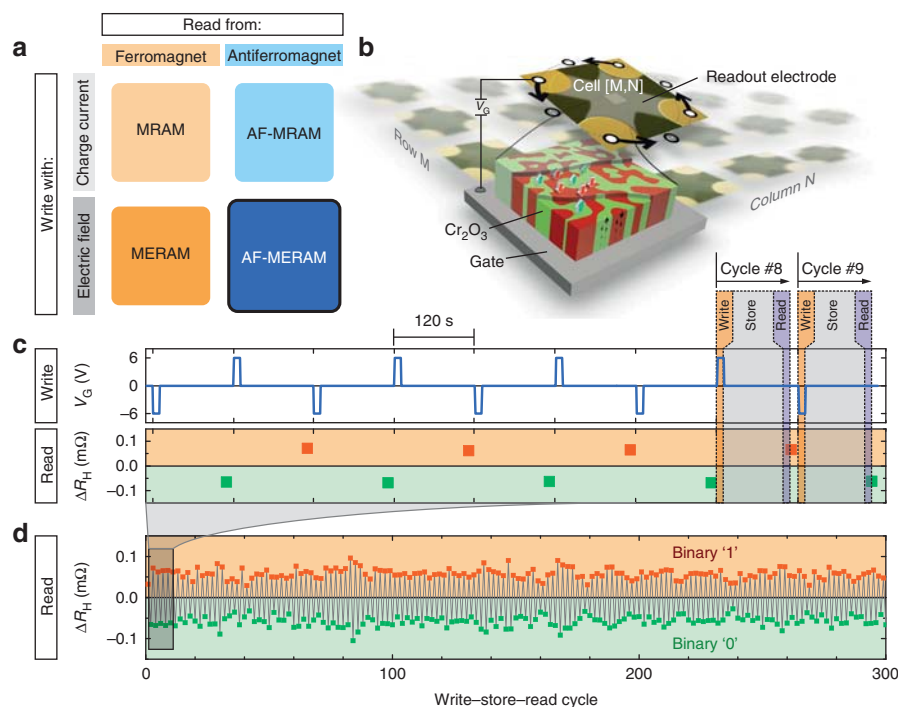


Figure 1 | Electric field-driven manipulation of the antiferromagnetic order parameter. (a) Nonvolatile magnetic random access memory elements categorized according to their writing and readout interfaces. Antiferromagnetic magnetoelectric random access memory (AF-MERAM) initiates a new field of antiferromagnetic spintronics. (b) Sketch of one memory cell within a matrix of devices. The arrows indicate the contact permutation to obtain offset free Hall readings¹⁰. (c) Random access memory operation where binary information is written by a voltage pulse and stored in the antiferromagnetic order parameter. The magnetic state is readout at a later time after the writing stimulus is removed. (d) Device behavior over 300 write–store–read cycles.

An individual magnetoelectric element is obtained by patterning the top Pt layer. Figure 1c shows the protocol of an isothermal magnetoelectric switching experiment that was carried out at 19 °C in a permanent magnetic field of $H \approx +0.5 \text{ MA m}^{-1}$ along the film normal. The test sequence mimics random access operations comprising the three essential elements of any memory cell: writing, storage and reading. One of the key technological advantages is that the memory cell operates in static magnetic fields and writing operations are triggered by the application of a voltage. No energy input is necessary during the storage times. The reproducibility of this process is demonstrated over 300 write–store–read cycles in Fig. 1d, during which the cell reveals no performance degradation.

Two key material requirements must be satisfied to achieve reliable magnetoelectric reversal processes such as shown in Fig. 1. First, the order parameter has to be susceptible to the gate voltage via the linear magnetoelectric effect. Second, the cell has to exhibit thermal stability at the operation temperature, giving rise to stable remanent magnetic states. Both criteria can be directly probed in our system using the electrical writing and reading interfaces of the magnetoelectric cell. To reveal the exact influence of magnetic and electric field on the antiferromagnetic order parameter, it is mandatory to avoid the influence of magnetic anisotropy, which fixes the order parameter while below the ordering temperature, and instead carry out magnetoelectric field cooling through the ordering temperature. The map in Fig. 2a shows the resulting average antiferromagnetic order parameter in the cell after cooling from 30 to 7 °C using the indicated combination of magnetic cooling field H_{cool} and electric cooling field $E_{\text{cool}} = V_{\text{cool}}/t$ (t denotes the AF film thickness). For large EH fields, the order parameter selection is consistent with that expected in $\alpha\text{-Cr}_2\text{O}_3$ (refs 7,13,18,19) due to the linear magnetoelectric effect. However, for small writing voltages that are technologically desirable, the EH symmetry is disturbed, giving rise to magnetic field-induced selection of the order parameter. Strikingly, the EH symmetry is perfectly restored when accounting for a gate bias voltage V_{GB} , which is about -1 V for this system.

When applying a writing voltage to the cell at 19 °C, the antiferromagnetic order parameter can be switched hysteretically with a coercive gate voltage V_C of $\approx 1.5 \text{ V}$ (Fig. 2b), completing the list of ingredients for the nonvolatile AF-MERAM prototype. The slightly asymmetric shape of the hysteresis loop is due to the gate voltage range being symmetric about $V_G = 0$, instead of $V_G = V_{\text{GB}}$. The temperature window, in which magnetoelectric writing can be carried out, is limited at higher temperatures by the collapse of antiferromagnetic order and at lower temperatures by magnetic anisotropy¹⁵. It should be possible to widen this writability window considerably to $>100 \text{ K}$. The high-temperature limit can be enhanced by doping^{20,21}, and the lower-temperature limit by applying higher writing voltages^{4,5} or by intentionally reducing the anisotropy via doping²⁰ (Supplementary Note 1).

Table 1 contains an overview of state-of-the-art studies of magnetoelectric functionality using magnetoelectric thin films^{4–6,9,13} and single crystals⁷, but in both cases relying on interfacial exchange bias with a thin ferromagnetic layer. In addition, the AF-MERAM cell presented in this work is included for comparison. The metrics in the overview are the magnetoelectric film thickness t , the writing threshold $(VH)_C$ and the coercive gate voltage V_C . For integration in microelectronics, the latter two are of particular relevance as the circuit voltage rating depends on them.

While exchange bias has traditionally been used to probe the antiferromagnetic state of Cr_2O_3 , this leads to strongly increased magnetoelectric coercivities, especially for thin films of Cr_2O_3 (refs 4,5). When judging the writing threshold, all the exchange bias systems require very large VH for isothermal magnetoelectric switching of the AF order parameter in Cr_2O_3 . In contrast, the AF-MERAM approach provides a route to reduce both the coercivity and the resulting write voltage by a factor of about 50 over exchange-biased examples (Supplementary Note 2). In addition, AF-MERAM can be readout in permanent external magnetic fields, whereas exchange-biased MERAM requires the removal of the magnetic field for readout. Thus, the example here presented opens an appealing field of AF-MERAM with ultra-low

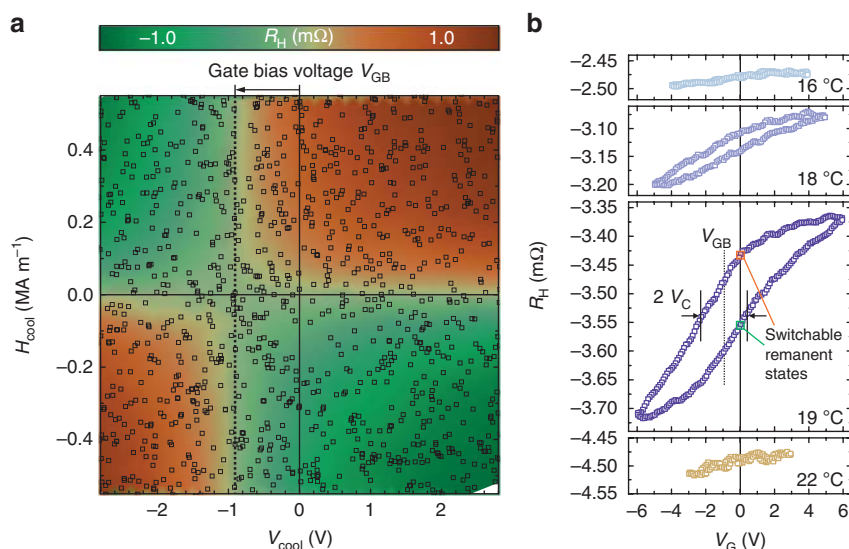


Figure 2 | Isothermal and field-cooled magnetoelectric selection. (a) Map of the antiferromagnetic state selected by a range of magnetic field and gate voltage combinations during cool-down from 30 °C through the antiferromagnetic ordering temperature to the measurement temperature of 7 °C. Measurements were carried out at $H = 0$ and $V_G = 0$. The squares are data points and the background color is a linear interpolation. (b) Readout signal corresponding to the antiferromagnetic order parameter of the cell as a function of the writing voltage V_G for several temperatures near the antiferromagnetic ordering temperature and $H = 0.5 \text{ MA m}^{-1}$. The open hysteresis loop with coercivity V_C gives rise to switchable remanent states.

Table 1 | Performance chart of MERAM systems.

Study	t (μm)	$(VH)_c$ (MW m^{-1})	V_c (V)	Magnetic field
Exchange bias reversal*, $\text{Cr}_2\text{O}_3/\text{Co}/\text{Pd}$ (ref. 7)	1,000	240	450 [†]	Writing pulse
Exchange bias reversal*, $\text{Cr}_2\text{O}_3/\text{Co}/\text{Pt}$ (ref. 5)	0.2	40	56 [†]	Writing pulse
Exchange bias reversal*, $\text{Cr}_2\text{O}_3/\text{Co}/\text{Pt}$ (ref. 4)	0.5	48	105 [†]	Writing pulse
Magnetization switching, $\text{BiFeO}_3/\text{CoFe}$ (ref. 6)	0.1	—	4	Must be ≈ 0 for readout
Magnetization switching, $\text{Cr}_2\text{O}_3/\text{Pt}$ (present work)	0.2	0.75	1.5	Permanent

Overview of state-of-the-art isothermal magnetoelectric switching studies using either the linear magnetoelectric effect in Cr_2O_3 or the multiferroic coupling in BiFeO_3 . The value $(VH)_c$ gives the magnetoelectric writing threshold (product of magnetic field and voltage). The writing voltage V_c allows to qualitatively compare Cr_2O_3 -based systems and BiFeO_3 systems in terms of the voltage at which the magnetization state switches.

*Application of the writing voltage does not switch the ferromagnetic Co, but only the antiferromagnetic Cr_2O_3 , implying that the magnetic field must be removed for readout from the ferromagnet.

[†]For comparability, the writing voltages are calculated for a magnetic field of $H_{\text{write}} = 0.5 \text{ MA m}^{-1}$ as was used in the present study. The actual used writing voltages in these studies are similar to the normalized values, as the magnetic fields were also similar.

writing thresholds and superior stability and readability of the magnetic information in the presence of external magnetic fields.

Discussion

The gate bias voltage of $V_{\text{GB}} \approx -1 \text{ V}$ (Fig. 2) presents a key challenge for achieving ultra-low voltage threshold switching and ultra-high data stability. It has a detrimental effect on both the required writing voltage and on the data stability at zero voltage as the antiferromagnetic state develops a susceptibility to magnetic fields, even in the absence of an electric field ($V_{\text{G}} = 0$). We find that the gate bias voltage is a material characteristic in thin films of magnetoelectric antiferromagnets, and in the following we reveal its physical origin and derive a means to control its value.

When combining the large body of data on Cr_2O_3 thin-film systems^{4,5,7,9,13,15,17,22–29}, a coherent picture emerges: the total magnetoelectric energy density exerting a selection pressure on the antiferromagnetic order parameter in thin-film magnetoelectric antiferromagnets is composed of three effects that act simultaneously:

$$U_{\text{MEAF}}(E, H) = t^{-1}\alpha V_{\text{G}}H + t^{-1}J_{\text{EB}} + t^{-1}\rho_{\text{m}}\mu_0 H \quad (1)$$

The first term describes the linear magnetoelectric effect with its coefficient α reported to be about 1 ps m^{-1} in Cr_2O_3 (refs 18,30). This is the only desired effect in the context of MERAM devices, while the other two effects are parasitic. The second term is the influence of the exchange bias coupling strength J_{EB} on the antiferromagnet. While this term was typically the strongest contribution in previous studies (Supplementary Note 3), it is zero in AF-MERAM due to the lack of a ferromagnet. The last term arises from a non-zero areal magnetic moment density ρ_{m} within the antiferromagnet itself, which renders the material ferrimagnetic. This term, due to emergent ferrimagnetism, cannot be excluded a priori. The gate bias voltage can now be calculated from equation (1):

$$V_{\text{GB}} = -\mu_0 \frac{\rho_{\text{m}}}{\alpha} \quad (2)$$

The gate bias voltage V_{GB} is in an intimate relation with the magnetoelectric coefficient α and the areal magnetic moment density ρ_{m} at the onset temperature of the thermal stability of the antiferromagnetic order. Equation (2) implies that the gate bias in magnetoelectric field cooling experiments vanishes for perfectly antiferromagnetic order ($\rho_{\text{m}} = 0$). Its non-zero value in our system can be used to estimate the approximate ferrimagnetic moment density at the ordering temperature of about 21°C , yielding a value of $\rho_{\text{m}} \approx 0.1 \mu_{\text{B}} \text{ nm}^{-2}$. Conversely, achieving a low gate bias voltage requires that ferrimagnetism is averted.

The presence of ferrimagnetism cannot be accounted for by any intrinsic effect within the Cr_2O_3 antiferromagnetic film, as all

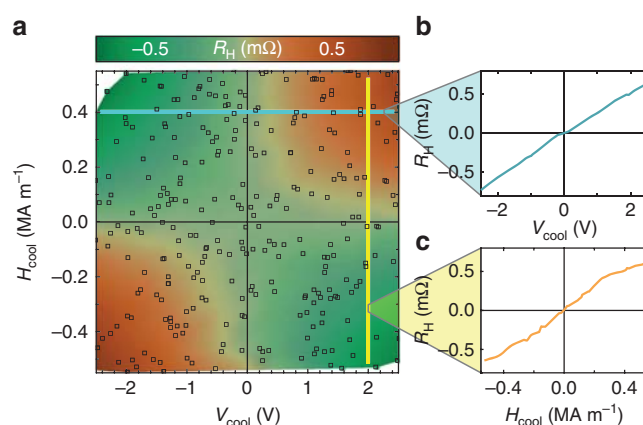


Figure 3 | Influence of a V_2O_3 buffer layer on Cr_2O_3 magnetoelectricity.

(a) Magnetoelectric field cooling map of the antiferromagnetic order selection for a $\text{V}_2\text{O}_3/\text{Cr}_2\text{O}_3/\text{Pt}$ system. (b,c) Line profiles taken from the map in a. Only non-zero products of gate voltage and magnetic field lead to appreciable order parameter selection, whereas the individual stimuli do not.

magnetic moments, including boundary moments^{10,16,17}, are intrinsically compensated when accounting for all boundaries (Supplementary Note 4; Supplementary Fig. 1). Therefore, extrinsic effects are necessary to break the sublattice equivalence and produce ferrimagnetism. In the following, we present an in-depth study of extrinsic thin-film phenomena and their influence on the emergent ferrimagnetism. Namely, we invoke different degrees of crystalline twinning, elastic lattice deformation, intermixing and misfit dislocation density in Cr_2O_3 thin films, by preparing three distinct systems with epitaxial underlayers of $\text{Al}_2\text{O}_3(0001)$, $\text{Pt}(111)$ or $\text{V}_2\text{O}_3(0001)$.

One striking result is that the gate bias voltage, and thus the emergent ferrimagnetism, can indeed be controlled by the choice of underlayer material. In particular, when Cr_2O_3 thin films are grown on a V_2O_3 underlayer, ferrimagnetism is almost entirely eliminated. Figure 3a shows a magnetoelectric field cooling map of the V_2O_3 -buffered system exhibiting virtually perfect EH symmetry. As highlighted by the indicated line profiles (Fig. 3b,c), the selection preference for a particular antiferromagnetic state vanishes when either $E = 0$ or $H = 0$, as expected from the pristine action of the linear magnetoelectric effect (first term in equation (1)). The possibility to completely eliminate the gate bias is highly relevant for AF-MERAM applications, as the AF state can then be switched with lower voltages (Supplementary Note 5; Supplementary Fig. 2) and is completely stable once the gate voltage returns to zero.

Table 2 | Influence of different underlayers on structural and ferrimagnetic properties of Cr₂O₃ thin films.

Underlayer material	Twinning ratio (%)	c axis compression (%)	Expected miscibility	Linear misfit (%)	Areal magnetization ρ_m (a.u.)
Al ₂ O ₃	≈ 2	0.0	weak	+ 4.0	+ 0.455 ± 0.28
Pt	≈ 50	0.18	none	+ 2.8	+ 0.100 ± 0.043
V ₂ O ₃	≈ 2	0.30	strong	- 0.5	- 0.0021 ± 0.001

The values for the structural properties are derived in detail in the (Supplementary Note 6; Supplementary Fig. 3; Supplementary Fig. 4). The ferrimagnetic moment density values are relative values obtained by zero-offset Hall (Supplementary Note 7; Supplementary Fig. 5; Supplementary Fig. 6). They are normalized to the approximate value for Pt/Cr₂O₃/Pt obtained via the gate bias voltage as of equation (2).

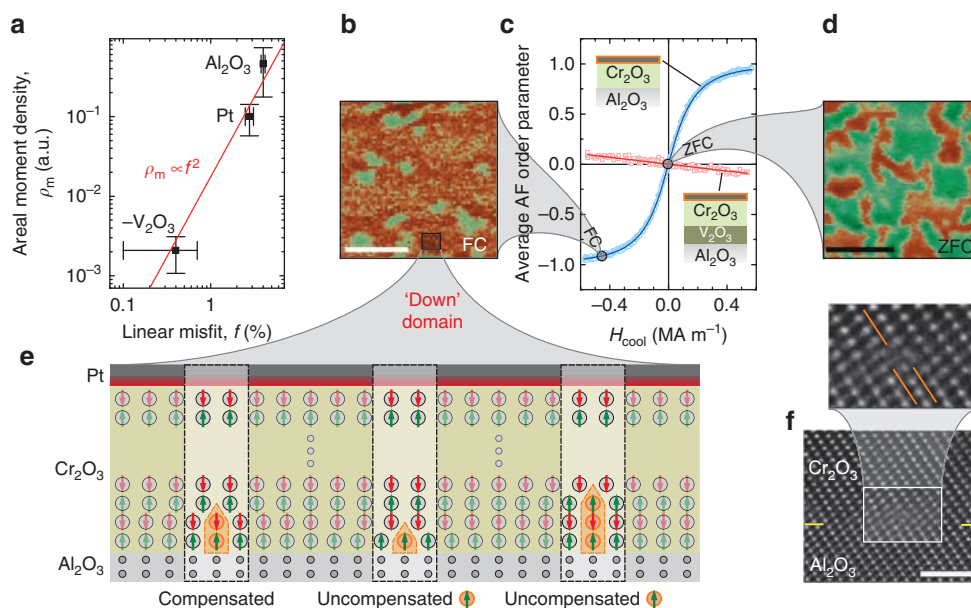


Figure 4 | Thin-film Cr₂O₃ behaves ferrimagnetically. (a) Scaling between the measured areal magnetic moment density and the linear misfit between Cr₂O₃ and its underlayer. Vertical error bars represent s.e.'s based on the best fit values for the domain moment and domain areas (Table 2; Supplementary Note 7). Horizontal error bars show the maximum discrepancy of the lattice misfit values when accounting for only half the thermal expansion of one lattice. (b,d) Images of the surface magnetic stray field after field cooling (FC) and zero-field cooling (ZFC), respectively, were obtained by scanning nitrogen-vacancy microscopy (see text). Scale bars, 1 μm . (c) The emergent ferrimagnetism couples strongly to external magnetic fields and renders the antiferromagnetic order parameter selectable by magnetic fields much smaller than anisotropy fields. (e) Sketch of the effect of different misfit dislocations on the atomic populations of the two antiferromagnetic sublattices. (f) High-resolution TEM images of the Al₂O₃/Cr₂O₃ interface (yellow guide lines) showing complete structural coherence disrupted by occasional misfit dislocations. Scale bar, 2 nm.

To pinpoint the specific extrinsic effect that is responsible for the different degrees of emergent ferrimagnetism in Cr₂O₃ thin films grown on different underlayers, it is instructive to correlate the observed areal magnetic moment density and the various growth-induced effects (Table 2). The areal magnetization is determined via the slope of the dependence of the antiferromagnetic order parameter selection on the magnetic field (Fig. 4c; Supplementary Fig. 5). The gradual shape of these dependences results from a selection tendency of uniaxial antiferromagnetic domains according to their ferrimagnetism, averaged over the readout electrode area. To verify that the microscopic ordering is indeed a mixture of purely uniaxial domains, images of the surface magnetization states after zero-field cooling (Fig. 4d) and field cooling (Fig. 4b) were obtained by scanning nitrogen-vacancy (NV) magnetometry^{31–33}. This technique measures the stray magnetic field $\approx 50\text{nm}$ above the sample surface, clearly indicating the equal presence of up- and down-domains in the zero-field-cooled state. In contrast, field cooling predominantly selects one of the two domain orientations that allows to calculate the degree of ferrimagnetism in the films.

It should also be noted that measuring the gate bias voltage V_{GB} (Equation (2)) provides a second route to quantify the areal magnetization ρ_m absolutely, which is however restricted to conducting underlayers and suffers from the uncertainty of the

value of α . Therefore, magnetization values determined via the gate bias will not be used for the comparison of the different underlayer materials.

Based on these data, we conclude that elastic film strain, twinning and cation intermixing in epitaxial Cr₂O₃ films cannot account for the observed degree of ferrimagnetism, as none of these properties are correlated to the areal magnetization (Table 2). Instead, the results suggest that the lattice mismatch is the cause of the emergent ferrimagnetism.

The scaling relationship between the measured areal magnetic moment density and the linear lattice misfit between Cr₂O₃ and its underlayer is shown in Fig. 4a. When taking into account the data of the three investigated systems, we find that the data align tightly to a quadratic scaling relation (red line). Such a relationship hints at the number of the misfit dislocations per area being the key property determining the areal ferrimagnetic moment density. This result leads to a picture in which the population of the two antiferromagnetic sublattices is unbalanced by the presence of misfit dislocations.

Such dislocations arise due to the heteroepitaxial film growth (Fig. 4f) as the dominant defect type of the otherwise highly coherent interface and appear within the first atomic layers of the Cr₂O₃ film as evidenced by positron annihilation spectroscopy (Supplementary Note 8; Supplementary Fig. 7; Supplementary

ARTICLE

Table 1). As sketched for the case of compressive misfit in Fig. 4e, the dislocations (orange boxes) can contain unequal populations of spin ‘up’ and spin ‘down’ atoms if the dislocation terminates after an odd number of atomic layers. These surplus spins are all aligned within one domain due to the layered sublattice structure in α -Cr₂O₃(0001). While the magnetic moment of atoms near dislocations might be different from atoms in the relaxed lattice, this picture serves to illustrate that misfit dislocations do indeed unbalance the atomic populations in each of the two sublattices.

Remarkably, the lattice misfit not only correlates with the magnitude of the emergent magnetization, but also with its sign with respect to the antiferromagnetic order parameter. This sign change of the ferrimagnetic behavior in the case of tensile misfit for the V₂O₃-buffered sample emerges naturally from the previously introduced picture. Tensile misfit results in atoms being skipped from the bottom boundary sublattice instead of atoms being added. Therefore, tensile misfit results in the top boundary magnetization being aligned along the cooling field, while compressive misfit results in the top boundary magnetization being aligned opposite to the magnetic cooling field.

To quantify ferrimagnetism, we investigate the magnetic field-induced antiferromagnetic order parameter selection with no electric field applied (Fig. 4c), which is influenced exclusively by the last term of equation (1). The Al₂O₃ buffered films are clearly more susceptible to the magnetic field than the V₂O₃-buffered films, which is in line with the substantially larger lattice misfit of the former over the latter. Moreover, a magnetic field of the same sign selects opposite antiferromagnetic states in the two systems, which corresponds to the opposite sign of the lattice misfit.

In conclusion, we demonstrated reliable room temperature magnetoelectric random access memory cells based on a new scheme that relies purely on antiferromagnetic components and does not require a ferromagnet for readout. This AF-MERAM provides substantially reduced writing thresholds over conventional MERAM prototypes, enabling further improvements in the energy efficiency of nonvolatile solid-state memory and logics. Since a permanent magnetic writing field does not interfere with readout in AF-MERAM, this new approach extends voltage driven writing to magnetoelectric antiferromagnets such as Cr₂O₃, whereas such functionality has previously been feasible only in multiferroic antiferromagnets such as BiFeO₃ (Table 1). It should be noted that the advantages of omitting the ferromagnet from MERAM cells likewise apply to multiferroic antiferromagnets, opening an appealing field of AF-MERAM with ultra-low writing thresholds and superior stability of the magnetic order parameter. The concept also provides an important new building block for the emerging field of antiferromagnetic spintronics. While we did not investigate the speed of the actual writing process, first prototypes of conventional MERAM could be switched within a few tens of nanosecond⁵.

We use thin films of magnetoelectric antiferromagnetic Cr₂O₃ as the core material and find that this material becomes ferrimagnetic when grown as epitaxial thin films. Emergent ferrimagnetism in thin films of magnetoelectric antiferromagnets can be desirable³⁴. For the application to purely antiferromagnetic magnetoelectric elements, however, ferrimagnetism should be minimized. Through an in-depth structural characterization, we find that the observed degree of ferrimagnetism is correlated with the square of the linear lattice misfit between Cr₂O₃ and its underlayer. This finding provides both a fundamental mechanism for the phenomenon of emergent ferrimagnetism and suggests a readily available tuning knob to enhance or eliminate the magnetic field coupling of magnetoelectric antiferromagnets.

Methods

Sample preparation. Oxide films were grown by reactive evaporation of the base metal in high vacuum onto *c*-cut sapphire substrates (Crytec GmbH) heated to 700 °C initially and to 500 °C after the first few monolayers. The background gas used was molecular oxygen at a partial pressure of 10⁻⁵ mbar. Chromium was evaporated from a Knudsen cell, vanadium was evaporated from a block target using an electron-beam and platinum was sputtered from a d.c. magnetron source. Deposition of the oxides was carried out using rates of about 0.4 Å s⁻¹ and was monitored *in situ* by reflection high-energy electron diffraction. Oxide layers were subjected to a vacuum annealing process at 750 °C and residual pressure of 10⁻⁷ mbar directly after growth. The thin Pt top layers were deposited at lower temperatures of ≈ 100 °C using a higher rate of 1.0 Å s⁻¹ to maintain layer continuity. Hall crosses were patterned from the top Pt layers, by SF₆ reactive ion etching around a photoresist mask.

Transport experiments. Transport was measured using zero-offset Hall¹⁰. Typical current amplitudes were on the order of 500 μA. RAM operation was carried out in a permanent magnetic background field of $H \approx +0.5 \text{ MA m}^{-1}$ along the film normal.

To obtain the average AF order parameter dependence on the magnetic cooling field, the data of the spontaneous Hall signal after cooling under a range of field values were fitted by an expression that provides the normalization and the absolute magnetic moment distribution of individual domain pieces within the Cr₂O₃ films (Supplementary Note 7). The relative domain sizes of films with different buffer layers were determined using zero-offset Hall by evaluating the statistics of the domain selection within the finite-size Hall crosses (Supplementary Note 7).

The structural properties of the Cr₂O₃ films on different buffer layers were characterized by x-ray diffraction and channeling contrast scanning electron microscopy as shown in detail in (Supplementary Note 6).

NV magnetic microscopy. Scanning NV magnetometry was performed with a tip fabricated from single-crystal, <100>-oriented diamond that was implanted with ¹⁴N ions at 6 keV, and annealed at 800 °C to form NV centres³⁵. An external field of 2.2 kA m⁻¹ was applied along the NV axis (diamond <111> crystal direction) to induce Zeeman splitting of the NV electronic ground-state spin. A microwave driving field was then locked to the spin transition at ≈ 2.864 GHz to track the additional Zeeman shift due to the stray field of the magnetic film surface³⁶. Magnetic field values for each pixel were obtained by averaging the microwave lock frequency for 7 s.

Data availability. The data underlying the present work are available upon request from the corresponding authors.

References

- Yang, J. J., Strukov, D. B. & Stewart, D. R. Memristive devices for computing. *Nat. Nanotechnol.* **8**, 13–24 (2013).
- Jungwirth, T., Marti, X., Wadley, P. & Wunderlich, J. Antiferromagnetic spintronics. *Nat. Nanotechnol.* **11**, 231–241 (2016).
- Wadley, P. *et al.* Electrical switching of an antiferromagnet. *Science* **351**, 587–590 (2016).
- Ashida, T. *et al.* Isothermal electric switching of magnetization in Cr₂O₃/Co thin film system. *Appl. Phys. Lett.* **106**, 132407 (2015).
- Toyoki, K. *et al.* Magnetoelectric switching of perpendicular exchange bias in Pt/Co/α-Cr₂O₃/Pt stacked films. *Appl. Phys. Lett.* **106**, 162404 (2015).
- Heron, J. *et al.* Deterministic switching of ferromagnetism at room temperature using an electric field. *Nature* **516**, 370–373 (2014).
- He, X. *et al.* Robust isothermal electric control of exchange bias at room temperature. *Nat. Mater.* **9**, 579–585 (2010).
- Matsukura, F., Tokura, Y. & Ohno, H. Control of magnetism by electric fields. *Nat. Nanotechnol.* **10**, 209–220 (2015).
- Toyoki, K. *et al.* Switching of perpendicular exchange bias in Pt/Co/α-Cr₂O₃/Pt layered structure using magneto-electric effect. *J. Appl. Phys.* **117**, 17D902 (2015).
- Kosub, T., Kopte, M., Radu, F., Schmidt, O. G. & Makarov, D. All-electric access to the magnetic-field-invariant magnetization of antiferromagnets. *Phys. Rev. Lett.* **115**, 097201 (2015).
- Marti, X. *et al.* Room-temperature antiferromagnetic memory resistor. *Nat. Mater.* **13**, 367–374 (2014).
- Rovillain, P. *et al.* Electric-field control of spin waves at room temperature in multiferroic BiFeO₃. *Nat. Mater.* **9**, 975–979 (2010).
- Ashida, T. *et al.* Observation of magnetoelectric effect in Cr₂O₃/Pt/Co thin film system. *Appl. Phys. Lett.* **104**, 152409 (2014).
- Iwata, N., Kuroda, T. & Yamamoto, H. Mechanism of growth of Cr₂O₃ thin films on (1102), (1120) and (0001) surfaces of sapphire substrates by direct current radio frequency magnetron sputtering. *Jpn. J. Appl. Phys.* **51**, 11PG12 (2012).
- Fallarino, L., Berger, A. & Binek, C. Magnetic field induced switching of the antiferromagnetic order parameter in thin films of magnetoelectric chromia. *Phys. Rev. B* **91**, 054414 (2015).

16. Belashchenko, K. D. Equilibrium magnetization at the boundary of a magnetoelectric antiferromagnet. *Phys. Rev. Lett.* **105**, 147204 (2010).
17. Wu, N. *et al.* Imaging and control of surface magnetization domains in a magnetoelectric antiferromagnet. *Phys. Rev. Lett.* **106**, 087202 (2011).
18. Fiebig, M. Revival of the magnetoelectric effect. *J. Phys. D Appl. Phys.* **38**, R123 (2005).
19. Dzyaloshinskii, I. E. On the magneto-electrical effect in antiferromagnets. *J. Exp. Theor. Phys.* **37**, 881–882 (1959).
20. Mu, S., Wysocki, A. L. & Belashchenko, K. D. Effect of substitutional doping on the Néel temperature of Cr₂O₃. *Phys. Rev. B* **87**, 054435 (2013).
21. Street, M. *et al.* Increasing the Néel temperature of magnetoelectric chromia for voltage-controlled spintronics. *Appl. Phys. Lett.* **104**, 222402 (2014).
22. Shiratsuchi, Y., Fujita, T., Oikawa, H., Noutomi, H. & Nakatani, R. High perpendicular exchange bias with a unique temperature dependence in Pt/Co/ α -Cr₂O₃(0001) thin films. *Appl. Phys. Exp.* **3**, 113001 (2010).
23. Shiratsuchi, Y. *et al.* High-Temperature regeneration of perpendicular exchange bias in a Pt/Co/Pt/ α -Cr₂O₃/Pt thin film system. *Appl. Phys. Exp.* **6**, 123004 (2013).
24. Fallarino, L., Berger, A. & Binek, C. Giant temperature dependence of the spin reversal field in magnetoelectric chromia. *Appl. Phys. Lett.* **104**, 022403 (2014).
25. Nozaki, T. *et al.* Positive exchange bias observed in Pt-inserted Cr₂O₃/Co exchange coupled bilayers. *Appl. Phys. Lett.* **105**, 212406 (2014).
26. Shiratsuchi, Y., Nakatani, T., Kawahara, S. & Nakatani, R. Magnetic coupling at interface of ultrathin Co film and antiferromagnetic Cr₂O₃(0001) film. *J. Appl. Phys.* **106**, 033903 (2009).
27. Lim, S.-H. *et al.* Exchange bias in thin-film (Co/Pt)₃/Cr₂O₃ multilayers. *J. Magn. Magn. Mater.* **321**, 1955–1958 (2009).
28. Sahoo, S. & Binek, C. Piezomagnetism in epitaxial Cr₂O₃ thin films and spintronic applications. *Phil. Mag. Lett.* **87**, 259–268 (2007).
29. Shiratsuchi, Y. *et al.* Detection and *in situ* switching of unreversed interfacial antiferromagnetic spins in a perpendicular-exchange-biased system. *Phys. Rev. Lett.* **109**, 077202 (2012).
30. Folen, V. J., Rado, G. T. & Stalder, E. W. Anisotropy of the magnetoelectric effect in Cr₂O₃. *Phys. Rev. Lett.* **6**, 607–608 (1961).
31. Balasubramanian, G. *et al.* Nanoscale imaging magnetometry with diamond spins under ambient conditions. *Nature* **455**, 648–651 (2008).
32. Maletinsky, P. *et al.* A robust scanning diamond sensor for nanoscale imaging with single nitrogen-vacancy centres. *Nat. Nanotechnol.* **7**, 320–324 (2012).
33. Taylor, J. *et al.* High-sensitivity diamond magnetometer with nanoscale resolution. *Nat. Phys.* **4**, 810–816 (2008).
34. Halley, D. *et al.* Size-induced enhanced magnetoelectric effect and multiferroicity in chromium oxide nanoclusters. *Nat. Commun.* **5**, 3167 (2014).
35. Appel, P. *et al.* Fabrication of all diamond scanning probes for nanoscale magnetometry. *Rev. Sci. Instrum.* **87**, 063703 (2016).
36. Schoenfeld, R. S. & Harneit, W. Real time magnetic field sensing and imaging using a single spin in diamond. *Phys. Rev. Lett.* **106**, 030802 (2011).

Acknowledgements

We acknowledge the support from Dr S. Harazim for the maintenance of the clean room facilities, S. Nestler for conducting the reactive ion etching, M. Bauer for depositing the contact pads, R. Engelhard for the maintenance of the deposition tools and D. Karanushenko and D. D. Karanushenko for providing polyimide photoresist (all IFW Dresden). Support by the Structural Characterization Facilities at IBC of the HZDR is gratefully acknowledged. This work was funded in part by the European Research Council under the European Union's Seventh Framework Programme (FP7/2007-2013)/ERC grant agreement no. 306277 and the European Union Future and Emerging Technologies Programme (FET-Open grant no. 618083).

Author contributions

T.K. prepared the samples. T.K. and M.K. set up the magneto-transport measurement system. T.K. carried out the electrical measurements and the corresponding data analysis. T.K., M.K. and Ru.H. conducted the X-ray diffraction studies. P.A., B.S. and P.M. carried out the NV microscopy measurements. Re.H. imaged cross-sections of the samples in TEM. M.O.L. conducted the positron annihilation spectroscopy (PAS) investigations. T.K. created the graphics and T.K. and D.M. wrote the manuscript with comments from all authors. D.M., O.G.S. and J.F. supervised the project.

Additional information

Supplementary Information accompanies this paper at <http://www.nature.com/naturecommunications>

Competing financial interests: The authors declare no competing financial interests.

Reprints and permission information is available online at <http://npg.nature.com/reprintsandpermissions/>

How to cite this article: Kosub, T. *et al.* Purely antiferromagnetic magnetoelectric random access memory. *Nat. Commun.* **8**, 13985 doi: 10.1038/ncomms13985 (2017).

Publisher's note: Springer Nature remains neutral with regard to jurisdictional claims in published maps and institutional affiliations.



This work is licensed under a Creative Commons Attribution 4.0 International License. The images or other third party material in this article are included in the article's Creative Commons license, unless indicated otherwise in the credit line; if the material is not included under the Creative Commons license, users will need to obtain permission from the license holder to reproduce the material. To view a copy of this license, visit <http://creativecommons.org/licenses/by/4.0/>

© The Author(s) 2017

PHYSICAL REVIEW MATERIALS 1, 054401 (2017)

Interplay between localization and magnetism in (Ga,Mn)As and (In,Mn)AsYe Yuan,^{1,2,*} Chi Xu,^{1,2} René Hübner,¹ Rafal Jakiela,³ Roman Böttger,¹ Manfred Helm,^{1,2} Maciej Sawicki,³ Tomasz Dietl,^{3,4,5} and Shengqiang Zhou¹¹*Helmholtz-Zentrum Dresden-Rossendorf, Institute of Ion Beam Physics and Materials Research, Bautzner Landstrasse 400, D-01328 Dresden, Germany*²*Technische Universität Dresden, D-01062 Dresden, Germany*³*Institute of Physics, Polish Academy of Sciences, Aleja Lotnikow 32/46, PL-02668 Warsaw, Poland*⁴*International Research Centre MagTop, Aleja Lotnikow 32/46, PL-02668 Warsaw, Poland*⁵*WPI-Advanced Institute for Materials Research, Tohoku University, Sendai 980-8577, Japan*

(Received 9 June 2017; published 3 October 2017)

Ion implantation of Mn combined with pulsed laser melting is employed to obtain two representative compounds of dilute ferromagnetic semiconductors (DFSs): Ga_{1-x}Mn_xAs and In_{1-x}Mn_xAs. In contrast to films deposited by the widely used molecular beam epitaxy, neither Mn interstitials nor As antisites are present in samples prepared by the method employed here. Under these conditions the influence of localization on the hole-mediated ferromagnetism is examined in two DFSs with a differing strength of *p-d* coupling. On the insulating side of the transition, ferromagnetic signatures persist to higher temperatures in In_{1-x}Mn_xAs compared to Ga_{1-x}Mn_xAs with the same Mn concentration *x*. This substantiates theoretical suggestions that stronger *p-d* coupling results in an enhanced contribution to localization, which reduces hole-mediated ferromagnetism. Furthermore, the findings support strongly the heterogeneous model of electronic states at the localization boundary and point to the crucial role of weakly localized holes in mediating efficient spin-spin interactions even on the insulator side of the metal-insulator transition.

DOI: [10.1103/PhysRevMaterials.1.054401](https://doi.org/10.1103/PhysRevMaterials.1.054401)**I. INTRODUCTION**

One of the most specific features of magnetic semiconductors is the coexistence of strong exchange coupling effects between carriers and localized spins with intriguing phenomena of quantum localization in disordered systems. These issues are particularly relevant to dilute ferromagnetic semiconductors (DFSs) in which carriers mediate ferromagnetic coupling and, at the same time, are subject to localization [1–14]. The localization in (Ga,Mn)As can be tuned, e.g., by varying Mn concentration [1], by isovalent-anion substitution [15], and by nonmagnetic compensation via codoping [16]. The understanding of the interplay between ferromagnetism and carrier localization remains in a nascent stage and contradicting approaches are under consideration [17–19]. One of the reasons is due to a strong dependence of localization and key magnetic properties on the concentration of poorly controlled donor defects, such as—in the most thoroughly studied system, i.e., (Ga,Mn)As—Mn interstitials [20] and As antisites [21]. Another reason for the slow progress towards a consensus is the intricate nature, even in nonmagnetic semiconductors, of the metal-insulator transition (MIT). In particular, characteristic length scales are too large to allow the MIT to be treated by available *ab initio* methods, whereas theoretical tools, such as the renormalization group formalism, provide merely critical exponents and quantum corrections brought about by diffusion poles, rather than the absolute values of experimentally available quantities [22].

In this paper we present results of systematic charge transport and magnetic studies on a series of Ga_{1-x}Mn_xAs films, together with magnetic investigations on In_{1-x}Mn_xAs layers.

Both kinds of materials are obtained by Mn ion implantation followed by subsequent pulsed laser melting. Neither Mn interstitials nor As antisites are present in samples prepared in this way [23]. Under these rather unique conditions we explore the interplay between magnetism and quantum localization in the Mn concentration range *x* from 0.3 to 1.8%, which covers both sides of the MIT. We demonstrate in a quantitative fashion how the system evolves with *x* from a paramagnetic (PM) phase (probed down to 1.8 K), to a superparamagnetic (SPM) material, to reach, *via* a mixed phase consisting of percolating ferromagnetic clusters and superparamagnetic grains, a global ferromagnetism (FM) without any superparamagnetism. The absence of superparamagnetism for *x* ≥ 1.4% makes our samples, grown by PLM, different from those obtained by molecular beam epitaxy (MBE), in which the measurement procedure employed here reveals often a superparamagnetic component even in films with higher *x* [9,12]. Furthermore, the absence of compensation allows us to determine the hole concentration directly from *x*, which provides a solid ground to test the *p-d* Zener model quantitatively. We find excellent agreement between our experimental data and the theoretical prediction [2]. A worthwhile finding in our work is a clear demonstration that the *p-d* interaction enhances the hole localization and, thus, diminishes hole-mediated coupling. This results in a *weaker* ferromagnetic signature in the range of low Mn concentrations in (Ga,Mn)As compared to (In,Mn)As in which hole localization is weaker.

II. EXPERIMENT

The (Ga,Mn)As and (In,Mn)As samples for this study were prepared by Mn ion implantation into semi-insulating GaAs and intrinsic InAs wafers, respectively, followed by subsequent pulsed laser melting (PLM). The implantation

*y.yuan@hzdr.de

YE YUAN *et al.*

PHYSICAL REVIEW MATERIALS 1, 054401 (2017)

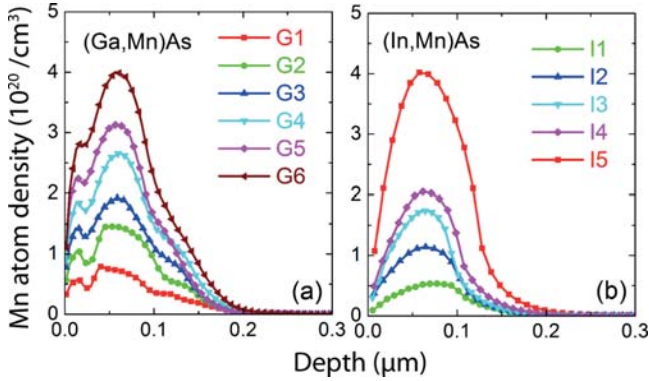


FIG. 1. Concentration profiles of Mn in (Ga,Mn)As and (In,Mn)As determined by SIMS measurements.

energy was 100 keV, and the wafer normal was tilted by 7° with respect to the ion beam to avoid channeling. According to the stopping and range of ions in matter (SRIM) simulation, the longitudinal straggling (ΔR_p) for the Mn distribution in GaAs and InAs is around 31 and 38 nm, respectively. A Coherent XeCl laser (with 308 nm wavelength and 28 ns pulse duration) was employed to recrystallize the samples, and the energy densities were optimized to achieve both the highest crystalline quality and the best randomization of the Mn distribution: 0.3 J/cm^2 for (Ga,Mn)As and 0.2 J/cm^2 for (In,Mn)As [24].

Mn concentration profiles were determined by secondary ions mass spectrometry (SIMS) technique using Cameca IMS 6F microanalyser. SIMS measurement was performed with the cesium (Cs^+) primary beam. Mn concentrations were derived from the intensity of MnCs^+ clusters, as shown in Fig. 1. Since the Mn distribution in both (Ga,Mn)As and (In,Mn)As is approximately Gaussian the Mn concentration relevant for the measured T_C is taken as an average value within the coherence length (which is of the order of 5 nm) in the region around the maximum, as T_C is determined by the peak Mn concentration in the distribution [9,15].

Magnetic properties were studied by employing a Quantum Design MPMS XL Superconducting Quantum Interference Device (SQUID) magnetometer equipped with a low field option. For the thermo-remnant magnetization (TRM—the temperature dependence of the remnant magnetization measured upon warming) measurements, the samples were cooled down under a field of 1 kOe, then at the base temperature the field was switched off using a soft quench of the superconducting magnet and the system was warmed up while collecting data. When above the magnetic critical temperature (T_C —taken here as the temperature where the TRM vanishes), the samples were recooled to the starting temperature at the same zero-field conditions while the data recording was continued and entitled as spontaneous magnetization M_S . All the magnetic measurements were carried out using an about ~ 20 -cm-long silicon strip to fix the samples and the adequate experimental code for minute signal measurements was strictly observed [25]. Temperature-dependent transport measurements were carried out using van der Pauw geometry in a Lakeshore Hall measurement system.

TABLE I. The Mn concentration x , Curie temperature T_C , and characteristic temperatures of ferromagnetic grains T_σ of the $\text{Ga}_{1-x}\text{Mn}_x\text{As}$ samples (denoted by G) and the $\text{In}_{1-x}\text{Mn}_x\text{As}$ samples (denoted by I).

Sample no.	Mn concentration (%)	T_C (T_σ) (K)
G1	0.35	0
G2	0.66	(7.5)
G3	0.87	17 (13)
G4	1.2	31
G5	1.4	44
G6	1.8	60
I1	0.30	0
I2	0.63	(6)
I3	0.96	14 (11)
I4	1.2	23
I5	2.2	40

III. RESULTS AND DISCUSSION

We have prepared both (Ga,Mn)As and (In,Mn)As with very low Mn concentrations, as shown in Table I. As shown in Fig. 2(a), the perfect lattice-fringe image in the cross-sectional high-resolution transmission electron microscopy (HR-TEM) indicates that PLM leads to the complete epitaxial recrystallization of the implanted region even if x is as high as 1.8%. Importantly, for the same sample, a concave curvature of

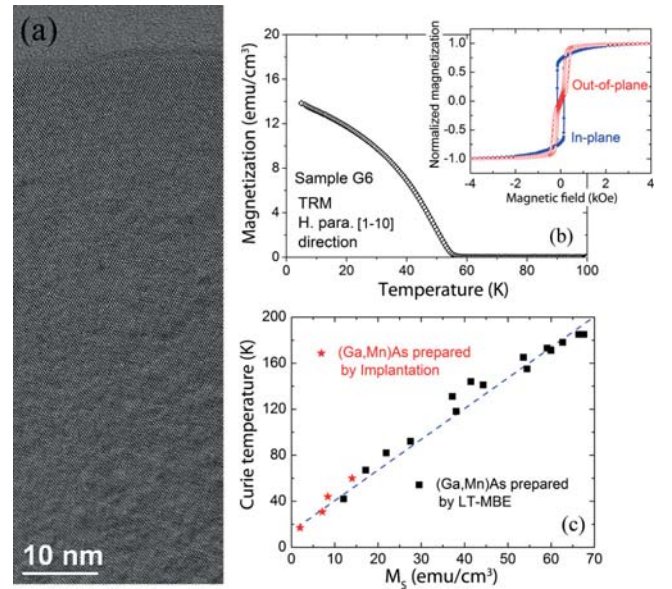


FIG. 2. Structural (a) and magnetic properties (b, c) of (Ga,Mn)As epilayers prepared by ion implantation and PLM. (a) A cross-sectional high-resolution TEM image of the (Ga,Mn)As sample with 1.8% Mn points to high crystalline quality and excludes the presence of any extended lattice defects, amorphous inclusions, and precipitates of other crystalline phases. Temperature dependence of magnetization (b), the character of magnetic anisotropy [inset to (b)], and the magnitude of Curie temperature at given spontaneous magnetization M_S in our (Ga,Mn)As follow the trend established in optimized (Ga,Mn)As films grown by LT-MBE [26].

TRM indicates a nearly mean-field theory behavior, as shown in Fig. 2(b). More convincing evidence to support the epitaxial nature of (Ga,Mn)As on the GaAs substrate is the character of magnetic anisotropy, as shown in the inset of Fig. 2(b). Due to the compressive strain in the (Ga,Mn)As epilayer, an in-plane magnetic easy axis is observed, as expected on the ground of the Zener model and typically observed in (Ga,Mn)As.

The magnitude of Curie temperature (T_C) in (III,Mn)V DSFs is expected to increase with the hole density p and the effective Mn concentration x_{eff} [2]. The value of p is controlled by concentrations of substitutional Mn acceptors and compensating donors. In spatially uniform systems, x_{eff} is directly determined by the spontaneous magnetization M_S , and is typically smaller than x due to antiferromagnetic interactions, for instance, between substitutional and interstitial Mn ions [15,18]. The determined values of x and T_C are summarized in Table I. In order to compare our T_C values to $T_C(M_S)$ obtained for optimized thin MBE (Ga,Mn)As films [26,27] we take $M_S \sim xN_0m_{\text{Mn}}$, where N_0 is the cation concentration and $m_{\text{Mn}} = 4.0 \mu_B$ in the case of weak compensation, small magnitude of the hole orbital moment [28,29], and large spin polarization of the hole liquid. As indicated in Fig. 2(c) our (Ga,Mn)As samples that show FM characteristics follow the $T_C(M_S)$ trend established for thin films obtained by MBE and low-temperature annealing [26].

In doped semiconductors the critical carrier concentration corresponding to the MIT is usually well described by the Mott formula [17,22]:

$$p_c^{\frac{1}{3}} a_B = 0.26 \pm 0.05, \quad (1)$$

$$a_B = \frac{e^2}{8\pi\epsilon_0\epsilon_r E_I}, \quad (2)$$

where a_B is the effective Bohr radius, p_c is the critical hole concentration, e is the charge of single electron, ϵ_r is the static dielectric constant, ϵ_0 is the vacuum permittivity, and E_I is the impurity binding energy. For Mn in GaAs, $\epsilon_r = 12.9$, $E_I = 112.4 \text{ meV}$, thus a critical concentration of p_c ranging from 0.7×10^{20} to $2.4 \times 10^{20} \text{ cm}^{-3}$ is obtained [17,30]. We compare this theoretical value to the hole concentrations in our samples assuming that each substitutional Mn atom delivers one hole, $p \cong xN_0$, where $N_0 = 2.2 \times 10^{22} \text{ cm}^{-3}$ is the cation density in GaAs. The absence of compensation was proved by Rutherford backscattering channelling which showed that (Ga,Mn)As films prepared by ion implantation and PLM are free from Mn interstitial defects [23]. Moreover, owing to the high temperature nature of PLM, the formation of arsenic antisite defects can also be excluded [26]. Under these rather unique conditions we find that the values of p spans from 8.8×10^{19} to $4 \times 10^{20} \text{ cm}^{-3}$ in samples G1 to G6, respectively. This means, in agreement with our resistance measurements discussed below, that our samples are probing both sides of the MIT.

In Fig. 3, solid lines and open circles represent the temperature dependent TRM and sheet resistance, respectively. The resistance in the $G\Omega$ range of sample G1 [Fig. 3(a)] indicates a robust localization of carriers. The conductivity can be described as variable range hopping *via* a Coulomb

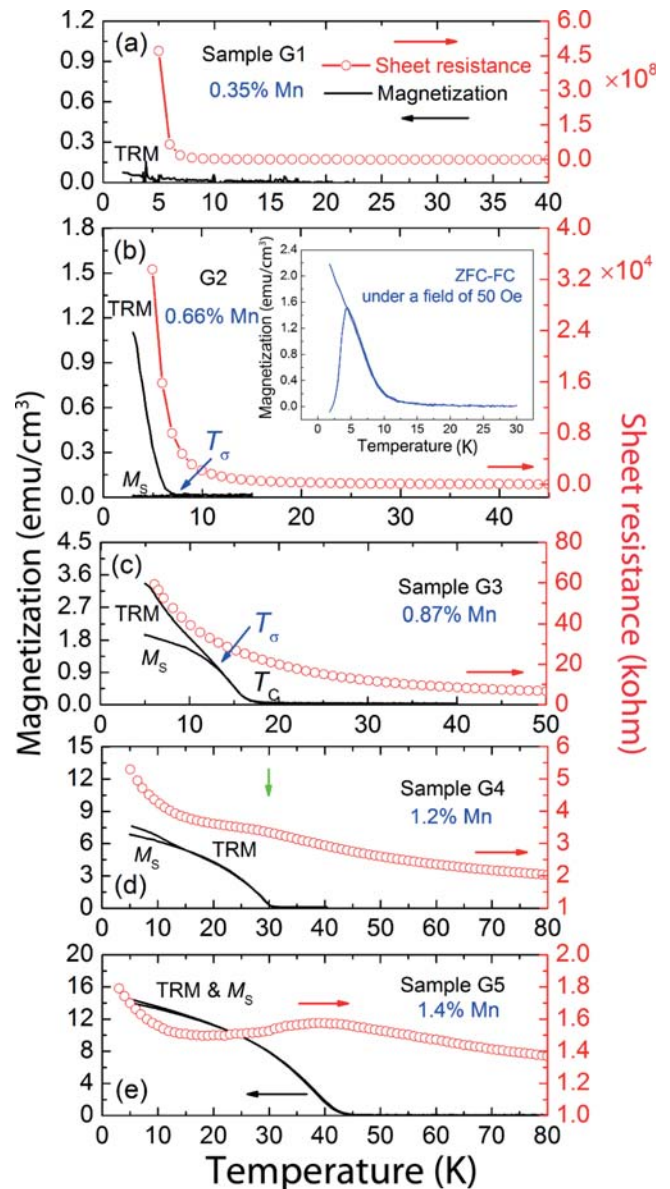


FIG. 3. The interplay between localization and magnetism in (Ga,Mn)As in the vicinity of metal-insulator transition. Temperature dependence of remnant magnetization (lines, left axis) and sheet resistance (circles, right axis) of (Ga,Mn)As (samples G1-G5). The inset to (b) shows ZFC and FC curves for sample G2 in a field of 50 Oe. Upon increasing Mn concentration, together with the emergence of metallic conductivity, differences between spontaneous magnetization (M_S) and thermoremanent magnetization (TRM) get reduced. This indicates that the long-range global ferromagnetic order gradually replaces the mesoscopic ferromagnetic order when hole localization diminishes.

gap [31] with a characteristic energy of 3.4 meV in the whole temperature range, as shown in Fig. 4. There is no detectable remnant magnetization in this sample, indicating that the FM coupling does not develop for such a low x value above 2 K—the sample is in a paramagnetic state.

However, clear indications of FM coupling are seen for the remaining samples with $x \geq 0.66\%$. Namely, all these samples

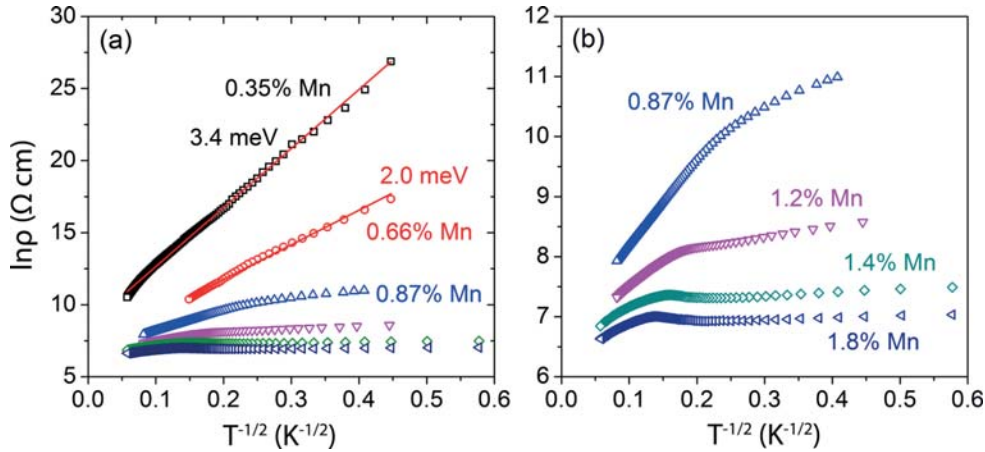


FIG. 4. (a) Temperature dependence of resistivity ρ in (Ga,Mn)As in the absence of an external magnetic field. The results are shown as $\ln(\rho)$ vs $T^{-1/2}$. In samples G1 and G2, the linear dependence dominates across the whole temperature range, supporting the crucial role of hopping mechanism in the electronic transport. However, in other samples with higher Mn concentrations, the conduction mechanism significantly changes, as magnified in (b).

show the existence of TRM, whose thermal properties change significantly with x . In particular, upon increasing x the TRM vanishes at progressively higher temperatures. Furthermore, the TRM curvature changes from a convex for sample G2 with $x = 0.66\%$, through a mixed case for sample G3, to a concave one for larger x . Remarkably, hand in hand with these changes a spontaneous magnetization M_S becomes visible when the sample is cooled back at the same zero-field conditions under which the TRM was measured. This ferromagnetic response M_S : (i) appears on cooling at exactly the same temperature T_C at which the TRM shows up, and (ii) M_S follows the TRM only when the TRM's curvature is concave, otherwise the M_S trails below the TRM. As detailed below, information encoded in TRM and $M_S(T)$ measurements proves sufficient to assess the magnetic constitution of the studied layers.

Sample G2 with $x = 0.66\%$ is the lowest- x layer exhibiting a nonzero TRM. This is indicative that FM coupling is present here, but the rapid increase of the resistivity at low temperatures, despite four orders of magnitude lower values than in sample G1, still points to a sizable localization that precludes a long-range (global) ordering mediated by itinerant holes. Indeed, this is the case—the FM coupling is maintained only over a nanometer-range distance.

To substantiate the claim above we resort to low-temperature sample cycling in a weak field of 50 Oe in the well-established protocol of zero-field cooled (ZFC) and the field cooled (FC) manner. The results presented in the inset to Fig. 3(b) convince us of a granular (nonhomogeneous) magnetic state of this sample, as the magnetic behaviour is typical for blocked SPM ensembles of magnetic particles. In particular, a maximum on the ZFC curve and a clear bifurcation between ZFC and FC data are both seen at nearly the same temperature, corresponding to the (mean) blocking temperature T_B of the ensemble. By using the standard formula for the dynamical blocking, $KV = 25k_B T_B$, where K , the anisotropy constant in (Ga,Mn)As, ranges between 5000 and 50000 erg/cm³ [30], V is the volume of the magnetic particle, k_B is the Boltzmann constant, and the factor 25 is set by the experimental time scale—about 100 s,

in the SQUID magnetometry. This condition implies that $T_B \cong 5$ K corresponds to a sphere of a diameter between 8 to 20 nm, which indeed confirms a mesoscopic extent of FM coupling in this case. Importantly, the appearance of the granular magnetism does not result from nanometer sized Mn aggregates or other types of short scale Mn inhomogeneities, as their presence is excluded by the TEM analyses [see, e.g., Fig. 2(a)]. The presence of magnetic particles is assigned to the fact that according to the Anderson-Mott character of the MIT—occurring primarily due to localization of band carriers by scattering—the carriers' localization radius increases only gradually from the Bohr radius in the strong localization limit, $p \rightarrow 0$, toward infinity at the MIT, $p \rightarrow p_c$ [2,6,17,22]. Thus, a magnetic nanoscale phase separation, driven by carrier density fluctuations, is present in the vicinity of the localization boundary. In such a case FM grains are embedded in the PM host background, as observed experimentally [9,12]. At the same time, the presence of randomly oriented nano-sized magnetic grains gives rise to efficient spin-disorder scattering of carriers. This enhances localization at $B = 0$ and leads to a colossal negative magnetoresistance when a magnetic field is applied to polarize the nanosized ferromagnetic component. Such a colossal negative magnetoresistance has been observed for sample G2 as shown in Fig. 5(a) and also in donor-compensated (Ga,Mn)As MBE films with higher Mn concentrations [1,32].

Due to the absence of a long-range magnetic coupling in sample G2, the concept of a Curie temperature as the temperature of the thermodynamic phase transition is not appropriate. However, from our measurements we can assess a temperature up to which the magnetic particles survive, T_σ . From Fig. 3(b) we get $T_\sigma \cong 7$ K, that is where the TRM vanishes. Finally, we want to point out that no spontaneous moment is observed on cooling at $H = 0$ across T_σ . This is yet another strong indication of the mesoscopic scale of the magnetism in this case. On cooling without an external field the magnetic moments of the grains get blocked in random orientations yielding zero net magnetization, although at the remanence it is considerably larger.

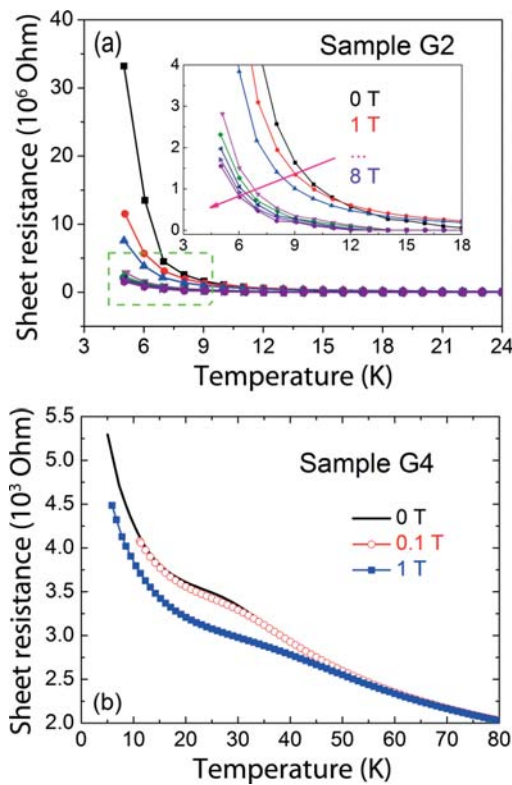


FIG. 5. Temperature- and field- dependent resistance in two (Ga,Mn)As samples. In the superparamagnetic sample G2, the resistance at 5 K gets reduced by 95% in 8 T, and the effect results from the suppression of hole scattering by randomly orientated FM grains and orbital quantum localization effect. In the ferromagnetic sample G4, the critical spin-disorder scattering of itinerant holes by fluctuating Mn spins near T_C disappears when the magnetic field is increased to 1T.

Upon increasing the Mn concentration to 0.87%, the global ferromagnetism with a transition temperature $T_C = 17$ K appears, as indicated in Fig. 3(c). However, a clear gap which opens between the TRM and $M_S(T)$ below T_C , accompanied by a change of the TRM's curvature to a convex one, informs us about the presence of an additional magnetic component possessing similar, superparamagnetic, properties to that observed in sample G2. The value of the TRM- M_S bifurcation temperature, when accompanied by a change to the convex curvature of the TRM, is another practical assessment of T_C .

In contrast, global ferromagnetism without any superparamagnetism is found in sample G4 with 1.2% Mn. This is proven by the overlap of curves corresponding to heating and cooling TRM measurements. In this sample a characteristic hump [1,33] appears in the temperature dependent resistance near $T_C = 30$ K. In DFSs, the hump comes from critical spin-disorder scattering of itinerant holes by fluctuating Mn spins near T_C . Such scattering can be suppressed by an external magnetic field [see Fig. 5(b)]. This sample exhibits a clear increase of the resistivity upon lowering temperature, which points to its insulating character. It means that global FM signatures set in at lower x values, thus at lower hole concentrations than metallic behavior.

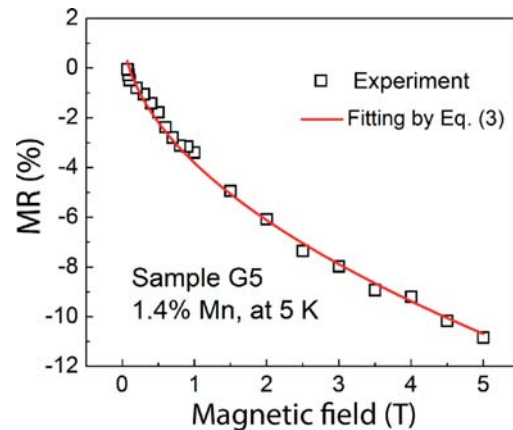


FIG. 6. Quantum localization-induced negative magnetoresistance in metallic (Ga,Mn)As. Negative magnetoresistance is observed at 5 K in sample G5 in the fields in which Mn spins are saturated (open squares). A remarkably good fitting (solid line) suggests that single-carrier orbital weak-localization magnetoresistance dominates at low temperatures.

Both metallic behavior and global ferromagnetism are observed in sample G5 with $x = 1.4\%$. A weak resistance increase at low temperature is related to quantum corrections to conductance on the metallic side of the MIT, associated with disorder-modified carrier-carrier interactions [6,34]. On the other hand, as shown in Fig. 6, the negative magnetoresistance at low temperatures $T \ll T_C$ in this sample can be well fitted within the single-electron quantum localization scenario [35].

$$\frac{\Delta\rho(B)}{\rho_0} \approx -\frac{\Delta\sigma}{\sigma} = -\frac{n_V e^2 C_0 \rho_0 (eB/\hbar)^{\frac{1}{2}}}{2\pi^2 \hbar}, \quad (3)$$

where $C_0 \approx 0.605$, ρ is the resistivity and σ is the electrical conductivity, and $n_V/2$ is the number of spin subbands contributing to charge transport. The fitted value $n_V = 1.6$ indicates that at least three subbands are occupied.

The evolution of magnetism with x , as determined for our samples, is illustrated schematically in Figs. 7(a)–7(d). The normalized magnetization per Mn atom is calculated from the magnetization divided by the integrated number of all Mn atoms in the layer. The magnetization has been measured at 5 K and 2 T to saturate both the SPM and FM components. The results are displayed in Fig. 7(e). They allow us to obtain information on the degree of hole localization and on the relative participation of the ferromagnetic component.

Because of the low Mn and hole concentration $p = 8.8 \times 10^{19} \text{ cm}^{-3}$ only paramagnetism is observed in sample G1 for which the normalized magnetization is determined to be $M = 2.8 \mu_B/\text{Mn}$. This value allows us to find out whether the holes are in the strongly or weakly localized regime in this sample. In the former case, the holes are localized on parent Mn acceptors and the magnetic moment per Mn atom can be calculated from the Brillouin function,

$$M = Jg\mu_B \left[\frac{2J+1}{2J} \coth\left(\frac{2J+1}{2J}x\right) - \frac{1}{2J} \coth\left(\frac{1}{2J}x\right) \right], \quad (4)$$

$$x = \frac{Jg\mu_B H}{k_B T}, \quad (5)$$

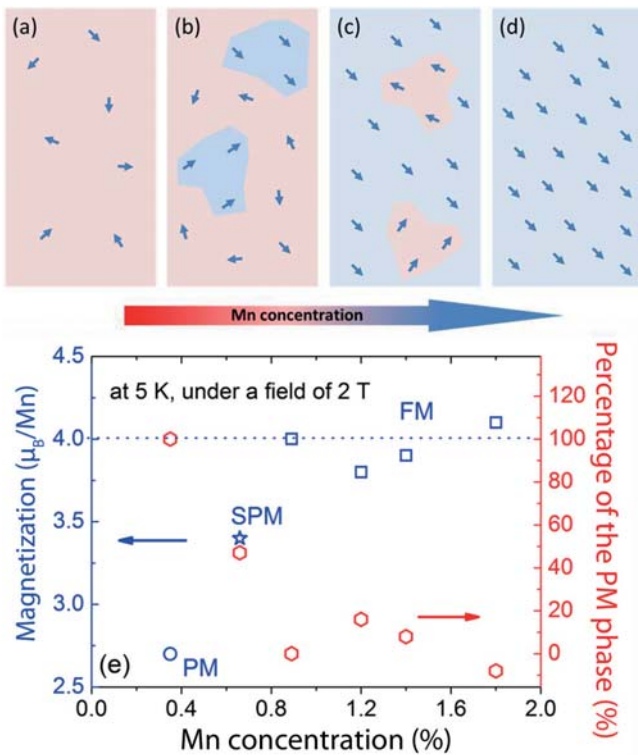
YE YUAN *et al.*

FIG. 7. Descriptions of the transition from the paramagnetic to ferromagnetic phases in (Ga,Mn)As. (a–d) A schematic diagram of the evolution of magnetic order in (Ga,Mn)As with increasing Mn concentration. (e) Mn-concentration dependent magnetization in the paramagnetic (circle), superparamagnetic (star), and ferromagnetic (squares) samples measured under a field of 2 T at 5 K. The normalized magnetization per Mn atom was determined by dividing the magnetization by the total number of Mn ions obtained by integrating the distribution of the Mn concentration.

where $J = 1$ and $g = 2.77$ [36]. This formula leads to $M = 1.6 \mu_B/\text{Mn}$ at 5 K in 2 T, which implies that the model of strong localization is not applicable for this Mn concentration in question. On the other hand, according to Eq. (4) the $M = 2.7 \mu_B$ for $J = 5/2$ and $g = 2.0$, which is close to the established value of $2.8 \mu_B/\text{Mn}$ in sample G1. This is consistent with the fact that in the weakly localized regime, in which holes reside in the valence band, the degree of the hole spin polarization is small, as the Fermi level is about 80 meV below the valence band top whereas the valence band spin splitting is below 12 meV [37].

In the SPM sample G2 $M = 3.4 \mu_B/\text{Mn}$ is obtained, indicating that not all Mn spins contribute to the detectable magnetic moment as depicted in Fig. 7(b). Such a value can be used for quantitatively evaluating the electronic phase separation between the ferromagnetic and paramagnetic phases in this (Ga,Mn)As system. For sample G2, $M = 3.4 \mu_B/\text{Mn}$ implies a mixture of the nanosized hole-rich ferromagnetic phase and the paramagnetic matrix with only very few holes. Therefore, the values of 4 and $2.8 \mu_B/\text{Mn}$ in the ferromagnetic and paramagnetic regions, respectively, can be used to quantitatively calculate the composition of each phase according to $4\mu_B(1 - y) + 2.8\mu_B y = M_{\text{Mn}}$, where

PHYSICAL REVIEW MATERIALS 1, 054401 (2017)

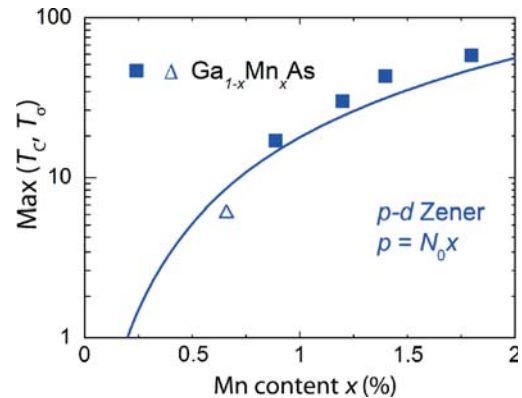


FIG. 8. Curie temperatures T_C (full points) and SP temperatures T_S (empty triangle) in $\text{Ga}_{1-x}\text{Mn}_x\text{As}$. The solid line shows the prediction by the $p-d$ Zener model for $\text{Ga}_{1-x}\text{Mn}_x\text{As}$ assuming the absence of compensating donors. The dependence of the $T_C(T_S)$ on Mn content matches the Zener model prediction for both SPM and FM (Ga,Mn)As samples.

y is the percentage of the paramagnetic phase, i.e., of the component without ferromagnetic coupling, and M is the measured value in Fig. 7(e). As the Mn density increases, the percentage of paramagnetic Mn is gradually decreasing: From 100% in sample G1, through 47% in sample G2, finally gets saturated at around 0% in samples G3–G6. The results correspond to the electronic picture given in Figs. 3 and 7; i.e., the inhomogeneity of the ferromagnetism in the sample in the MIT regime directly comes from the electronic phase separation. Note that, since the implanted Mn atoms are not distributed in a rectangular fashion, but exhibit a Gaussian shape, a tail with lower Mn concentrations always exists in all samples. However, only a small part of the superparamagnetic phase is seen through TRM measurements in the ferromagnetic samples G4 and G5 [see in Figs. 3(d) and 3(e)], indicating the tail with low Mn concentration is negligible.

It is interesting to compare the experimental values of T_C and T_S to the expectations of the $p-d$ Zener model. As shown in Fig. 8, there is good agreement between the measured and computed values for both insulating and metallic samples. This finding substantiates the applicability of the $p-d$ Zener model for the description of ferromagnetism mediated by itinerant holes as well as by weakly localized holes.

The versatility of ion implantation allows us to compare (Ga,Mn)As with (In,Mn)As. Previous studies of (In,Mn)As films obtained by MBE [38,39] and ion implantation [40,41] with relatively large Mn concentrations show lower T_C compared to (Ga,Mn)As, in agreement with theoretical expectations [2,37]. According to our results presented in Fig. 9, an evolution from the paramagnetic phase to the global ferromagnetic state which takes place in (Ga,Mn)As with increasing x is also observed in (In,Mn)As samples obtained by ion implantation and PLM.

Only paramagnetic behaviour is observed in sample I1 with $x = 0.30\%$ like in the (Ga,Mn)As sample with $x = 0.35\%$. In sample I2, both TRM and a bifurcation between ZFC and FC co imply the SPM character, as in the case of sample G2. When the Mn concentration reaches 0.96%, the TRM measurement points to the coexistence of superparamagnetism

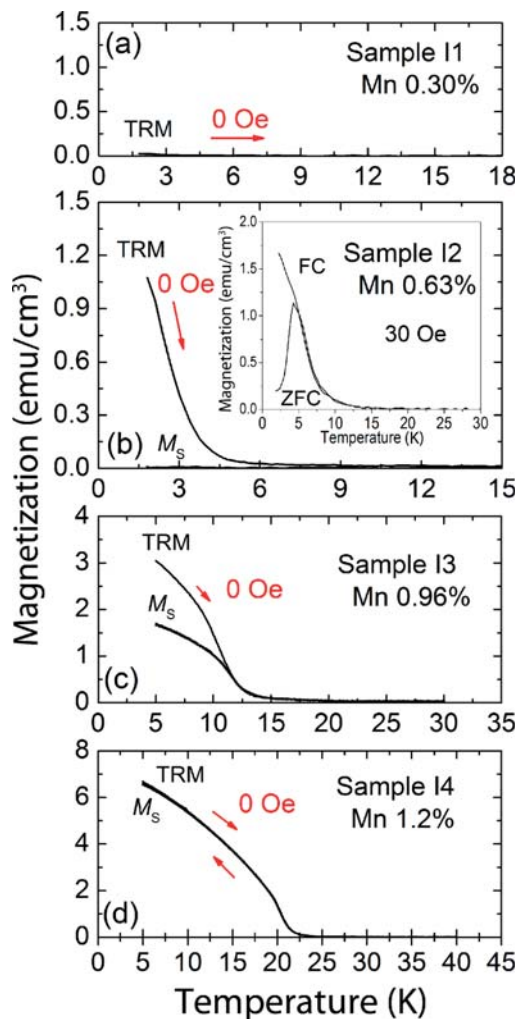


FIG. 9. The transition from the PM, via SPM, to FM phase in (In,Mn)As samples at the MIT regime. Temperature dependent thermo-remnant magnetization of (In,Mn)As samples of (a) I1, (b) I2, (c) I3, and (d) I4. The inset to (b) shows the temperature dependent magnetization under a field of 30 Oe after field cooling (FC) and zero field cooling (ZFC) for sample I2.

and long-range ferromagnetism, which is similar to the case of the (Ga,Mn)As sample with $x = 0.87\%$. Upon further increase of x to 1.2%, global ferromagnetism dominates, similarly to (Ga,Mn)As with the same x . Due to the narrow bandgap nature intrinsic InAs substrates needed for these studies are highly conductive, thus preventing magneto-transport measurements for thin (In,Mn)As layers. However, as established previously [38,39], electrical properties of ferromagnetic (In,Mn)As prepared on insulating GaAs are similar to those of (Ga,Mn)As. The negative magneto-resistance and anomalous Hall effect of (In,Mn)As are observed as in (Ga,Mn)As [38,39,42]. In Ref. [42], the authors also discussed the possible magnetic phase separation due to inhomogeneous distribution of acceptor impurities.

The Curie and SPM temperatures, T_C and T_σ , respectively, of a series of (Ga,Mn)As and (In,Mn)As samples with sequentially increasing Mn densities are shown in Fig. 10. Interestingly, an approximately linear dependence of Max

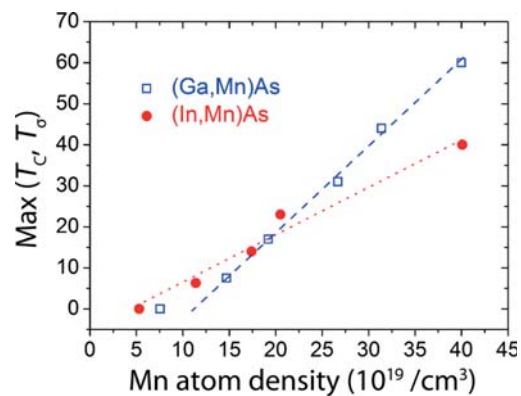


FIG. 10. Influence of the p - d coupling strength on magnetic properties of (Ga,Mn)As and (In,Mn)As. The dependence of the Curie and superparamagnetic temperature (T_C and T_σ , respectively) on the Mn atom density for (Ga,Mn)As and (In,Mn)As. The dashed and dotted lines are linear guides for eye for (Ga,Mn)As and (In,Mn)As, respectively. The crossing of two lines, and the higher and lower T_C/T_σ in (In,Mn)As at low and high x regimes, respectively, result from weaker p - d coupling in (In,Mn)As compared to (Ga,Mn)As.

$[T_C, T_\sigma]$ versus the Mn concentration is found for both materials, however, with differing slopes. In the regime of $N \leq 1.9 \times 10^{20} \text{ cm}^{-3}$, the (Ga,Mn)As samples exhibit a lower T_C or T_σ at given Mn concentrations, i.e., weaker ferromagnetism compared to (In,Mn)As, while in the regime of $N > 1.9 \times 10^{20} \text{ cm}^{-3}$, higher Curie temperatures are observed in (Ga,Mn)As. This remarkable observation substantiates experimentally the dual role of p - d exchange coupling in DFSs, as discussed theoretically previously [43]. Deeper in the metallic regime, a larger p - d interaction makes the hole-mediated ferromagnetism stronger, so that T_C in (Ga,Mn)As is higher than in (In,Mn)As, as observed previously [1,26,38,39]. However, in addition to controlling ferromagnetic coupling, a larger p - d hybridization shifts the MIT to higher hole concentrations, the effect being stronger in (Ga,Mn)As than in (In,Mn)As in which the bond length is longer. The enhanced hole localization makes ferromagnetic features weaker in (Ga,Mn)As compared to (In,Mn)As in the limit of low hole densities.

The interplay between localization and magnetism of (Ga,Mn)As with high Mn concentrations was also investigated by codoping either with donors [16] or with isovalent anions [15]. The reduction of T_C was observed together with stronger carrier localization. In our current work, we focus on (Ga,Mn)As and (In,Mn)As with very low Mn concentrations. In addition to the decreased T_C upon enhancing carrier localization [15,16], we find that the superparamagnetic phase in insulating (Ga,Mn)As and (In,Mn)As is not associated with the presence of compensating donor defects but is an intrinsic property originating, presumably, from the electronic phase separation specific to the Anderson-Mott localization.

IV. CONCLUSIONS

Through combining systematic studies of electrical and magnetic properties, we have presented experimental evidence

YE YUAN *et al.*PHYSICAL REVIEW MATERIALS **1**, 054401 (2017)

supporting the heterogeneous model of electronic states at the localization boundary in (Ga,Mn)As and (In,Mn)As without compensating donors. A transition from an insulating (hopping) to a metalliclike conductance is observed, which is accompanied by a gradual build-up of long-range magnetic coupling, as well as by an increase of the Curie temperature. The p - d Zener model prediction is consistent with the measured T_C values in metallic samples as well as with the magnitudes of T_C and T_σ on the insulator side of the transition, where the ferromagnetic coupling is mediated by weakly localized holes. Furthermore, in the limit of low Mn concentration the interplay between localization and magnetism results in more robust ferromagnetic signatures in (In,Mn)As compared to (Ga,Mn)As in which the stronger p - d coupling enhances localization.

ACKNOWLEDGMENTS

Support by the Ion Beam Center (IBC) at HZDR is gratefully acknowledged. This work is funded by the Helmholtz-Gemeinschaft Deutscher Forschungszentren (HGF-VH-NG-713). The author Y.Y. thanks financial support by Chinese Scholarship Council (File No. 201306120027). The work in Poland is supported by the Narodowe Centrum Nauki through projects MAESTRO (Grant No. 2011/02/A/ST3/00125) and by the Foundation for Polish Science through the IRA Programme financed by EU within SG OP Programme. Financial support by the EU 7th Framework Programme under the Project No. REGPOT-CT-2013-316014 (EAgLE) and the international project co-financed by Polish Ministry of Science and Higher Education, Grant Agreement No. 2819/7.PR/2013/2, is also gratefully acknowledged.

-
- [1] F. Matsukura, H. Ohno, A. Shen, and Y. Sugawara, Transport properties and origin of ferromagnetism in (Ga,Mn)As, *Phys. Rev. B* **57**, 2037(R) (1998).
- [2] T. Dietl, H. Ohno, F. Matsukura, J. Cibert, and D. Ferrand, Zener model description of ferromagnetism in zinc-blende magnetic semiconductors, *Science* **287**, 1019 (2000).
- [3] A. Kaminski and S. Das Sarma, Polaron Percolation in Diluted Magnetic Semiconductors, *Phys. Rev. Lett.* **88**, 247202 (2002).
- [4] M. Mayr, G. Alvarez, and E. Dagotto, Global versus local ferromagnetism in a model for diluted magnetic semiconductors studied with Monte Carlo techniques, *Phys. Rev. B* **65**, 241202 (2002).
- [5] B. L. Sheu, R. C. Myers, J. M. Tang, N. Samarth, D. D. Awschalom, P. Schiffer, and M. E. Flatté, Onset of Ferromagnetism in Low-Doped $\text{Ga}_{1-x}\text{Mn}_x\text{As}$, *Phys. Rev. Lett.* **99**, 227205 (2007).
- [6] T. Dietl, Interplay between carrier localization and magnetism in diluted magnetic and ferromagnetic semiconductors, *J. Phys. Soc. Jpn.* **77**, 031005 (2008).
- [7] K. Alberi, K. M. Yu, P. R. Stone, O. D. Dubon, W. Walukiewicz, T. Wojtowicz, X. Liu, and J. K. Furdyna, Formation of Mn-derived impurity band in III-Mn-V alloys by valence band anticrossing, *Phys. Rev. B* **78**, 075201 (2008).
- [8] A. Richardella, P. Roushan, S. Mack, B. Zhou, D. A. Huse, D. D. Awschalom, and A. Yazdani, Visualizing Critical Correlations Near the Metal-Insulator Transition in $\text{Ga}_{1-x}\text{Mn}_x\text{As}$, *Science* **327**, 665 (2010).
- [9] M. Sawicki, D. Chiba, A. Korbecka, Y. Nishitani, J. A. Majewski, F. Matsukura, T. Dietl, and H. Ohno, Experimental probing of the interplay between ferromagnetism and localization in (Ga,Mn)As, *Nat. Phys.* **6**, 22 (2010).
- [10] A. X. Gray, J. Minar, S. Ueda, P. R. Stone, Y. Yamashita, J. Fujii, J. Braun, L. Plucinski, C. M. Schneider, G. Panaccione, H. Ebert, O. D. Dubon, K. Kobayashi, and C. S. Fadley, Bulk electronic structure of the dilute magnetic semiconductor $\text{Ga}_{1-x}\text{Mn}_x\text{As}$ through hard X-ray angle-resolved photoemission, *Nat. Mater.* **11**, 957 (2012).
- [11] M. Kobayashi, I. Muneta, Y. Takeda, Y. Harada, A. Fujimori, J. Krempasky, T. Schmitt, S. Ohya, M. Tanaka, M. Oshima, and V. N. Strocov, Unveiling the impurity band induced ferromagnetism in the magnetic semiconductor (Ga,Mn)As, *Phys. Rev. B* **89**, 205204 (2014).
- [12] L. Chen, F. Matsukura, and H. Ohno, Electric-Field Modulation of Damping Constant in a Ferromagnetic Semiconductor (Ga,Mn)As, *Phys. Rev. Lett.* **115**, 057204 (2015)
- [13] S. Souma, L. Chen, R. Oszwaldowski, T. Sato, F. Matsukura, T. Dietl, H. Ohno, and T. Takahashi, Fermi level position, Coulomb gap, and Dresselhaus splitting in (Ga,Mn)As, *Sci. Rep.* **6**, 27266 (2016).
- [14] J. Kanski, L. Ilver, K. Karlsson, I. Ulfat, M. Leandersson, J. Sadowski, and I. Di Marco, Electronic structure of (Ga,Mn)As revisited, *New J. Phys.* **19**, 023006 (2017).
- [15] P. R. Stone, K. Alberi, S. K. Z. Tardif, J. W. Beeman, K. M. Yu, W. Walukiewicz, and O. D. Dubon, Metal-Insulator Transition by Isovalent Anion Substitution in GaMnAs: Implications to Ferromagnetism, *Phys. Rev. Lett.* **101**, 087203 (2008).
- [16] M. A. Scarpulla, P. R. Stone, I. D. Sharp, E. E. Haller, O. D. Dubon, J. W. Beeman, and K. M. Yu, Nonmagnetic compensation in ferromagnetic $\text{Ga}_{1-x}\text{Mn}_x\text{As}$ and $\text{Ga}_{1-x}\text{Mn}_x\text{P}$ synthesized by ion implantation and pulsed-laser melting, *J. Appl. Phys.* **103**, 123906 (2008).
- [17] T. Dietl and H. Ohno, Dilute ferromagnetic semiconductors: Physics and spintronic structures, *Rev. Mod. Phys.* **86**, 187 (2014), and references therein.
- [18] M. Tanaka, S. Ohya, and P. N. Hai, Recent progress in III-V based ferromagnetic semiconductors: Band structure, Fermi level, and tunneling transport, *Appl. Phys. Rev.* **1**, 011102 (2014), and references therein.
- [19] K. Edmonds, G. van der Laan, and G. Panaccione, Electronic structure of (Ga,Mn)As as seen by synchrotron radiation, *Semicond. Sci. Technol.* **30**, 043001 (2015), and references therein.
- [20] K. M. Yu, W. Walukiewicz, T. Wojtowicz, I. Kuryliszyn, X. Liu, Y. Sasaki, and J. K. Furdyna, Effect of the location of Mn sites in ferromagnetic $\text{Ga}_{1-x}\text{Mn}_x\text{As}$ on its Curie temperature, *Phys. Rev. B* **65**, 201303 (2002).
- [21] R. C. Myers, B. L. Sheu, A. W. Jackson, A. C. Gossard, P. Schiffer, N. Samarth, and D. D. Awschalom, Antisite effect on hole mediated ferromagnetism in (Ga,Mn)As, *Phys. Rev. B* **74**, 155203 (2006).

INTERPLAY BETWEEN LOCALIZATION AND MAGNETISM ...

PHYSICAL REVIEW MATERIALS 1, 054401 (2017)

- [22] E. Abrahams (ed.), *50 Years of Anderson Localization* (World Scientific, Singapore, 2010).
- [23] Y. J. Cho, M. A. Scarpulla, X. Liu, Y. Y. Zhou, O. D. Dubon, and J. K. Furdyna, Magnetic cluster phases of Mn-interstitial-free (Ga,Mn)As, *AIP Conf. Proc.* **893**, 1221 (2007).
- [24] Y. Yuan, R. Hübner, F. Liu, M. Sawicki, O. Gordan, G. Salvan, D. R. T. Zahn, D. Banerjee, C. Baetz, M. Helm, and S. Zhou, Ferromagnetic Mn-implanted GaP: Microstructures versus magnetic properties, *ACS Appl. Mater. Interfaces* **8**, 3912 (2016).
- [25] M. Sawicki, W. Stefanowicz, and A. Ney, Sensitive SQUID magnetometry for studying nanomagnetism, *Semicond. Sci. Technol.* **26**, 064006 (2011).
- [26] M. Wang, K. Olejnik, J. Wunderlich, M. Cukr, K. Vyborny, A. W. Rushforth, K. W. Edmonds, R. P. Campion, B. L. Gallagher, J. Sinova, and T. Jungwirth, Achieving high Curie temperature in (Ga,Mn)As, *Appl. Phys. Lett.* **93**, 132103 (2008).
- [27] P. Němec, V. Novak, N. Tesarova, E. Rozkotova, H. Reichlova, D. Butkovicova, F. Trojanek, K. Olejnik, P. Maly, R. P. Campion, B. L. Gallagher, J. Sinova, and T. Jungwirth, The essential role of carefully optimized synthesis for elucidating intrinsic material properties of (Ga,Mn)As, *Nat. Commun.* **4**, 1422 (2013).
- [28] P. Wadley, A. A. Freeman, K. W. Edmonds, G. van der laan, J. S. Chauhan, R. P. Campion, A. W. Rushforth, B. L. Gallagher, C. T. Foxon, F. Wilhelm, A. G. Smekhova, and A. Rogalev, Element-resolved orbital polarization in (III,Mn)As ferromagnetic semiconductors from K-edge X-ray magnetic circular dichroism, *Phys. Rev. B* **81**, 235208 (2010).
- [29] C. Sliwa and T. Dietl, Orbital magnetization in dilute ferromagnetic semiconductors, *Phys. Rev. B* **90**, 045202 (2014).
- [30] M. Linnarsson, E. Janzen, B. Monemar, M. Kleverman, and A. Thilderkvist, Electronic structure of the GaAs:Mn-Ga center, *Phys. Rev. B* **55**, 6938 (1997).
- [31] A. L. Efros and B. I. Shklovskii, Coulomb gap and low temperature conductivity of disordered systems, *J. Phys. C: Solid State Phys.* **8**, L49 (1975).
- [32] L. Li, S. Yao, S. Zhou, D. Bürger, O. Roshchupkina, S. Akhmadaliev, A. Rushforth, R. Campion, J. Fassbender, and M. Helm, Tailoring the magnetism of GaMnAs films by ion irradiation, *J. Phys. D: Appl. Phys.* **44**, 045001 (2011).
- [33] M. A. Scarpulla, R. Farshchi, P. R. Stone, R. V. Chopdekar, K. M. Yu, Y. Suzuki, and O. D. Dubon, Electrical transport and ferromagnetism in GaMnAs synthesized by ion implantation and pulsed-laser melting, *J. Appl. Phys.* **103**, 073913 (2008).
- [34] D. Neumaier, M. Turek, U. Wurstbauer, A. Vogl, M. Utz, W. Wegscheider, and D. Weiss, All-Electrical Measurement of the Density of States in (Ga,Mn)As, *Phys. Rev. Lett.* **103**, 087203 (2009).
- [35] F. Matsukura, Magnetotransport properties of metallic (Ga,Mn)As films with compressive and tensile strain, *Physica E* **21**, 1032 (2004).
- [36] J. Schneider, U. Kaufmann, W. Wilkening, M. Baeumler, and F. Kohl, Electronic Structure of the Neutral Manganese Acceptor in Gallium Arsenide, *Phys. Rev. Lett.* **59**, 240 (1987).
- [37] T. Dietl, H. Ohno, and F. Matsukura, Hole-mediated ferromagnetism in tetrahedrally coordinated semiconductors, *Phys. Rev. B* **63**, 195205 (2001).
- [38] H. Ohno, H. Munekata, T. Penney, S. Von Molnár, and L. L. Chang, Magnetotransport Properties of *p*-type (In,Mn)As Diluted Magnetic III-V Semiconductors, *Phys. Rev. Lett.* **68**, 2664 (1992).
- [39] T. Schallenberg and H. Munekata, Preparation of ferromagnetic (In,Mn)As with a high Curie temperature of 90 K, *Appl. Phys. Lett.* **89**, 042507 (2006).
- [40] S. Zhou, Y. Wang, Z. Jiang, E. Weschke, and M. Helm, Ferromagnetic InMnAs on InAs prepared by ion implantation and pulsed laser annealing, *Appl. Phys. Express* **5**, 093007 (2012).
- [41] Y. Yuan, Y. Wang, K. Gao, M. Khalid, C. Wu, W. Zhang, F. Munnik, E. Weschke, C. Baetz, W. Skorupa, M. Helm, and S. Zhou, High Curie temperature and perpendicular magnetic anisotropy in homoepitaxial InMnAs films, *J. Phys. D: Appl. Phys.* **48**, 235002 (2015). In this previous work, the pulsed laser melting fluence was 0.3 J/cm² and the Mn concentration *x* was determined by proton-induced X-ray emission (PIXE), both being different from those used for the samples shown in the current manuscript.
- [42] V. V. Rylkov, B. A. Aronzon, A. S. Lagutin, V. V. Podol'skii, V. P. Lesnikov, M. Goiran, J. Galibert, B. Raquet, and J. Léotin, Transport features in laser-plasma-deposited InMnAs layers in strong magnetic fields, *J. Exp. Theor. Phys.* **108**, 149 (2009).
- [43] T. Dietl, Hole states in wide band-gap diluted magnetic semiconductors and oxides, *Phys. Rev. B* **77**, 085208 (2008).

2D Materials

OPEN ACCESS



RECEIVED

9 December 2016

REVISED

14 March 2017

ACCEPTED FOR PUBLICATION

29 March 2017

PUBLISHED

28 April 2017

Original content from this work may be used under the terms of the [Creative Commons Attribution 3.0 licence](https://creativecommons.org/licenses/by/3.0/).

Any further distribution of this work must maintain attribution to the author(s) and the title of the work, journal citation and DOI.



PAPER

Two-dimensional MoS₂ under ion irradiation: from controlled defect production to electronic structure engineering

Mahdi Ghorbani-Asl¹, Silvan Kretschmer¹, Douglas E Spearot² and Arkady V Krasheninnikov^{1,3}

¹ Institute of Ion Beam Physics and Materials Research, Helmholtz-Zentrum Dresden-Rossendorf, 01314 Dresden, Germany

² Department of Mechanical & Aerospace Engineering, University of Florida, Gainesville, FL 32611, United States of America

³ Department of Applied Physics, Aalto University School of Science, PO Box 11100, 00076 Aalto, Finland

E-mail: mahdi.ghorbani@hzdr.de and a.krasheninnikov@hzdr.de

Keywords: transition metal dichalcogenides, defects, irradiation, first-principles calculations

Supplementary material for this article is available [online](#)

Abstract

Two-dimensional (2D) transition metal dichalcogenides (TMDs), like MoS₂, have unique electronic and optical properties, which can further be tuned using ion bombardment and post-synthesis ion-beam mediated methods combined with exposure of the irradiated sample to precursor gases. The optimization of these techniques requires a complete understanding of the response of 2D TMDs to ion irradiation, which is affected by the reduced dimensionality of the system. By combining analytical potential molecular dynamics with first-principles calculations, we study the production of defects in free-standing MoS₂ sheets under noble gas ion irradiation for a wide range of ion energies when nuclear stopping dominates, and assess the probabilities for different defects to appear. We show that depending on the incident angle, ion type and energy, sulfur atoms can be sputtered away predominantly from the top or bottom layers, creating unique opportunities for engineering mixed MoSX compounds where X are chemical elements from group V or VII. We study the electronic structure of such systems, demonstrate that they can be metals, and finally discuss how metal/semiconductor/metal junctions, which exhibit negative differential resistance, can be designed using focused ion beams combined with the exposure of the system to fluorine.

1. Introduction

Beams of energetic ions and electrons are powerful tools to change the morphology and properties of both bulk [1, 2] and nano [3–5] materials. This is particularly relevant to two-dimensional (2D) systems, as their ‘thickness’ is smaller than the ranges of even low-energy particles, so that the whole structure can easily be treated, as opposed to macroscopically large objects where much higher energies of electrons and especially ions are required, and the effects of irradiation on sample morphology are spatially nonuniform.

The very nature of 2D materials, which consist of only surface, also opens new routes for ion and electron beam engineering of their structure and properties through controllable introduction of defects [6]. In addition to ‘direct’ methods of nanomaterial processing such as cutting the target by atom sputtering [7–13], changing its stoichiometry [14, 15], welding system parts [16, 17] by creating reactive defects at their surfaces, or impurity atom implantation [18–20],

beam-mediated techniques can be used when irradiation is combined with exposure to precursor gases, similar to bulk systems [21]. For instance, atoms can be sputtered away from a 2D material, followed by an exposure to chemical species which fill the vacancies, so that impurities can be introduced into the system with a high spatial resolution if focused beams are used. The precursor gas can also be added during the irradiation, and the beam will break gas molecules thus providing reactive species. Examples of post-synthesis beam-mediated treatments of 2D materials include doping of hexagonal boron nitride with carbon [22], or graphene with metal atoms [23].

Experiments [24–26] and simulations [27, 28] indicate that the response of 2D targets to irradiation is different in many ways from that of bulk materials. Deposition of the energy by the energetic particle and its redistribution can also be different in systems with reduced dimensionalities [4], which may affect defect production, and thus justifies investigations of irradiation-induced phenomena in 2D targets.

So far, most of the ion irradiation studies on 2D materials have been done for graphene, a monoatomic solid, and much less is known about the response of other 2D systems to ion beams. Specifically, the behavior of 2D transition metal dichalcogenides (TMDs), which are composed of atoms of several types, under ion irradiation has not been studied systematically. At the same time, these materials are of particular interest, since they have already shown appealing potential for nanoelectronics, photonics, catalysis, and energy applications due to a unique combination of electronic, optical, and mechanical properties [29–32]. New functionalities can also be added to 2D TMDs by using irradiation directly or by attaching molecules and atoms to vacancies. Indeed, first experiments [33] showed that the transport characteristics of a MoS₂-monolayer (ML) field effect transistor can be modulated via irradiation with swift heavy ions. A similar technique has been used for defect engineering in single- and few-layer of MoS₂ [34]. The experimental results on the bombardment of MoSe₂ and WSe₂ MLs using a helium ion microscope indicated that the ion beam changes the electronic structure, shifts optical response towards the visible region and even increases the elastic Young's modulus [35, 36]. The presence of magnetic ordering in proton-irradiated bulk MoS₂ samples was recently reported [37] indicating that spin-polarized transport and magnetism can be realized in 2D TMDs. Furthermore, the possibility of selective desulfurization of MoS₂-ML through a low-energy argon ion irradiation [38] and the post-growth tuning of band gap in MoS₂-ML by substitution of top-layer sulfur atoms with selenium atoms [39] has been demonstrated. It has also been shown that the stoichiometry of few-layer MoS₂ flakes can be changed by He ion irradiation, and ribbons about 9 nm wide can be produced [40].

To fully leverage the opportunity of irradiation treatment of 2D TMDs, it is imperative to understand the response of these materials to impacts of energetic particles and find optimum parameters, such as particle energies, angles, ion mass, etc for efficient atomic structure engineering using ion bombardment. To this end, atomistic computer simulations are an indispensable tool for getting microscopic insights into defect production mechanisms in solids under irradiation [41]. At the same time, while the behavior of MoS₂, the most wide-spread member of the TMD family, under electron beam has been addressed [42], there is no theoretical data on the production of defects in these systems under ion irradiation.

Here, we assess the effects of ion irradiation on suspended MoS₂-ML by using analytical potential molecular dynamics (MD) simulations combined with density-functional theory (DFT) methods. We characterize the types and assess the abundance of point defects which appear in MoS₂ under irradiation with various noble-gas ions in a wide range of ion energies. We demonstrate that the ratio of the atoms sputtered from upper and bottom sulfur layers can be tuned by

choosing the appropriate energy and incident angle of the ion beam. Finally, we show the possibility for engineering mixed MoSX compounds where X are chemical elements from group V or VII, and discuss the properties of such systems and lateral MoSX-MoS₂ heterostructures.

2. Methods

2.1. Molecular dynamic simulations of ion irradiation

The LAMMPS package [43] is used to perform all classical simulations. A 2D periodic boundary condition is applied parallel to the basal plane of MoS₂. All structures are fully optimized using a nonlinear conjugate gradient energy minimization method available in LAMMPS. The interaction between ions (noble gas) and MoS₂-ML was constructed by the Ziegler–Biersack–Littmark (ZBL) universal repulsive potential [44] for modeling energetic collisions, which can accurately describe the interaction between atoms at small separations ($<1 \text{ \AA}$). We have used an adaptive time step for impact simulations as implemented in LAMMPS. Using this method, the time step is defined depending on the velocity of fastest moving atoms in the system, varying from almost one attosecond to one femtosecond. The ion irradiation simulations were carried out using a MoS₂ supercell containing 1254 atoms. This supercell corresponds to the 11×19 unit cells of the ideal lattice with dimensions of about $60 \times 60 \text{ \AA}^2$ in a rectangular representation (figure 1(a)). As strain is known to affect the response of nanomaterials to irradiation [45, 46], the supercell size was carefully optimized. The impact points for ion irradiation were randomly/uniformly selected within the minimum irreducible area of the lattice (figures 1(b) and S1). Our benchmark calculations for both uniform and random impact distribution showed that a minimum of 150 impact points can give very similar statistics from MD simulations (see figure S1). In order to adequately model the distribution of the energy brought in by the ion into the system and the evolution of the atomic structure after the impact, the system was quenched to zero temperature during a time period of 10 ps using a Nosé–Hoover thermostat. We performed 4896 independent simulations for each ion and angle that resulted in a total number of $\sim 150\,000$ simulations.

2.2. Electronic structure and transport calculations

Density-functional theory (DFT) calculations with the PBE [47] exchange-correlation functional have been carried out using the Atomistix ToolKit (ATK) code [48]. An SCF convergence tolerance of 0.0001 Hartree and a kinetic energy cutoff of 150 Hartree have been used for the calculations. A vacuum space of 30 \AA was set normal to the layer for avoiding any artificial interaction between the layer and its periodic images. The Brillouin zone (BZ) of the unit cell system and the transport model were sampled

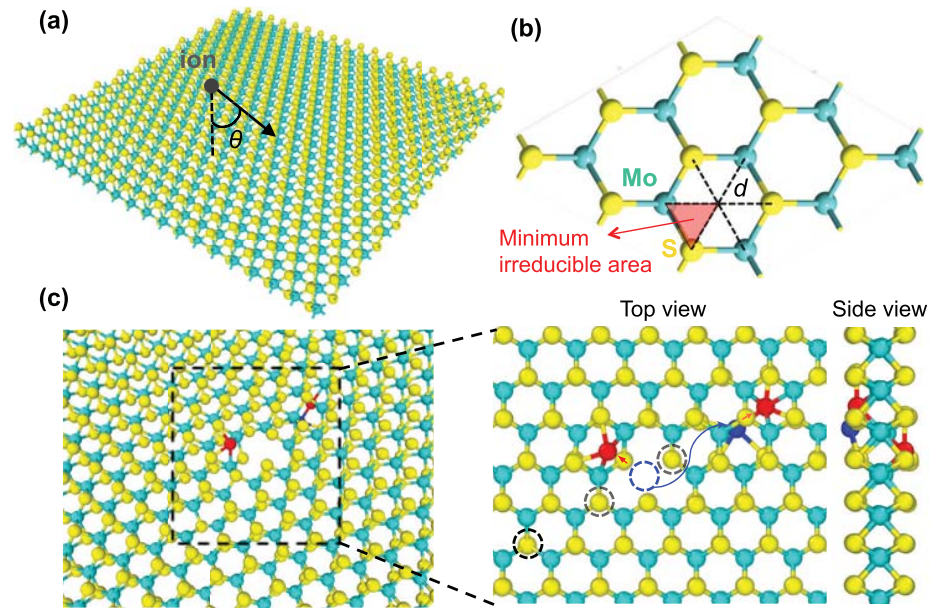


Figure 1. (a) Schematic illustration of the setup for ion irradiation simulations of MoS₂-ML. Molybdenum and sulfur atoms are shown in blue and yellow, respectively. (b) Definition of the minimum irreducible area (the red triangle) used for ion impacts. (c) A typical atomic structure of the target after an impact of an Ar ion with an energy of 254 eV and normal incidence ($\theta = 0$). Black dashed circles represent single S vacancies, the blue dashed circle shows a Mo vacancy and red atoms display S atoms with trigonal symmetry configuration, as in the T phase.

using $7 \times 7 \times 1$ and $1 \times 5 \times 100$ k points, respectively. The electron transport calculations were performed using the DFT method in conjunction with the non-equilibrium Green's function (NEGF) [49] approach as implemented in ATK. Poisson equation was solved using a fast Fourier transform solver in a self-consistent manner. The NEGF method has already been applied to study electron transport in various TMDs [50, 51].

3. Results and discussion

In order to get microscopic insights into defect production under ion impacts in free-standing MoS₂-ML, we carried out MD simulations as described in the Methods section. We considered the limit of low energies of ions when nuclear stopping dominates over electronic stopping. The simulation setup is shown in figure 1, which also presents the minimum irreducible area (the red triangle) used in ion impact simulations. We addressed low-dose irradiation, so that it was assumed that there is no cumulative effect originating from impacts of several ions into the same area.

We first assessed the ability of the interatomic potentials available for MoS₂-ML to describe atomic structure and energetics of point defects. We systematically calculated formation energies for different point defects using four available potentials [52–56] for MoS₂-ML and compared those to the energies obtained using DFT calculations [57]. These results are shown in figure 2. We analyzed 8 types of point defects, with most of them being observed in transmission electron microscopy (TEM) experiments [6, 42, 58, 59].

The formation energies of defects were calculated as: $E_f = E_{\text{def}} - E_{\text{bulk}} + \mu_X$, where E_{bulk} and E_{def} are the energies of the pristine system and defect containing supercell. μ_X represents the chemical potential of the X species, which is taken as the energy of the isolated atom (group). Such a choice of the chemical potentials is the most adequate for the physical problem we consider. By default $\mu_X = 0$ in analytical potential calculations for all isolated atoms, and the DFT values are also close to zero, $\mu_X < 0.1$ eV.

Among the considered potentials, the many-body reactive empirical bond-order (REBO) [52] and Stillinger–Weber (SW) 2013 potential [54] provide the best agreement in comparison to the DFT results [57]. The formation energy of single S vacancies as obtained from REBO in our calculations also agrees with the previously reported values [60], while the SW 2013 potential underestimates it by some 20% giving rise to a shift in ion threshold energies for defect production, as discussed below. As another important test, we also calculated the difference in energy between the 1T and 2H phases of MoS₂. The SW 2013 potential gives a better description of the phases, while REBO underestimates the energy difference (table S1). Another feature of the SW potential is that it is computationally efficient, being faster than REBO by a factor of 12. Based on the above, we conducted most of the calculations using the SW 2013 potential and verified some of the results using REBO. Using molecular dynamic simulations, we also calculated the displacement threshold energies (T_d) for Mo and S, i.e. the minimum kinetic energy required to transfer to S/Mo atom in order leave

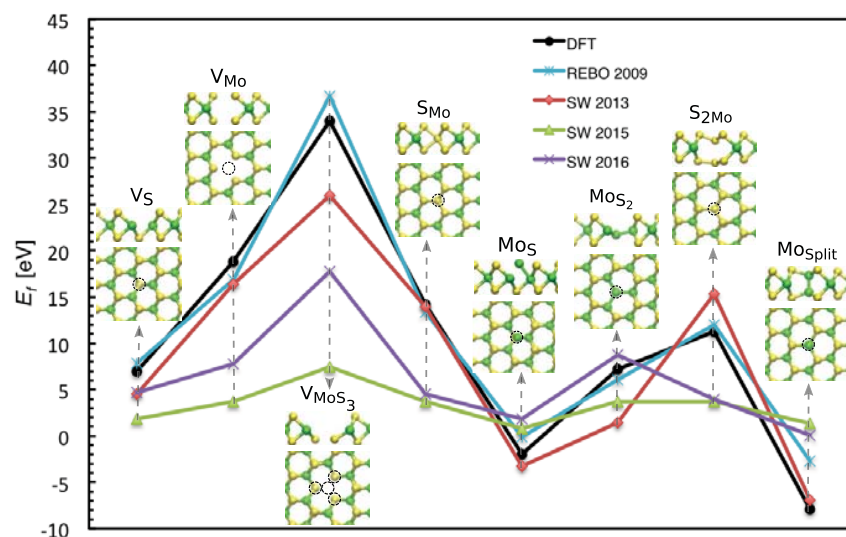


Figure 2. Comparison between formation energies of various type of defects calculated using DFT and empirical potentials. Different types of defects in MoS₂-ML, from left: vacancies (I)–(III), antisites (IV)–(VII), and the Mo–Mo split interstitial (VIII). Black dashed circles show the position of the defect.

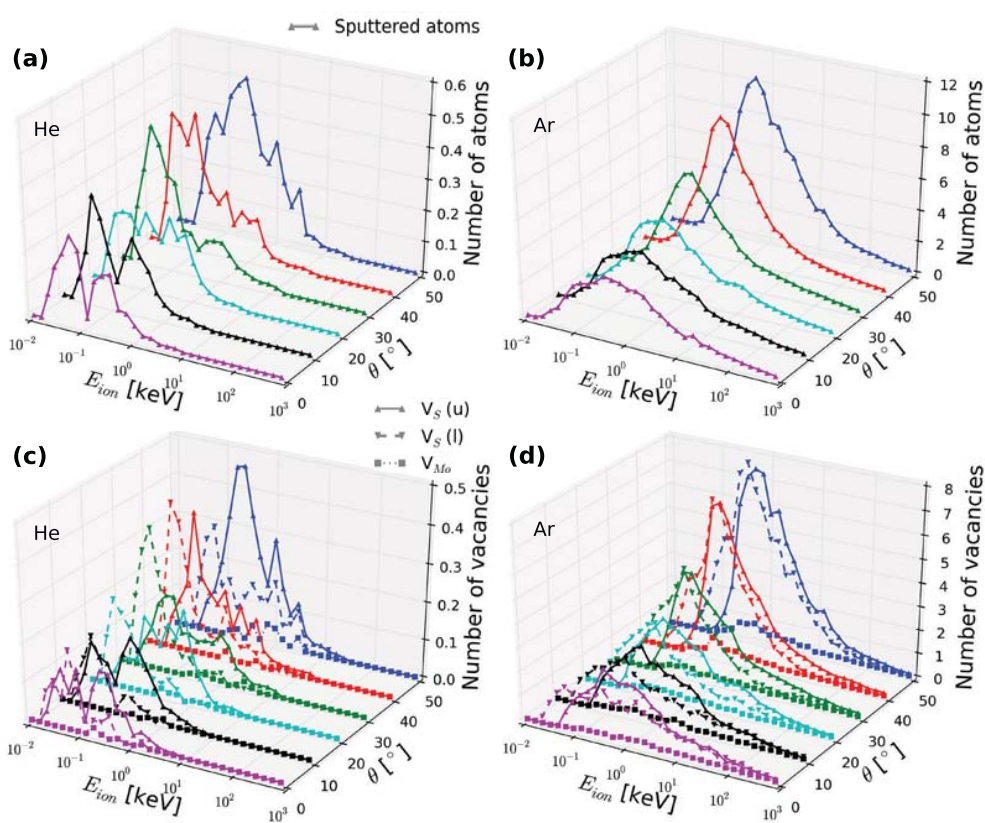


Figure 3. Upper panels: average numbers of sputtered atoms in MoS₂-ML as functions of ion energy and incident angle for He (a) and Ar (b) ions. Lower panels: the corresponding numbers of S vacancies produced in the upper layer ($V_S(u)$), the lower layer ($V_S(l)$) and Mo vacancies (V_{Mo}) for He (c) and Ar (d).

its position in the system in a binary collision. The displacement thresholds for the SW potential were found to be $T_d^S = 5.0$ eV and $T_d^{Mo} = 31.7$ eV for sulfur and molybdenum, respectively. The results are in line with the energies previously obtained using DFT [42], as shown in table S2.

Figure 3 presents the average number of sputtered target atoms as a function of ion energy ranging from 10 eV to 1000 keV. Mostly S vacancies are produced, including single and double vacancies with two missing S atoms on top of each other. This is consistent with the results of early experimental studies of MoS₂ surfaces

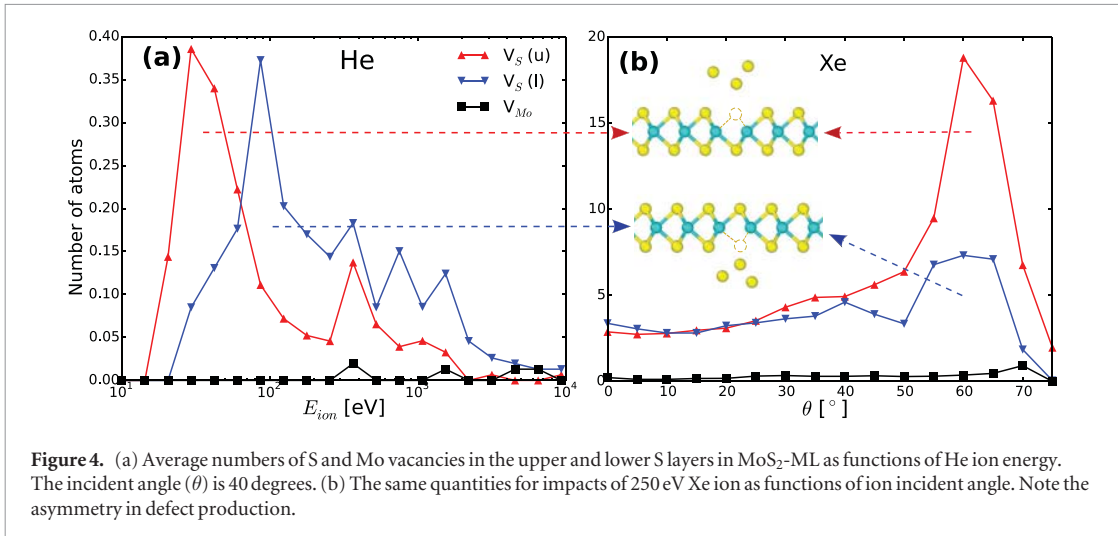


Figure 4. (a) Average numbers of S and Mo vacancies in the upper and lower S layers in MoS₂-ML as functions of He ion energy. The incident angle (θ) is 40 degrees. (b) The same quantities for impacts of 250 eV Xe ion as functions of ion incident angle. Note the asymmetry in defect production.

subjected to ion irradiation [61, 62]. S adatoms and S atoms displaced from the H to the distorted T positions shown in red in figure 1(c) were also rather common, but our MD simulations indicated that these defects should not be stable on macroscopic time scales even at room temperature.

Sputtering yield initially grows with ion energy up to a maximum value and then decreases, contrary to bulk targets where the total amount of damage is proportional to particle energy. The drop in the number of defects (average number of defects per ion impact) produced in 2D systems at high energies is due to the absence of collisional cascades in atomically thin targets, as shown for graphene [27] and h-BN [63], and a smaller cross section for energy transfer from the ion to the recoil atom at high ion energies [4]. The number of defects created in MoS₂-ML due to ion impacts also follows this trend. The data for other ions (Ne, Kr, and Xe) is shown in figure S2. It can be seen that the minimum ion energy for defect production (E_{min}) depends on ion mass. This should be immediately clear from the kinematic factor describing a head-on binary collision $E_{min} = T_d(m_i + m_t)^2/4m_i m_t$, where T_d is the S atom displacement energy, and m_i (m_t) represent ion (target atom) masses.

The results presented in figures 3 and S2 indicate that the incident angle (θ) has a significant effect on defect production. In general, the number of sputtered atoms increases with θ . The peak in the sputtering yield versus ion energy curve shifts towards higher energies with tilting the ion beam direction from normal, as larger incident angles increase the projected atomic density of the target in the ion direction.

In order to better characterize defect production in MoS₂-ML under ion irradiation, single vacancies produced by ion impacts were divided into 3 main categories: S vacancy in the upper layer, Mo vacancy and S vacancy in the lower layer. As evident from figures 3 and S2, the probability for S vacancies to appear is significantly higher than that for Mo vacancies due to much higher threshold displacement for Mo than S. As for S

vacancies, the ratio of the defect numbers in the upper and bottom layers depends on ion energy and atom types. At low energies of the ions, vacancies are mostly created in the upper layer, as more energy is required for the ion to pass through the system and collide with a S atom in the bottom layer. The same is true for the energy transfer mechanism involving several atoms. The ratio also depends on the incident angle as shown in figure 4. At large angles and low ion energies, vacancies are produced mostly in the upper layers, then the trend changes. The effect is more evident for lighter ions. Two examples of sputtering from upper and lower S layers under the ion irradiation are shown in Movies M1 and M2 (supplementary information (stacks.iop.org/TDM/4/025078/mmedia)).

An interesting feature of the relationship between sputtered atoms and ion energy is the presence of two maxima clearly visible for light ions. Such features have not been observed for 2D materials composed of atoms of the same type (graphene) [27] or atoms of roughly the same mass (h-BN) [63]. The analysis of the atom trajectories indicates that several mechanisms contribute to production of defects in this two-component solid with Mo atoms being much heavier than S: (1) direct collisions of He ions with S atoms, collisions with Mo, followed by energy transfer from the recoil Mo atom to S atoms under Mo, and (2) collisions of the backscattered He ions with the S atoms in the upper layer.

In order to fully understand the response of MoS₂-ML to ion bombardment, we calculated the cross-sections for defect production of single Mo and S vacancies in MoS₂-ML as functions of incident ion energy for various ions (see figures 5 and S3). In the binary collision calculations, shown in figure 5(a), the cross section (σ) can be obtained via calculation of the maximum impact parameter (ρ) for which the ion transfers enough energy to displace the recoil atom (displacement threshold). Accordingly, the cross section is simply evaluated as $\sigma = \pi\rho^2$. Figure 5(b) presents cross sections for various ions. Figure 5(c) shows the number of sputtered atoms

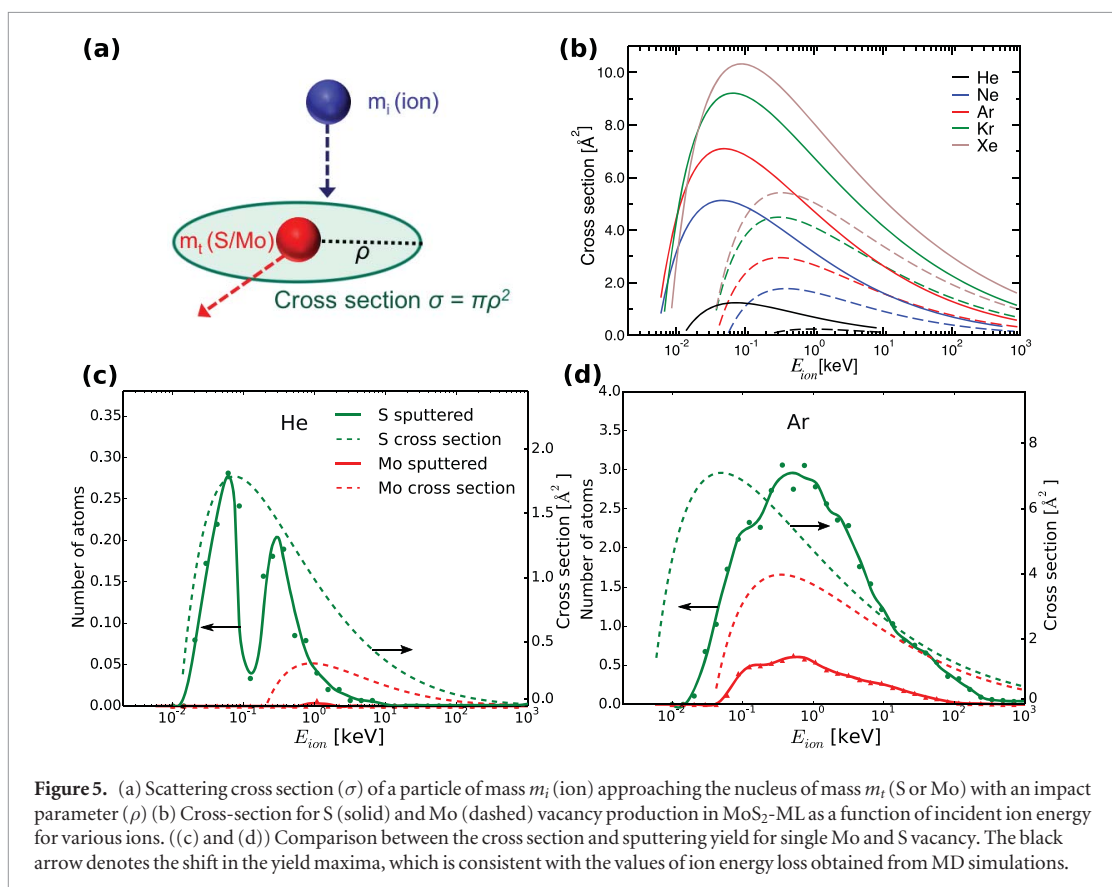


Figure 5. (a) Scattering cross section (σ) of a particle of mass m_i (ion) approaching the nucleus of mass m_t (S or Mo) with an impact parameter (ρ) (b) Cross-section for S (solid) and Mo (dashed) vacancy production in MoS₂-ML as a function of incident ion energy for various ions. ((c) and (d)) Comparison between the cross section and sputtering yield for single Mo and S vacancy. The black arrow denotes the shift in the yield maxima, which is consistent with the values of ion energy loss obtained from MD simulations.

for normal incidence of He ions along with the cross sections for S and Mo atoms. The peak positions and cross section onsets correlate with each other, especially if we account for the additional energy loss of the impinging ions, which was evaluated as the energy difference between the initial energy of ion and the energy after the first collision with target atoms. By comparison between figures 4(a) and 5(c), one can clearly see that the first peak is mostly governed by sputtering of atoms from the upper S layer while the second peak is caused by sputtering of the lower S layer.

The shapes of the curves for other ions considered can also be understood through a combination of the system geometry (tri-layer structure) and the above mechanisms, as illustrated for Ar in figure 5(d), but the shift in the onset of defect production is more pronounced due to a larger fraction of the kinetic energy of the ion being transferred to other target atoms. Our results are also consistent with the experimental results showing that He ion irradiation of bulk MoS₂ creates similar but smaller nanostructures in comparison to Ar ions with the same energy [64].

MD simulations using the REBO potential for all ions with normal incidence gave similar results, as shown in figure 6. The sputtering yield agrees very well with the results obtained using the SW potential implying the reliability of our approach. The displacement thresholds for S and correspondingly the onset energies (when defects appear) are slightly higher in the calculations using the REBO potential than the values obtained from SW potential. This correlates with

higher formation energies for S vacancies in REBO as compared to SW (see figure 2).

Different numbers of S vacancies produced in the upper and bottom layers of MoS₂-ML by energetic ions under specific conditions not only confirm that the preferential sputtering from one side of the MoS₂ sheet can be achieved, as already experimentally demonstrated [38, 39], but also indicate that MoS₂-ML can be selectively patterned with a high spatial resolution if focused ion beams can be used, e.g. in the He ion microscope [65]. If additional species are added during irradiation or after without exposing the sample to air, the missing S atoms can be substituted with other chemical elements, as schematically illustrated in figure 7(a). One can expect that in addition to S homologs Se and Te, other chemical elements can be used, and materials with different electronic properties can be manufactured.

To explore this scenario, we studied energetics and electronic properties of single layers of a mixed system, when S atoms on one side of the MoS₂ sheet are substituted with atoms from group V or VII. Both H and T phases were studied and the range of species is shown in figure 7. To access the stability of such compounds, we calculated cohesive energies (energy needed to dissociate the material into its individual constituent) by $E_{\text{coh}} = E_{\text{tot}} - \sum N_x E_x$, where N_x is the number of individual constituents, E_{tot} and E_x are the total energy of the system and energy of its component parts, respectively. The energies proved to be negative and for several compounds comparable to that of MoS₂-ML,

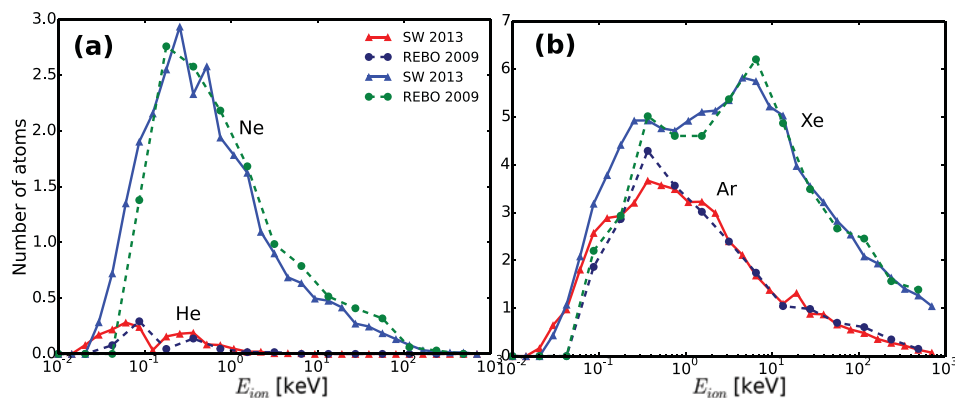


Figure 6. (a) Comparison between average numbers of S and Mo atoms sputtered from MoS₂-ML under normal incidence Ne irradiation. (b) The number of sputtered S atoms under Ar and Xe ions as calculated using the SW (solid line) and REBO (dashed line) potentials.

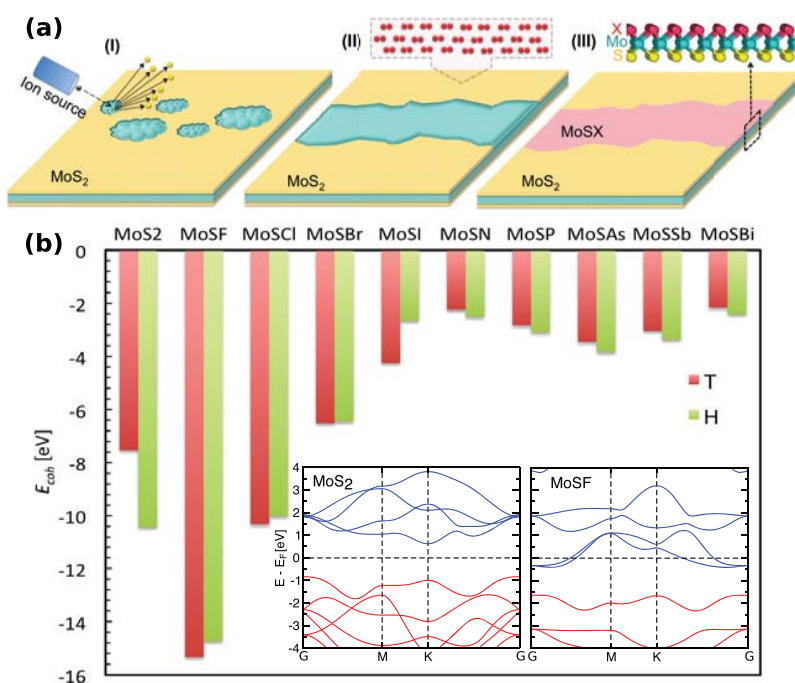


Figure 7. (a) Schematic illustration of ion-beam mediated production of mixed MoSX material starting from MoS₂-ML. The ion irradiation is used to sputter S atoms from one side of MoS₂-ML, followed by an exposure to a X gas precursor. (b) Cohesive energy per primitive cell for the MoSX alloys where X stands for chemical elements from group V and VII. Inset: electronic band structures of MoS₂ and MoSF alloy. The Fermi level is shifted to zero.

indicating that the mixture compounds should be at least metastable, figure 7(b).

We also calculated the energy difference between the mixed and segregated compounds, which are provided in table S4. It proved to be of the same order of magnitude (about or less than 0.1 eV per formula unit) as for the MoSSe system, that was experimentally realized, which may serve as another piece of evidence that the mixed material should be stable and will not spontaneously segregate into two compounds. Therefore, such 2D alloys can be manufactured via a post-synthesis procedure including vacancy production and atomic substitution under ion beam. Among considered compounds, MoSF was found to be energetically

most favorable in accord with the recent experimental data showing the high stability of doped MoS₂ samples with F-containing groups [66]. We stress that the mixed materials may be metastable with respect to dissociation into pure components, but they still could be manufactured, as ion-beam mediated engineering does not assume that the material is always in the thermodynamic equilibrium.

To get further insights into the electronic properties of the mixed compounds, we have analyzed the electronic structure of MoSF, presented in figures 7 and S4. Our band structure calculations showed that MoSF is a metal, see the inset in figure 7(b). Since F has an extra electron as compared to S and can be

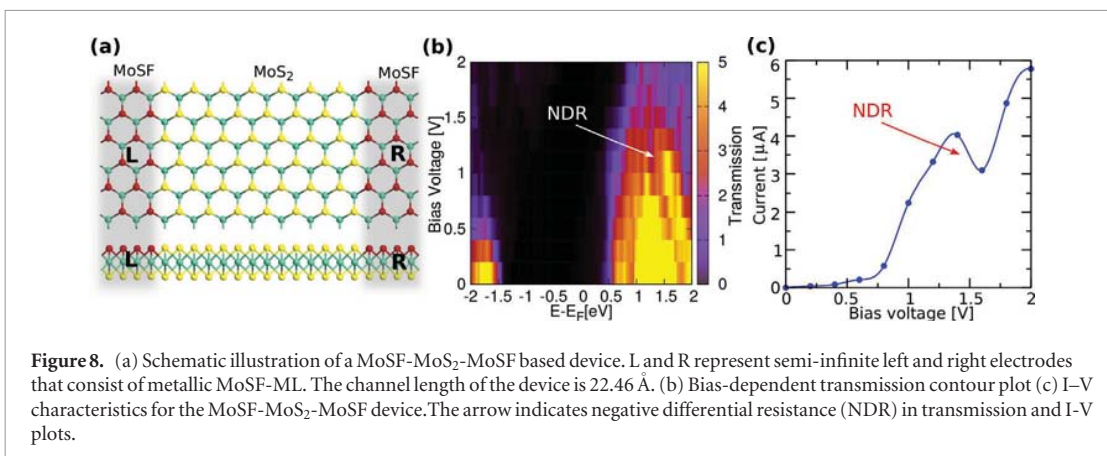


Figure 8. (a) Schematic illustration of a MoSF-MoS₂-MoSF based device. L and R represent semi-infinite left and right electrodes that consist of metallic MoSF-ML. The channel length of the device is 22.46 Å. (b) Bias-dependent transmission contour plot (c) I-V characteristics for the MoSF-MoS₂-MoSF device. The arrow indicates negative differential resistance (NDR) in transmission and I-V plots.

referred to as n-type dopant, the metallic behavior can be understood by a shift of the Fermi level to the conduction band. This suggests that partial substitution of S with F can be used to inject electrons into the system, and the metallic MoSF compound can serve as the electrode material attached to the semiconducting MoS₂-ML. Thus the entire device can be implemented on a single sheet, avoiding the severe problems of making good electrical contacts in 2D materials. Mixed MoS₂ and MoS₂Br compounds also proved to be metals, at least at the DFT/PBE level of theory, as shown in figure S5. To study the electronic properties of such a lateral heterostructure, we carried out electronic transport calculations through the system where the metallic MoSF compound serves as an electrode material attached to the semiconducting MoS₂-ML, shown in figure 8(a). The results showed a non-linear current-voltage similar to characteristics of a resonant tunneling diode. The threshold voltage of ~ 0.5 V reflects the energy mismatch between the Fermi level of the metallic electrodes and the lowest unoccupied levels of the channel region. In addition, the I-V plot indicates a negative differential resistance (NDR) feature at $1.37 \text{ V} < V_{\text{bias}} < 1.70 \text{ V}$ with a peak-to-valley ratio of ~ 1.3 comparable to those reported for graphene-h-BN-graphene-based tunneling devices [67]. The NDR effect can be attributed to the drop in the transmission coefficient within the corresponding bias window (see figures 8(b) and (c)). This feature can be used in a number of electronic devices such as frequency multipliers and high-frequency oscillators.

4. Conclusion

In summary, using molecular dynamics simulations, we studied the production of defects in MoS₂-ML under noble gas ion irradiation. For a wide range of ion energies, in the regime where nuclear stopping dominates, and various incident angles we showed that the most prolific defects which appear under ion bombardment are S vacancies. We demonstrated that the dependence of the total number of sputtered atoms on ion energy is qualitatively the same as in other 2D materials, but it has unique features related to the tri-

layer geometry of MoS₂-ML and the presence of two types of atoms with drastically different masses. We anticipate similar effects to occur in ion irradiation of other layered TMDs due to analogy in the structural properties. As vacancies in TMDs have been demonstrated to be an effective tool to tailor the carrier types and optical response in these systems [68, 69], ion bombardment is the ideal tool to achieve that with high spatial resolution. We showed that depending on the angle of incidence, ion type and energy, S atoms can be sputtered away predominantly from the top or bottom layers, creating unique opportunities for engineering mixed MoSX compounds where X are chemical elements from group V or VII. Using first-principles calculations, we studied the electronic structure of such systems, and demonstrated that they can be metals. We discussed how lateral heterostructures representing metal/semiconductor/metal junctions can be designed using focused ion beams combined with the exposure of the system to a precursor gas, e.g. fluorine. We showed that MoSF-MoS₂-MoSF has electronic transport properties reminiscent of those of resonant tunneling diodes, exhibiting negative differential resistance. Our results indicate that ion bombardment is a promising tool to tune stoichiometry and other properties of TMD monolayers and implement a broad range of nanoscale electronic devices via the appropriate post-growth processing of TMDs based on ion irradiation combined with the exposure of the samples to precursor gases.

Acknowledgments

We thank H-P Komsa and J Kotakoski for discussions. AVK acknowledges the Academy of Finland for the support under Project No. 286279, and the support from the US Army RDECOM via contract No. W911NF-15-1-0606. We further acknowledge the help from Dr Jin-Wu Jiang (Shanghai University) and Julian Schneider (QuantumWise) for using SW potentials of MoS₂-ML. The irradiation movies are created using the Open Visualization Tool (OVITO) [70]. The computational support from the HZDR computing cluster is gratefully appreciated.

References

- [1] Nastasi M, Mayer J and Hirvonen J 1996 *Ion-Solid Interactions—Fundamentals and Applications* (Cambridge: Cambridge University Press)
- [2] Bernas H (ed) 2010 *Materials Science with Ion Beams* (Berlin: Springer)
- [3] Krasheninnikov A V and Banhart F 2007 *Nat. Mater.* **6** 723–33
- [4] Krasheninnikov A V and Nordlund K 2010 *J. Appl. Phys.* **107** 071301
- [5] Dhara S 2007 *Crit. Rev. Solid State Mater. Sci.* **32** 1–50
- [6] Lin Z, Carvalho B R, Kahn E, Lv R, Rao R, Terrones H, Pimenta M A and Terrones M 2016 *2D Mater.* **3** 022002
- [7] Lemme M C, Bell D C, Williams J R, Stern L A, Baugher B W H, Jarillo-Herrero P and Marcus C M 2009 *ACS Nano* **3** 2674–6
- [8] Lin J et al 2014 *Nat. Nanotechnol.* **9** 436–42
- [9] Jin C, Lan H, Peng L, Suenaga K and Iijima S 2009 *Phys. Rev. Lett.* **102** 1–4
- [10] Liu X et al 2013 *Nat. Commun.* **4** 1776
- [11] Alcoltekin S, Bukowska H, Peters T, Osmani O, Monnet I, Alzahrer I, D'Etat B B, Lebius H and Schleberger M 2011 *App. Phys. Lett.* **98** 103103
- [12] Cretu O, Komsa H P, Lehtinen O, Algara-Siller G, Kaiser U, Suenaga K and Krasheninnikov A V 2014 *ACS Nano* **8** 11950–7
- [13] Ryu G H, Lee J, Kim N Y, Lee Y, Kim Y, Kim M J, Lee C and Lee Z 2016 *2D Mater.* **3** 014002
- [14] Sutter E, Huang Y, Komsa H P, Ghorbani-Asl M, Krasheninnikov A V and Sutter P 2016 *Nano Lett.* **16** 4410–6
- [15] Rotunno E, Fabbri F, Cinquanta E, Kaplan D, Longo M, Lazzarini L, Molle A, Swaminathan V and Salviati G 2016 *2D Mater.* **3** 025024
- [16] Ni Z, Li Q, Yan L, Gong J and Zhu D 2008 *Carbon* **46** 376–8
- [17] Terrones M, Banhart F, Grobert N, Charlier J C, Terrones H and Ajayan P M 2002 *Phys. Rev. Lett.* **89** 075505
- [18] Bangert U, Pierce W, Kepaptsoglou D M, Ramasse Q, Zan R, Gass M H, Van den Berg J A, Boothroyd C B, Amani J and Hofsäss H 2013 *Nano Lett.* **13** 4902–7
- [19] Kepaptsoglou D et al 2015 *ACS Nano* **9** 11398–407
- [20] Cress C D, Schmucker S W, Friedman A L, Dev P, Culbertson J C, Lyding J W and Robinson J T 2016 *ACS Nano* **10** 3714–22
- [21] Utke I, Hoffmann P and Melngailis J 2008 *J. Vac. Sci. Technol. B* **26** 1197–276
- [22] Wei X, Wang M, Bando Y and Golberg D 2011 *ACS Nano* **5** 2916–22
- [23] Wang H et al 2012 *Nano Lett.* **12** 141–4
- [24] López-Polín G, Gómez-Navarro C, Parente V, Guinea F, Katsnelson M I, Pérez-Murano F and Gómez-Herrero J 2014 *Nat. Phys.* **11** 26–31
- [25] Kalbac M, Lehtinen O, Krasheninnikov A V and Keinonen J 2013 *Adv. Mater.* **25** 1004–9
- [26] Tongay S et al 2013 *Sci. Rep.* **3** 2657
- [27] Lehtinen O, Kotakoski J, Krasheninnikov A V, Tolvanen A, Nordlund K and Keinonen J 2010 *Phys. Rev. B* **81** 153401
- [28] Bai Z, Zhang L and Liu L 2015 *J. Phys. Chem. C* **119** 26793–802
- [29] Wang Q H, Kalantar-Zadeh K, Kis A, Coleman J N and Strano M S 2012 *Nat. Nanotechnol.* **7** 699–712
- [30] Chhowalla M, Shin H S, Eda G, Li L J, Loh K P and Zhang H 2013 *Nat. Chem.* **5** 263–75
- [31] Liu G B, Xiao D, Yao Y, Xu X and Yao W 2015 *Chem. Soc. Rev.* **44** 2643–63
- [32] Lin Z et al 2016 *2D Mater.* **3** 042001
- [33] Ochedowski O, Marinov K, Wilbs G, Keller G, Scheuschner N, Severin D, Bender M, Maultzsch J, Tegude F J and Schleberger M 2013 *J. Appl. Phys.* **113**
- [34] Madau L, Ochedowski O, Lebius H, Ban-d'Etat B, Naylor C, Johnson A, Kotakoski J and Schleberger M 2017 *2D Mater.* **4** 015034
- [35] Iberi V et al 2016 *Sci. Rep.* **6** 30481
- [36] Stanford M G et al 2016 *Sci. Rep.* **6** 27276
- [37] Mathew S et al 2012 *App. Phys. Lett.* **101** 102103
- [38] Ma Q et al 2013 *J. Phys.: Condens. Matter.* **25** 252201
- [39] Ma Q et al 2014 *ACS Nano* **8** 4672–7
- [40] Fox D S et al 2015 *Nano Lett.* **15** 5307–13
- [41] Smith R (ed) 1997 *Atomic and Ion Collisions in Solids and at Surfaces: Theory, Simulation and Applications* (Cambridge: Cambridge University Press)
- [42] Komsa H P, Kotakoski J, Kurasch S, Lehtinen O, Kaiser U and Krasheninnikov A V 2012 *Phys. Rev. Lett.* **109** 035503
- [43] Plimpton S 1995 *J. Comput. Phys.* **117** 1–19
- [44] Ziegler J F and Biersack J P 1985 *The Stopping and Range of Ions in Matter* (Boston, MA: Springer) pp 93–129
- [45] Peng Q, Ji W and De S 2013 *Nanoscale* **5** 695–703
- [46] Holmström E, Toikka L, Krasheninnikov A V and Nordlund K 2010 *Phys. Rev. B* **82** 045420
- [47] Perdew J P, Burke K and Ernzerhof M 1996 *Phys. Rev. Lett.* **77** 3865–8
- [48] Atomistix ToolKit version 2015, QuantumWise A/S (www.quantumwise.com)
- [49] Datta S 2005 *Quantum Transport: Atom to Transistor* (New York: Cambridge University Press)
- [50] Ghorbani-Asl M, Kuc A, Miró P and Heine T 2016 *Adv. Mater.* **28** 853–6
- [51] Ghorbani-Asl M, Bristowe P D, Koziol K, Heine T and Kuc A 2016 *2D Mater.* **3** 25018
- [52] Liang T, Phillpot S R and Sinnott S B 2009 *Phys. Rev. B* **79** 245110
- [53] Stewart J A and Spearot D E 2013 *Modelling Simul. Mater. Sci. Eng.* **21** 45003
- [54] Jiang J W, Park H S and Rabczuk T 2013 *J. App. Phys.* **114** 064307
- [55] Jiang J W 2015 *Nanotechnology* **26** 315706
- [56] Kandemir A, Yapicioglu H, Kinaci A, Cagin T and Sevik C 2016 *Nanotechnology* **27** 55703
- [57] Komsa H P and Krasheninnikov A V 2015 *Phys. Rev. B* **91** 125304
- [58] Komsa H P, Kurasch S, Lehtinen O, Kaiser U and Krasheninnikov A V 2013 *Phys. Rev. B* **88** 35301
- [59] Zhou W, Zou X, Najmaei S, Liu Z, Shi Y, Kong J, Lou J, Ajayan P M, Yakobson B I and Idrobo J C 2013 *Nano Lett.* **13** 2615–22
- [60] Dang K Q and Spearot D E 2014 *J. Appl. Phys.* **116** 013508
- [61] Lince J R, Stewart T B, Hills M M, Fleischauer P D, Yarmoff J A and Taleb-Ibrahimi A 1989 *Surf. Sci.* **210** 387–405
- [62] McIntyre N S, Spevack P A, Beamson G and Briggs D 1990 *Surf. Sci.* **237** L390–L397
- [63] Lehtinen O, Dumur E, Kotakoski J, Krasheninnikov A V, Nordlund K and Keinonen J 2011 *Nucl. Instrum. Methods Phys. Res. B* **269** 1327–31
- [64] Park J B, France C B and Parkinson B A 2005 *J. Vac. Sci. Technol. B* **23** 1532–42
- [65] Hlawacek G, Veligura V, van Gastel R and Poelsema B 2014 *J. Vac. Sci. Technol. B* **32** 020801
- [66] Sim D M, Kim M, Yim S, Choi M J, Choi J, Yoo S and Jung Y S 2015 *ACS Nano* **9** 12115–23
- [67] Britnell L, Gorbachev R V, Geim A K, Ponomarenko L A, Mishchenko A, Greenaway M T, Fromhold T M, Novoselov K S and Eaves L 2013 *Nat. Commun.* **4** 1794
- [68] Mahjouri-Samani M et al 2016 *Nano Lett.* **16** 5213–20
- [69] Pandey M, Rasmussen F A, Kuhar K, Olsen T, Jacobsen K W and Thygesen K S 2016 *Nano Lett.* **16** 2234–9
- [70] Stukowski A 2010 *Modelling Simul. Mater. Sci. Eng.* **18** 15012

Chemical and Electronic Repair Mechanism of Defects in MoS₂ Monolayers

Anja Förster,^{†,‡,¶,Ⓜ} Sibylle Gemming,^{‡,§,||} Gotthard Seifert,^{‡,¶,Ⓜ,Ⓛ} and David Tománek^{*,†,Ⓜ}

[†]Physics and Astronomy Department, Michigan State University, East Lansing, Michigan 48824, United States

[‡]Center for Advancing Electronics Dresden (cfaed), 01062 Dresden, Germany

[¶]Theoretical Chemistry, Technische Universität Dresden, 01062 Dresden, Germany

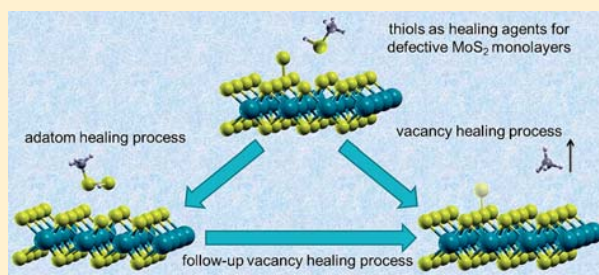
[§]Helmholtz-Zentrum Dresden-Rossendorf, Institute of Ion Beam Physics and Materials Research, Bautzner Landstrasse 400, 01328 Dresden, Germany

^{||}Institute of Physics, Technische Universität Chemnitz, 09107 Chemnitz, Germany

[Ⓛ]National University of Science and Technology, MISIS, 119049 Moscow, Russia

ABSTRACT: Using *ab initio* density functional theory calculations, we characterize changes in the electronic structure of MoS₂ monolayers introduced by missing or additional adsorbed sulfur atoms. We furthermore identify the chemical and electronic function of substances that have been reported to reduce the adverse effect of sulfur vacancies in quenching photoluminescence and reducing electronic conductance. We find that thiol-group-containing molecules adsorbed at vacancy sites may reinsert missing sulfur atoms. In the presence of additional adsorbed sulfur atoms, thiols may form disulfides on the MoS₂ surface to mitigate the adverse effect of defects.

KEYWORDS: transition metal dichalcogenides, 2D materials, *ab initio* calculations, electronic structure, defects



There is growing interest in two-dimensional (2D) transition metal dichalcogenide (TMD) semiconductors, both for fundamental reasons and as potential components in flexible, low-power electronic circuitry and for sensor applications.^{1–3} Molybdenum disulfide, MoS₂, is a prominent representative of this class of TMDs. A free-standing, perfect 2D MoS₂ monolayer possesses a direct band gap of 1.88 eV at the *K*-point in the Brillouin zone.^{4,5} Most commonly used production methods for MoS₂ monolayers are chemical vapor deposition (CVD) and mechanical exfoliation of the layered bulk material,^{6–8} as well as sputter growth atomic layer deposition⁹ (ALD) of the precursor MoO₃ and subsequent conversion to the disulfide under reducing conditions and at high temperatures.^{10,11} A direct ALD process using H₂S and MoCl₅¹² or Mo(CO)₆¹³ is another possibility to obtain MoS₂ monolayers. The CVD technique is probably best suited for mass production, but the synthesized MoS₂ layers lack atomic perfection. The most common defects in these layers are sulfur and molybdenum vacancies, as well as additional adsorbed sulfur atoms.^{14–19} Eliminating or at least reducing the adverse effect of such defects is imperative to improve the optoelectronic and transport properties of TMDs.

In search of ways to mitigate the adverse effect of defects, different methods have been suggested, including exposure of MoS₂ to superacids²⁰ or thiols.^{21,22} In the related MoSe₂

system, Se vacancies could be filled by S atoms from an adjacent MoS₂ layer.²³ In the present study, we focus on the reactions of thiols with defective MoS₂ monolayers.

First, we characterize changes in the electronic structure of MoS₂ monolayers introduced by missing or additional adsorbed sulfur atoms using *ab initio* density functional theory (DFT) calculations. We provide microscopic information about the chemical and electronic function of thiols as a theoretical background for the understanding of the successful use of thiols, which have been reported to reduce the adverse effect of sulfur vacancies in quenching photoluminescence and to improve the electronic conductance of defective MoS₂. We found that adsorbed thiols may reinsert missing sulfur atoms at vacancy sites. We also found that in the presence of sulfur adatoms thiols will form disulfides on the MoS₂ surface, which mitigates the adverse effect of defects.

In Figure 1 we display the structure of a defective MoS₂ monolayer with a sulfur monovacancy (V) and an additional sulfur adatom (A), since these defects are known to significantly affect the electronic properties of MoS₂.²⁴ The formation energy of the sulfur vacancy is 2.71 eV, and that of

Received: June 14, 2017

Accepted: September 15, 2017

Published: September 15, 2017

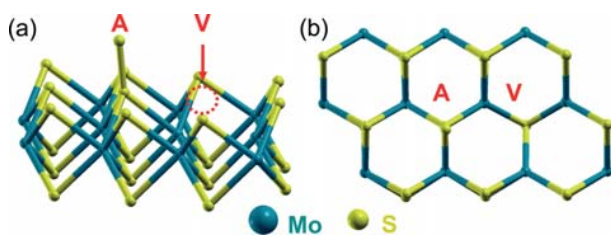


Figure 1. (a) Perspective and (b) top view of the optimized geometry of an MoS₂ monolayer containing a sulfur monovacancy (V) and a sulfur adatom (A).

the sulfur adatom is 1.07 eV. Consequently, the recombination energy of a sulfur vacancy and a sulfur adatom is -1.89 eV. In spite of the large energy gain, no spontaneous healing will occur in a system with both defect types present due to the high activation barrier of ≈ 1.5 eV for this reaction. The listed defect formation energies are in agreement with a study reporting the effect of various defect types on the electronic structure of MoS₂²⁵ and also with a study of vacancy defects.²⁶

Defects affect drastically the electronic structure in the vicinity of the Fermi level. Setting apart the inadequacy of DFT-PBE (Perdew–Burke–Ernzerhof) calculations for quantitative predictions of band gaps, we should note that in our computational approach with (large) supercells and periodic boundary conditions also defects form a periodic array. In spite of their large separation, defect states evolve into narrow bands that may affect the band structure of a pristine MoS₂ monolayer. The effect of a sulfur monovacancy, as well as that of a sulfur adatom, on the density of states (DOS) of a MoS₂ monolayer around the band gap region is shown in Figure 2.

As seen in Figure 2c, sulfur monovacancies introduce defect states within the band gap, and their superlattice shifts the DOS down by 0.16 eV with respect to the pristine lattice. The defect states are localized around the vacancy as seen in Figure 2a. The effect of a superlattice of sulfur adatoms, addressed in Figure 2b and d, is to reduce the DFT band gap from 1.88 to 1.72 eV, in agreement with published results.^{24,25}

Defect sites play an important role as catalytically active centers¹³ and as sites for functionalization reactions of 2D MoS₂.²⁷ Sulfur vacancies in particular are considered to be important nucleation sites for a functionalization with thiol molecules R–SH. The likely possibility of an adsorbed thiol group transferring a sulfur atom to the vacancy and thus repairing the defect is particularly appealing. In this case, the detached hydrogen atom may reconnect with the remaining R to form R–H and fill the vacancy site of MoS₂ with sulfur, as



where MoS₂^V denotes the MoS₂ layer with a sulfur vacancy.

An alternative reaction has been proposed to benefit from the STM tip current in an STM study.²² In the first step of reaction 2, similar to reaction 1, a hydrogen atom is removed from the thiol as its sulfur atom fills the previous vacancy, determining the reaction barrier for both reactions 1 and 2a. The removed hydrogen atom will then form H₂ and desorb from the MoS₂ surface. The remaining R is still bound to the sulfur atom, adsorbed at the sulfur vacancy site. The final assumption of the proposed mechanism²² is that the R-groups are removed with the support of the STM tip, as represented in reaction 2b.

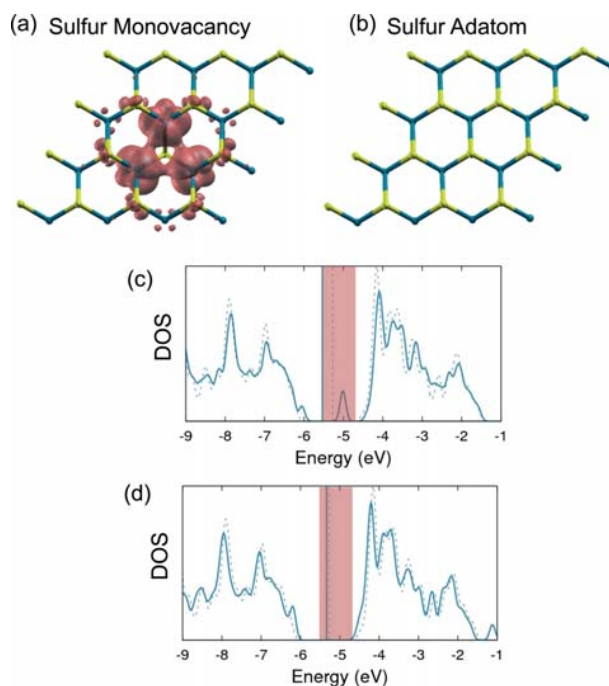
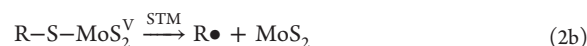
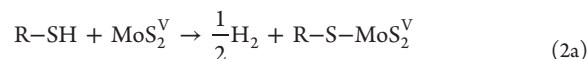
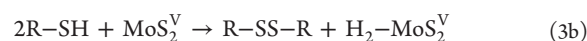
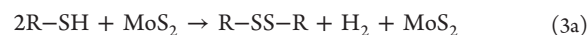


Figure 2. Ball-and-stick models of (a) a sulfur vacancy defect and (b) a sulfur adatom defect in a MoS₂ monolayer. Density of states (DOS) of MoS₂ with (c) a vacancy and (d) an adatom defect. The DOS and the position of the Fermi level are shown by solid blue lines in defective lattices and by dotted blue lines in the corresponding pristine lattices in (c) and (d). The DOS has been convoluted by a Gaussian with a full-width at half-maximum of 0.1 eV. The energy range of interest in the gap of the pristine lattice is highlighted in red. The local density of states (LDOS), representing the charge density associated with this highlighted energy range, is represented by an isosurface and superposed to the structure of a vacancy defect in (a) and an adatom defect in (b). The isosurface value in the LDOS plots is 0.003 e/bohr³.



There is evidence in the literature supporting both reaction 1 (refs 21, 28, 29) and reaction 2 (ref 22).

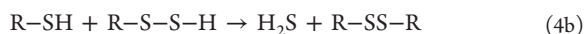
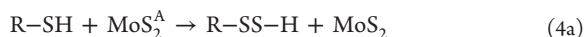
The authors of ref 30 propose yet another reaction (3a). Instead of the thiol molecules repairing the sulfur vacancy, they form an adsorbed R–SS–R disulfide at the surface of MoS₂ while releasing a hydrogen molecule. We also considered the possibility that instead of desorbing, the hydrogen molecule will fill the vacancy defect as described in reaction 3b,



Based on a previous study³¹ and the observation of H₂S as well as H₃C=CH₃ during the reaction of C₂H₅SH with bulk MoS₂ in ref 28, we also considered a sulfur atom adsorbed on the MoS₂ surface, identified as MoS₂^A, as the driving force for the observed disulfide formation.

In this case, the reaction to form the disulfide R–SS–R is divided into the following two steps. In reaction 4a, one thiol reacts with the adatom to R–S–S–H and, in the follow-up

reaction 4b with a second thiol, to R–S–S–R. An alternative reaction with a sulfur vacancy following reaction 4a is also possible. Similar to reaction 1, the SH-group of R–S–S–H can heal the vacancy defect, leading to the reduction of R–S–S–H to the thiol R–S–H in reaction 4c,



To better understand the above reaction mechanisms 1–4, we performed DFT calculations to compare the energy associated with the pathways of these reactions. For the sake of easy understanding, we consider the small methanethiol molecule CH_3SH as a representative of thiols.

We limit our study of vacancy repair processes to reactions with MoS_2 monolayers that contain one sulfur monovacancy per unit cell. We analyze which reactions with thiols are favorable to repair vacancy and adatom defects. Our results also unveil the likely cause of apparent contradictions in the interpretation of experimental results obtained by different researchers.

RESULTS AND DISCUSSION

Vacancy Repair. The majority of published results indicate that thiol molecules interacting with sulfur-deficient MoS_2 may fill in sulfur atoms at the vacancy defect sites. Reaction pathways for the two vacancy-healing reactions 1 and 2a, which have been proposed in the literature,^{22,28,29} are sketched in Figure 3. We note that reaction 1 has been studied in greater detail for a different thiol²¹ and agrees with our findings for the model compound $\text{H}_3\text{C-SH}$.

We find that reactions 1 and 2a are both exothermic and require crossing only a low activation barrier of 0.22 eV, since they share the same transition state shown in Figure 3. The larger energy gain $E_{\text{R}} = -3.09$ eV in reaction 1 in comparison to -0.90 eV in reaction 2a suggests that the former reaction is thermodynamically preferred.

Figure 4a shows the DOS and partial densities of states (PDOS), projected on individual atoms, of the product of reaction 1. Figure 4b provides the corresponding information for reaction 2a, and Figure 4c provides a detailed view of the PDOS for the CH_3 -group and the connected sulfur atom. In both cases, the defect states associated with sulfur monovacancies have been removed. In the final state of reaction 1 the DOS is completely restored to the undamaged state of the semiconductor. For reaction 2a, on the other hand, the Fermi level is shifted to the lower edge of the conduction band due to the CH_3 -group. Therefore, only the preferred repair reaction 1 leads to both an electronic and a chemical repair of MoS_2 .

Disulfide Formation. A different reaction scenario (3a) has been proposed in ref 30, suggesting that disulfides are formed when thiols interact with MoS_2 . We investigated the MoS_2 surface both in its pristine state and in the presence of sulfur vacancies to clarify the differences in the catalytic potential for disulfide formation. Figure 5 illustrates reaction 3a on pristine MoS_2 and reaction 3b on a sulfur-deficient MoS_2 substrate. The schematic reaction profile indicates that both reactions involve significant activation barriers. As seen in Figure 5, reaction 3a is endothermic with a reaction energy of $E_{\text{R}} = 0.39$ eV and involves a high activation barrier of 2.91 eV. Reaction 3b near a sulfur monovacancy is only slightly endothermic, with a

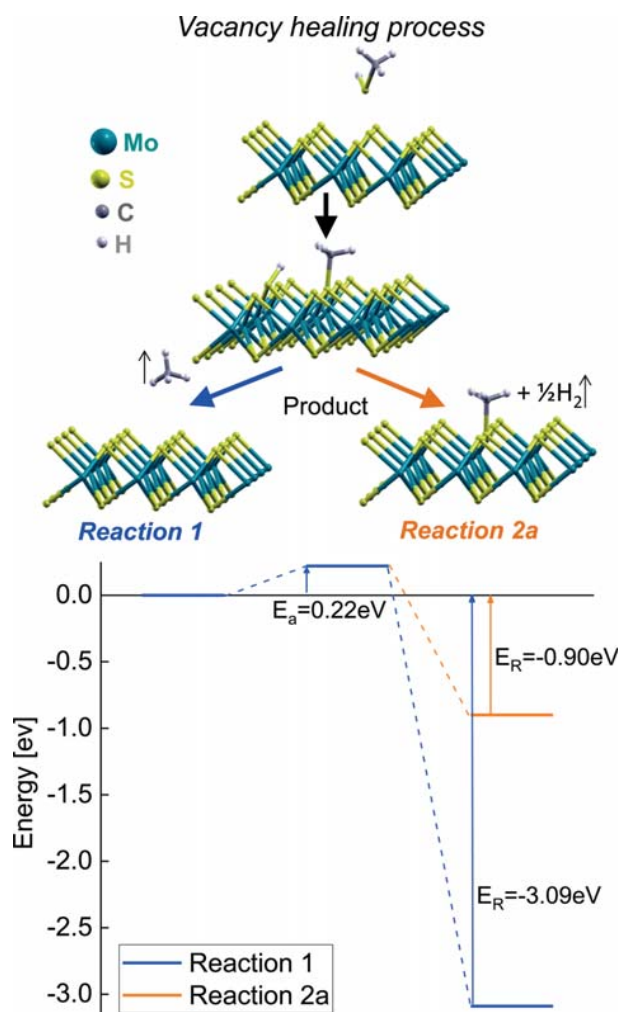


Figure 3. Reaction scheme for the sulfur vacancy healing process caused by exposure of MoS_2 with vacancies to CH_3SH . E_{R} denotes the reaction energy and E_{a} the activation barrier. The same initial state can lead to two different final states *via* the same transition state. The favorable reaction 1, shown in dark blue, leads to a free CH_4 molecule. The energetics of reaction 2a is displayed in light orange.

reaction energy $E_{\text{R}} = 0.02$ eV, and involves a somewhat lower activation barrier of 2.13 eV. Thus, reaction 3b is energetically more favorable than reaction 3a.

The near-neutral reaction energy of reaction 3b can be explained by the Kubas interaction of transition metal $\eta^2\text{-H}_2$ complexes.^{32,33} It means that the excess H_2 molecule in the product of reaction 3b, which is attached to an Mo atom at the sulfur vacancy site and indicated by a circle in Figure 5, still retains the H–H bond character. According to ref 34, the Kubas interaction energy is in the range of 0.2–0.4 eV and thus in agreement with the reaction energy difference of 0.37 eV between the transition and final states of reactions 3a and 3b.

The Kubas interaction also reduces the reaction barrier and degree of endothermicity considerably. Nevertheless, reactions 3a and 3b are not competitive in comparison with the strongly exothermic reaction 1 with $E_{\text{R}} = -3.09$ eV in thermodynamic equilibrium.

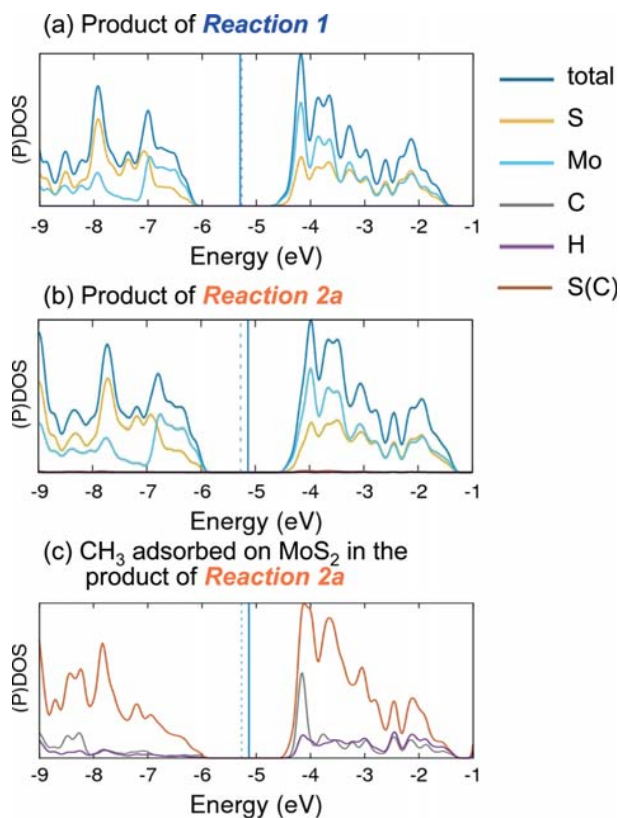


Figure 4. Electronic structure of products of the vacancy healing process shown in Figure 3. Total density of states (DOS) and partial densities of states (PDOS) of the products of reactions (a) 1 and (b) 2a. (c) PDOS of the CH₃ molecule bonded to a sulfur atom in an MoS₂ monolayer. The PDOS of the sulfur atom connected to C in CH₃, S(C), is shown by the brown line. All DOS and PDOS functions have been convoluted by a Gaussian with a full-width at half-maximum of 0.1 eV. The position of the Fermi level is shown by solid blue lines in defective lattices and by dotted blue lines in the corresponding pristine lattices.

The PDOS functions characterizing the products of reactions 3a and 3b, visualized in Figure 5, are shown in Figure 6. The product of reaction 3b still contains a defect state in the gap region, indicating that the chemisorbed H₂ molecule is incapable of electronically repairing the effect of the sulfur vacancy. This is seen in the PDOS of the Mo atoms of the Kubas complex surrounding the vacancy defect in Figure 6c. The product of reaction 3a, on the other hand, shows no indication of a defect state, since the vacancy-free MoS₂ monolayer is not affected much by the physisorbed disulfide, as seen in the PDOS of Figure 6a.

We can thus conclude that the disulfide formation reaction 3a, suggested in ref 30, is endothermic. The alternative reaction 3b on a sulfur-deficient MoS₂ substrate displays a lower activation barrier and an end-product stabilized by the Kubas interaction, but is still weakly endothermic and thus unlikely. In the following, we propose an alternative pathway toward disulfide formation.

Adatom Repair. The postulated alternative reaction requires extra sulfur atoms adsorbed on the MoS₂ surface, which act as nucleation sites for the disulfide formation. The reaction leading to the formation of disulfide R–SS–R in the presence of sulfur adatoms consists of two steps, described by

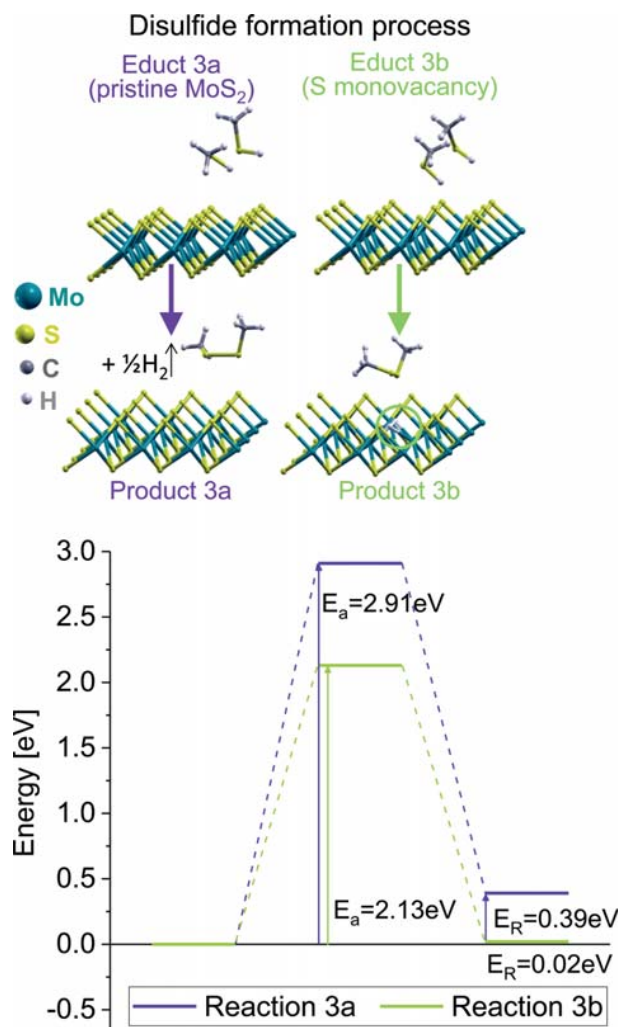


Figure 5. Reaction scheme of the disulfide formation process involving exposure of an MoS₂ monolayer to two CH₃SH molecules. E_R denotes the reaction energy and E_a the activation barrier. Reaction 3a, shown in dark purple, occurs on pristine MoS₂. Reaction 3b, shown in light green, occurs on a sulfur-deficient MoS₂ substrate.

reactions 4a and 4b, as well as the alternative reaction 4c following reaction 4a, as shown in Figure 7.

In reaction 4a, a CH₃SH molecule interacts with the reactive sulfur adatom to methylhydrodisulfide (CH₃SSH), releasing –0.86 eV due to the formation of a stable disulfide bond. The estimated activation barrier for this reaction is close to 1 eV, which is considerably lower than the values for the corresponding reactions 3a and 3b in absence of an extra sulfur adatom.

Electronic structure changes during the adatom healing process are displayed in Figure 8. The DOS of the product of reaction 4a, shown in Figure 8b, shows no defect-related states in the band gap, indicating chemical and electronic repair of the sulfur adatom defect that is seen in Figure 8a.

In the subsequent reaction 4b, shown in Figure 7, a second CH₃SH molecule interacts with the methylhydrodisulfide CH₃SSH, leading to the exchange of the hydrogen atom with a methyl group and formation of hydrogen sulfide (H₂S) as a side product. This reaction is mildly exothermic, with an overall

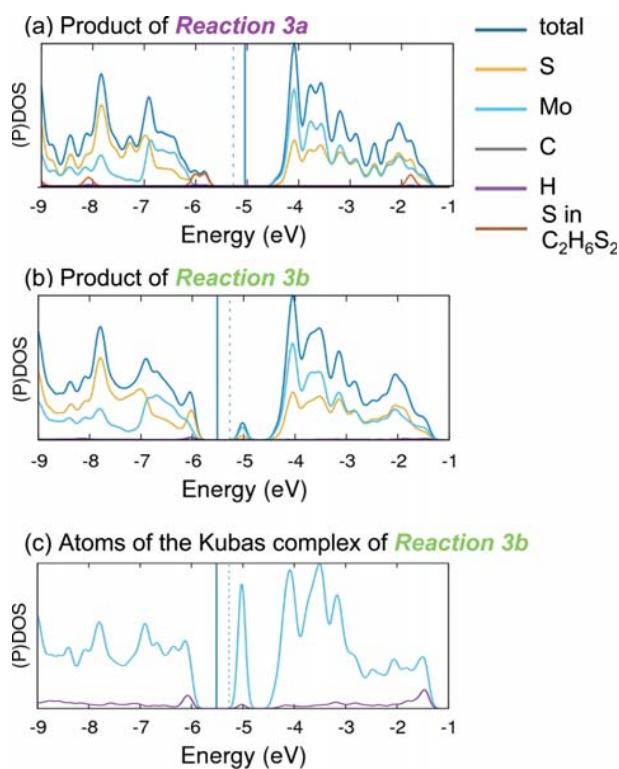


Figure 6. Electronic structure of products of the disulfide formation process shown in Figure 5. Total density of states (DOS) and partial densities of states (PDOS) of the products of reactions (a) 3a and (b) 3b. (c) PDOS of the 3 Mo atoms and the H₂ molecule attached to the vacancy that form the Kubas complex in the product of reaction 3b. All DOS and PDOS functions have been convoluted by a Gaussian with a full-width at half-maximum of 0.1 eV. The position of the Fermi level is shown by solid blue lines in defective lattices and by dotted blue lines in the corresponding pristine lattices.

reaction energy of -0.18 eV. Even though the combined reaction 4a and 4b for the formation of CH₃SSCH₃ is strongly exothermic with a net energy gain of -1.05 eV, the activation barrier for the ligand exchange in reaction 4b is prohibitively high with $E_a \approx +3$ eV, which essentially suppresses the formation of CH₃SSCH₃ following reaction 4a.

Therefore, we investigated reaction 4c as an alternative follow-up process to reaction 4a. In reaction 4c, the CH₃SSH molecule interacts with a nearby sulfur vacancy defect. This reaction is similar to the vacancy healing reaction 1 and consequently is strongly exothermic with a reaction energy of -2.81 eV. Reaction 4c is barrier-free and thus occurs spontaneously. As seen in Figure 8c, describing the product of reaction 4c, the defect-related state above E_F has been removed from the DOS. This means that following the adatom repair and disulfide formation, reaction 4a, reaction 4c will take place in case that sulfur vacancies are also present. The two reactions will thus heal both vacancy and adatom defects.

Our above considerations offer an attractive explanation why disulfide formation was observed in ref 30, but not in refs 21, 22, 28, and 29. Initially, reactions 1 and 4a plus 4c have taken place in all samples that contained vacancies. Vacancy healing as the primary outcome of reactions reported in refs 21, 22, 28, and 29 could likely be achieved due to an abundance of vacancies in the samples used. We may speculate that the MoS₂

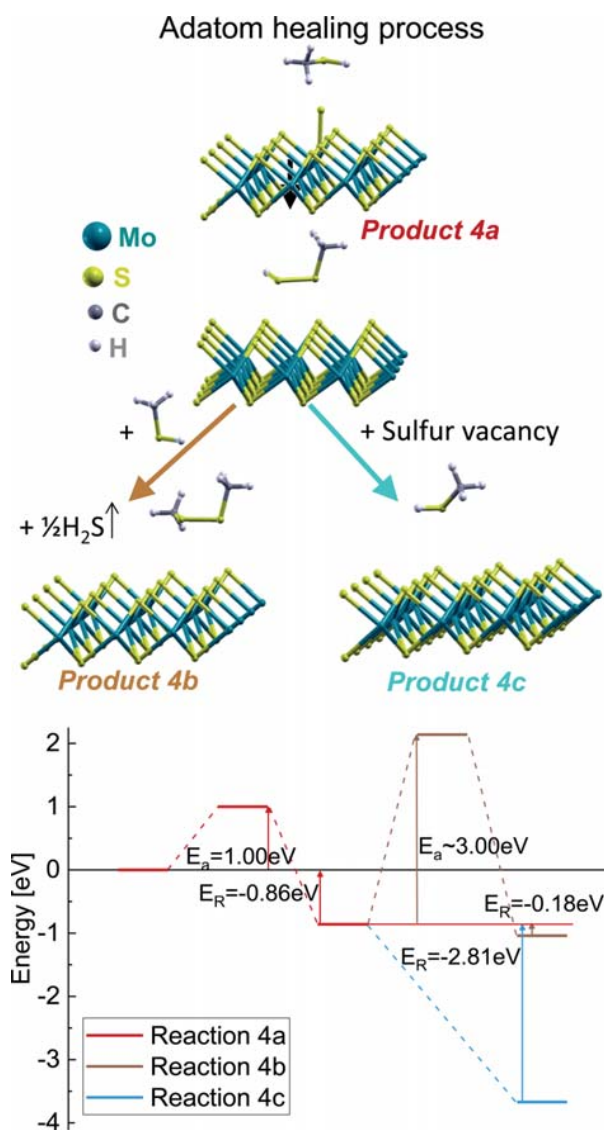


Figure 7. Reaction scheme of the adatom healing process that starts with reaction 4a and leads to disulfide formation in the presence of extra sulfur atoms on MoS₂, shown in dark red. Subsequent ligand exchange reaction 4b is shown in brown. Alternative subsequent vacancy repair reaction 4c is shown in light blue. E_R denotes the reaction energy and E_a the activation barrier.

sample of ref 30 contained more sulfur adatoms than sulfur vacancies. In that case, all vacancy defects could be repaired, but some adatom defects were left unrepaired in the sample of ref 30. At this point, lack of vacancy defects would block reactions 1 and 4c. The only viable reaction was 4a, which repaired adatom defects, leaving a pristine MoS₂ surface behind with disulfide as a byproduct. This speculative assumption is also consistent with the observation that the electronic structure of MoS₂ has remained unaffected by the reaction leading to the formation of disulfide.³⁰

CONCLUSIONS

We studied three different reaction paths of thiols, represented by methanethiol (CH₃SH), with a defective 2D MoS₂ monolayer. We showed that the repair of sulfur monovacancies

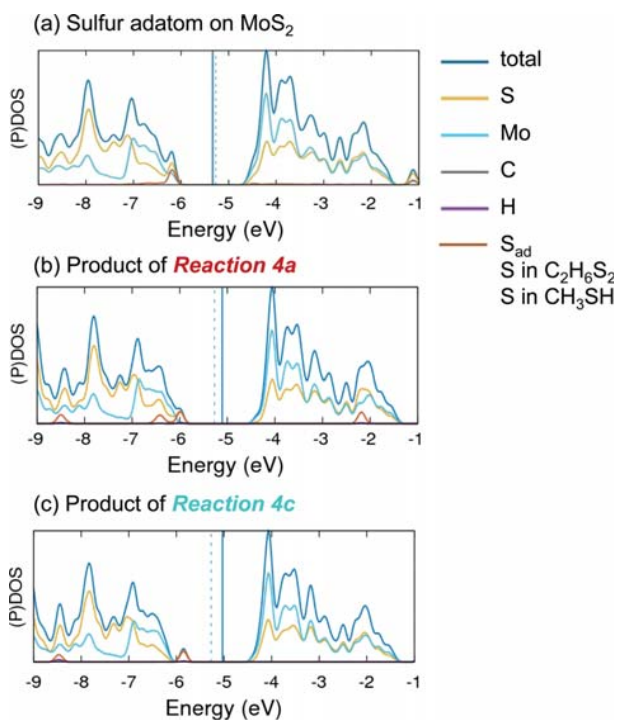


Figure 8. Electronic structure of products of the adatom healing process shown in Figure 7. Total density of states (DOS) and partial densities of states (PDOS) of (a) MoS₂ with a sulfur adatom (without CH₃SH), (b) product of reaction 4a, and (c) product of reaction 4c. All DOS and PDOS functions have been convoluted by a Gaussian with a full-width at half-maximum of 0.1 eV. The position of the Fermi level is shown by solid blue lines in defective lattices and by dotted blue lines in the corresponding pristine lattices.

by adsorbed CH₃SH is an exothermic reaction releasing up to 3 eV. In another possible reaction between CH₃SH and MoS₂, leading to the formation of disulfide, we found that the presence of sulfur vacancies lowers the reaction barrier due to the Kubas interaction at the defect site. The corresponding reaction involving MoS₂ with sulfur adatoms instead of vacancies, on the other hand, leads to disulfide formation and releases about 0.9 eV. In the presence of sulfur vacancies, the formed disulfides will immediately reduce to thiols while simultaneously healing the vacancy defect. We can therefore conclude that, regardless of interim disulfide formation, thiols always lead to a chemical repair of available sulfur vacancies by filling-in the missing sulfur atoms and consequently eliminating vacancy-related defect states in the gap.

THEORETICAL METHODS

To obtain insight into the reaction processes, we performed DFT calculations using the SIESTA code.³⁵ We used *ab initio* Troullier–Martins pseudopotentials³⁸ and the PBE exchange–correlation functional³⁶ throughout the study. Except for sulfur, all pseudopotentials used were obtained from the online resource in ref 39. The pseudopotential of sulfur has been generated without core corrections using the ATM code in the SIESTA suite and the parameters listed in ref 39. All pseudopotentials were tested against atomic all-electron calculations. We used a double- ζ basis set including polarization orbitals (DZP) to represent atoms in crystal lattices, 140 Ry as the mesh cutoff energy for the Fourier transform of the charge density, and 0 K for the electronic temperature. We used periodic boundary

conditions with large supercells spanned by the lattice vectors $\vec{a}_1 = (12.84, 0.00, 0.00)$ Å, $\vec{a}_2 = (6.42, 11.12, 0.00)$ Å, $\vec{a}_3 = (0.00, 0.00, 22.23)$ Å to represent pristine and defective 2D MoS₂ lattices. The unit cells of defect-free MoS₂ contained 16 molybdenum and 32 sulfur atoms and were separated by a vacuum region of ≈ 15 Å normal to the layers. The Brillouin zone was sampled by a $4 \times 4 \times 1$ k -point grid³⁷ and its equivalent in larger supercells.

The above input parameters were found to guarantee convergence. In particular, we found that using the larger triple- ζ polarized (TZP) instead of the DZP basis and increasing the mesh cutoff energy affected our total energy differences by typically less than 0.01 eV. We furthermore validated the *ab initio* pseudopotential approach used in the SIESTA code by comparing to results of the all-electron SCM-Band code⁴¹ and found that energy differences obtained using the two approaches differed typically by less than 0.3 eV.

All geometries have been optimized using the conjugate gradient method,⁴⁰ until none of the residual Hellmann–Feynman forces exceeded 10^{-2} eV/Å. In addition to the default density matrix convergence, we also demanded that the total energy should reach the tolerance of $\lesssim 10^{-4}$ eV. To eliminate possible artifacts associated with local minima, we verified initial and final state geometries by performing canonical molecular dynamics (MD) simulations using an NVT–Nosé thermostat with $T = 273.15$ K and 1 fs time steps.

Due to the complexity of the reaction energy hypersurface and the large number of relevant degrees of freedom, approaches such as the nudged elastic band, which are commonly used to determine the reaction path including transition states, turned out to be extremely demanding on computer resources. We focused on transition states only and initiated our search by running canonical MD simulations starting from a set of educated guesses for the geometry. Following the atomic trajectories, we could identify a saddle point in the energy hypersurface, where all forces acting on atoms vanished, and postulated this point in configurational space as a transition state. To confirm this postulate, we ran MD simulations starting at a slightly altered geometry of the postulated transition state. We concluded that the postulated transition state is indeed the real transition state once all trajectories reached either the initial (educt) or the final (product) state. The activation barrier was determined by the energy difference between the initial and the transition state.

AUTHOR INFORMATION

Corresponding Author

*E-mail: tomanek@pa.msu.edu.

ORCID

Anja Förster: 0000-0002-2203-8662

David Tománek: 0000-0003-1131-4788

Notes

The authors declare no competing financial interest.

ACKNOWLEDGMENTS

We thank Jie Guan and Dan Liu for useful discussions and Garrett B. King for carefully checking the bibliography. This study was supported by the NSF/AFOSR EFRI 2-DARE grant number #EFMA-1433459. Computational resources have been provided by the Michigan State University High Performance Computing Center and the Center of Information Services and High Performance Computing (ZIH) at TU Dresden. A.F., S.G., and G.S. acknowledge funding from the Center for Advancing Electronics Dresden (cfaed). A.F. acknowledges the hospitality of Michigan State University and the cfaed Inspire Grant. S.G. acknowledges funding from the Initiative and Networking Funds of the President of the Helmholtz Association *via* the W3 Programme. G.S. also acknowledges support from NUST “MISis” (No. K3-2017-064).

REFERENCES

- (1) Li, H.; Yin, Z.; He, Q.; Li, H.; Huang, X.; Lu, G.; Fam, D. W. H.; Tok, A. I. Y.; Zhang, Q.; Zhang, H. Fabrication of Single- and Multilayer MoS₂ Film-Based Field-Effect Transistors for Sensing NO at Room Temperature. *Small* **2012**, *8*, 63–67.
- (2) Castellanos-Gomez, A.; van Leeuwen, R.; Buscema, M.; van der Zant, H. S.; Steele, G. A.; Venstra, W. J. Single-Layer MoS₂ Mechanical Resonators. *Adv. Mater.* **2013**, *25*, 6719–6723.
- (3) Chang, H.-Y.; Yang, S.; Lee, J.; Tao, L.; Hwang, W.-S.; Jena, D.; Lu, N.; Akinwande, D. High-Performance, Highly Bendable MoS₂ Transistors with High-K Dielectrics for Flexible Low-Power Systems. *ACS Nano* **2013**, *7*, 5446–5452.
- (4) Ellis, J. K.; Lucero, M. J.; Scuseria, G. E. The Indirect to Direct Band Gap Transition in Multilayered MoS₂ as Predicted by Screened Hybrid Density Functional Theory. *Appl. Phys. Lett.* **2011**, *99*, 261908.
- (5) Splendiani, A.; Sun, L.; Zhang, Y.; Li, T.; Kim, J.; Chim, C.-Y.; Galli, G.; Wang, F. Emerging Photoluminescence in Monolayer MoS₂. *Nano Lett.* **2010**, *10*, 1271–1275.
- (6) Pachauri, V.; Kern, K.; Balasubramanian, K. Chemically Exfoliated Large-Area Two-Dimensional Flakes of Molybdenum Disulfide for Device Applications. *APL Mater.* **2013**, *1*, 032102.
- (7) Li, H.; Wu, J.; Yin, Z.; Zhang, H. Preparation and Applications of Mechanically Exfoliated Single-Layer and Multilayer MoS₂ and WSe₂ Nanosheets. *Acc. Chem. Res.* **2014**, *47*, 1067–1075.
- (8) Varrla, E.; Backes, C.; Paton, K. R.; Harvey, A.; Gholamvand, Z.; McCauley, J.; Coleman, J. N. Large-Scale Production of Size-Controlled MoS₂ Nanosheets by Shear Exfoliation. *Chem. Mater.* **2015**, *27*, 1129–1139.
- (9) Samassekou, H.; Alkabsh, A.; Wasala, M.; Eaton, M.; Walber, A.; Walker, A.; Pitkänen, O.; Kordas, K.; Talapatra, S.; Jayasekera, T.; Mazumdar, D. Viable Route towards Large-Area 2D MoS₂ Using Magnetron Sputtering. *2D Mater.* **2017**, *4*, 021002.
- (10) Kastl, C.; Chen, C. T.; Kuykendall, T.; Shevitski, B.; Darlington, T. P.; Borys, N. J.; Krayev, A.; Schuck, P. J.; Aloni, S.; Schwartzberg, A. M. The Important Role of Water in Growth of Monolayer Transition Metal Dichalcogenides. *2D Mater.* **2017**, *4*, 021024.
- (11) Keller, B. D.; Bertuch, A.; Provine, J.; Sundaram, G.; Ferralis, N.; Grossman, J. C. Process Control of Atomic Layer Deposition Molybdenum Oxide Nucleation and Sulfidation to Large-Area MoS₂ Monolayers. *Chem. Mater.* **2017**, *29*, 2024–2032.
- (12) Browning, R.; Padigi, P.; Solanki, R.; Tweet, D. J.; Schuele, P.; Evans, D. Atomic Layer Deposition of MoS₂ Thin Films. *Mater. Res. Express* **2015**, *2*, 035006.
- (13) Kwon, D. H.; Jin, Z.; Shin, S.; Lee, W.-S.; Min, Y.-S. A Comprehensive Study on Atomic Layer Deposition of Molybdenum Sulfide for Electrochemical Hydrogen Evolution. *Nanoscale* **2016**, *8*, 7180–7188.
- (14) Vancsó, P.; Magda, G. Z.; Petö, J.; Noh, J.-Y.; Kim, Y.-S.; Hwang, C.; Biró, L. P.; Tapasztó, L. The Intrinsic Defect Structure of Exfoliated MoS₂ Single Layers Revealed by Scanning Tunneling Microscopy. *Sci. Rep.* **2016**, *6*, 10.1038/srep29726.
- (15) Addou, R.; McDonnell, S.; Barrera, D.; Guo, Z.; Azcatl, A.; Wang, J.; Zhu, H.; Hinkle, C. L.; Quevedo-Lopez, M.; Alshareef, H. N. Impurities and Electronic Property Variations of Natural MoS₂ Crystal Surfaces. *ACS Nano* **2015**, *9*, 9124–9133.
- (16) Liu, K.-K.; Zhang, W.; Lee, Y.-H.; Lin, Y.-C.; Chang, M.-T.; Su, C.-Y.; Chang, C.-S.; Li, H.; Shi, Y.; Zhang, H. Growth of Large-Area and Highly Crystalline MoS₂ Thin Layers on Insulating Substrates. *Nano Lett.* **2012**, *12*, 1538–1544.
- (17) Lee, Y.-H.; Zhang, X.-Q.; Zhang, W.; Chang, M.-T.; Lin, C.-T.; Chang, K.-D.; Yu, Y.-C.; Wang, J. T.-W.; Chang, C.-S.; Li, L.-J. Synthesis of Large-Area MoS₂ Atomic Layers with Chemical Vapor Deposition. *Adv. Mater.* **2012**, *24*, 2320–2325.
- (18) Zhan, Y.; Liu, Z.; Najmaei, S.; Ajayan, P. M.; Lou, J. Large-Area Vapor-Phase Growth and Characterization of MoS₂ Atomic Layers on a SiO₂ Substrate. *Small* **2012**, *8*, 966–971.
- (19) Hong, J.; Hu, Z.; Probert, M.; Li, K.; Lv, D.; Yang, X.; Gu, L.; Mao, N.; Feng, Q.; Xie, L.; Zhang, J.; Wu, D.; Zhang, Z.; Jin, C.; Ji, W.; Zhang, X.; Yuan, J.; Zhang, Z. Exploring Atomic Defects in Molybdenum Disulfide Monolayers. *Nat. Commun.* **2015**, *6*, 6293.
- (20) Amani, M.; Lien, D.-H.; Kiriya, D.; Xiao, J.; Azcatl, A.; Noh, J.; Madhupathy, S. R.; Addou, R.; KC, S.; Dubey, M.; Cho, K.; Wallace, R. M.; Lee, S.-C.; He, J.-H.; Ager, J. W.; Zhang, X.; Yablonovitch, E.; Javey, A. Near-Unity Photoluminescence Quantum Yield in MoS₂. *Science* **2015**, *350*, 1065–1068.
- (21) Yu, Z.; Pan, Y.; Shen, Y.; Wang, Z.; Ong, Z.-Y.; Xu, T.; Xin, R.; Pan, L.; Wang, B.; Sun, L.; Wang, J.; Zhang, G.; Zhang, Y. W.; Shi, Y.; Wang, X. Towards intrinsic charge transport in monolayer molybdenum disulfide by defect and interface engineering. *Nat. Commun.* **2014**, *5*, 5290.
- (22) Makarova, M.; Okawa, Y.; Aono, M. Selective Adsorption of Thiol Molecules at Sulfur Vacancies on MoS₂ (0001), Followed by Vacancy Repair via S-C Dissociation. *J. Phys. Chem. C* **2012**, *116*, 22411–22416.
- (23) Surrente, A.; Dumcenco, D.; Yang, Z.; Kuc, A.; Jing, Y.; Heine, T.; Kung, Y.-C.; Maude, D. K.; Kis, A.; Plochocka, P. Defect Healing and Charge Transfer-Mediated Valley Polarization in MoS₂/MoSe₂/MoS₂ Trilayer van der Waals Heterostructures. *Nano Lett.* **2017**, *17*, 4130–4136.
- (24) Noh, J.-Y.; Kim, H.; Kim, Y.-S. Stability and Electronic Structures of Native Defects in Single-Layer MoS₂. *Phys. Rev. B: Condens. Matter Mater. Phys.* **2014**, *89*, 205417.
- (25) Santosh, K.; Longo, R. C.; Addou, R.; Wallace, R. M.; Cho, K. Impact of Intrinsic Atomic Defects on the Electronic Structure of MoS₂ Monolayers. *Nanotechnology* **2014**, *25*, 375703.
- (26) Ghorbani-Asl, M.; Enyashin, A. N.; Kuc, A.; Seifert, G.; Heine, T. Defect-Induced Conductivity Anisotropy in MoS₂ Monolayers. *Phys. Rev. B: Condens. Matter Mater. Phys.* **2013**, *88*, 245440.
- (27) Sim, D. M.; Kim, M.; Yim, S.; Choi, M.-J.; Choi, J.; Yoo, S.; Jung, Y. S. Controlled Doping of Vacancy-Containing Few-Layer MoS₂ via Highly Stable Thiol-Based Molecular Chemisorption. *ACS Nano* **2015**, *9*, 12115–12123.
- (28) Peterson, S. L.; Schulz, K. H. Ethanethiol Decomposition Pathways on MoS₂ (0001). *Langmuir* **1996**, *12*, 941–945.
- (29) Wiegenstein, C. G.; Schulz, K. H. Methanethiol Adsorption on Defective MoS₂ (0001). *J. Phys. Chem. B* **1999**, *103*, 6913–6918.
- (30) Chen, X.; Berner, N. C.; Backes, C.; Duesberg, G. S.; McDonald, A. R. Functionalization of Two-Dimensional MoS₂: On the Reaction Between MoS₂ and Organic Thiols. *Angew. Chem., Int. Ed.* **2016**, *55*, 5803–5808.
- (31) Benziger, J. B.; Preston, R. E. Organosulfur Chemistry on Tungsten (211) Surfaces. I. A Comparison of Methanethiol and Methanol. *J. Phys. Chem.* **1985**, *89*, 5002–5010.
- (32) Kubas, G. J. Five-Co-Ordinate Molybdenum and Tungsten Complexes, [M(CO)₃(PCy₃)₂], which Reversibly Add Dinitrogen, Dihydrogen, and Other Small Molecules. *J. Chem. Soc., Chem. Commun.* **1980**, 61–62.
- (33) Gordon, J. C.; Kubas, G. J. Perspectives on How Nature Employs the Principles of Organometallic Chemistry in Dihydrogen Activation in Hydrogenases. *Organometallics* **2010**, *29*, 4682.
- (34) Skipper, C. V. J.; Hamaed, A.; Antonelli, D. M.; Kaltsoyannis, N. The Kubas Interaction in M(II) (M = Ti, V, Cr) Hydrazine-Based Hydrogen Storage Materials: A DFT Study. *Dalton Trans.* **2012**, *41*, 8515–8523.
- (35) Soler, J. M.; Artacho, E.; Gale, J. D.; García, A.; Junquera, J.; Ordejón, P.; Sánchez-Portal, D. The SIESTA Method for *Ab Initio* Order-N Materials Simulation. *J. Phys.: Condens. Matter* **2002**, *14*, 2745.
- (36) Perdew, J. P.; Burke, K.; Ernzerhof, M. Generalized Gradient Approximation Made Simple. *Phys. Rev. Lett.* **1996**, *77*, 3865.
- (37) Monkhorst, H. J.; Pack, J. D. Special Points for Brillouin-Zone Integrations. *Phys. Rev. B* **1976**, *13*, 5188.
- (38) Troullier, N.; Martins, J. L. Efficient Pseudopotentials for Plane-Wave Calculations. *Phys. Rev. B: Condens. Matter Mater. Phys.* **1991**, *43*, 1993–2006.

(39) <http://departments.icmab.es/leem/siesta/Databases/Pseudopotentials/periodictable-gga-abinit.html>, accessed on August 1, 2016.

(40) Hestenes, M. R.; Stiefel, E. Methods of Conjugate Gradients for Solving Linear Systems. *J. Res. Natl. Bur. Stand.* **1952**, *49*, 409–436.

(41) BAND2017, SCM, Theoretical Chemistry; Vrije Universiteit: Amsterdam, The Netherlands, <http://scm.com>, accessed on June 22, 2016.

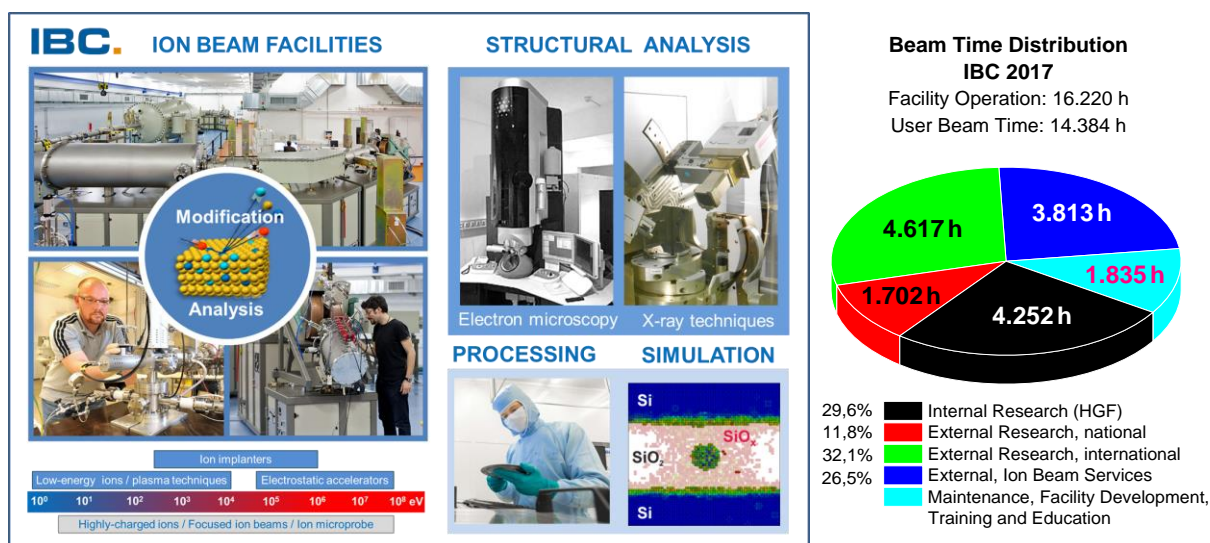
Statistics

Image: HZDR/H.Schultheiss, T. Hache

User facilities and services

Ion Beam Center (IBC)

The Ion Beam Center (IBC) at HZDR combines various machines (electrostatic accelerators, ion implanters, low-energy and plasma-based ions equipment) into a unique facility primarily used for ion beam modification and ion beam analysis of materials. The available energy range spans from a few eV to almost 100 MeV with a respective interaction depth in solids between 0.1 nm to 10 μm . In addition to standard broad beams also focused (down to 1 nm) and highly-charged (charge state up to +45) ion beams are available. For the benefit of the users in combination with an allocated ion experiment structural analysis (electron microscopy and spectroscopy, X-ray scattering techniques) and sample or device processing under clean-room conditions can be utilized at IBC to provide a “complete” user service. At the 6 MV tandem accelerator, the IBC together with the Helmholtz Institute Freiberg for Resource Technology (HIF, www.hzdr.de/HIF) operates the DREAMS (DREsden AMS = accelerator mass spectrometry) facility, which is used for the determination of long-lived radionuclides ($^7,^{10}\text{Be}$, ^{26}Al , ^{35}Cl , ^{41}Ca , ^{129}I and others) with ultimate sensitivity. A schematic overview of the IBC including the description of the main beam lines and experimental stations is given on page 55 of this Annual Report. In 2017, about 14.400 beam time hours were delivered for about 480 users from 23 countries worldwide performing experiments at IBC or using the capabilities for ion beam services.



IBC activities are efficiently integrated into various Helmholtz programs within the research field “Matter”, but also in the Helmholtz cross-program activities “Mineral Resources”, “Materials Research for Energy Technologies”, and “Helmholtz Energy Materials Foundry”. From 2013, the IBC has been recognized as a large-scale facility within the “BMBF Verbundforschung” promoting long-term collaborations with universities. In addition, from 2015 the IBC has the status of a Helmholtz LK-II user facility.

The IBC demonstrates its outstanding status within the international community of ion beam facilities by the following features:

- the IBC has provided ion beam technology as a user and competence centre for ion beam applications for more than 30 years. With respect to user beam time hours, the IBC is internationally leading and has been supported by numerous national and European grants and by industry.
- the IBC activities cover both ion beam modification as well as ion beam analysis (IBA). Experienced staff is present to support IBC users and to enhance the experimental capabilities to their needs.

- the operation of IBC is accompanied by a strong in-house research at the affiliated host “Institute of Ion Beam Physics and Materials Research”, both in experiment and theory. This allows in-depth research in targeted research areas as well as the exploration of new application fields for ion beam technology.

Following the rules of a European and national user facility, access for scientific experiments to IBC is provided on the basis of a proposal procedure (www.hzdr.de/IBC) via the common HZDR user facility portal **HZDR-GATE** (gate.hzdr.de). Due to the availability of multiple machines and versatile instrumentation, IBC proposals can be submitted continuously (no deadline). The scientific quality of the proposals is steadily evaluated and ranked by an external international User Selection Panel. For successfully evaluated proposals, users get free access to IBC facilities for their experiments which can be often realized within four months after proposal submission. Moreover, the IBC provides possibilities for fast access via pilot and test experiments which are limited to 16 hours beam time. The use of the IBC facilities includes the scientific and technical support during planning, execution and evaluation of the experiments. For AMS samples preparation, two chemical laboratories are available.

The IBC strongly supports the commercial exploitation of ion beam technology by partners from industry which is essential for materials science applications. For ion beam services, the HZDR Innovation GmbH (spin-off of the HZDR) – www.hzdr-innovation.de – provides a direct and fast access to the IBC facilities based on individual contracts. The close collaboration between IBC and HZDR Innovation GmbH is considered as a Helmholtz reference model aiming to develop innovative strategies for an effective contribution of large-scale facilities for economic innovation. Currently, about 25% of the total IBC beam time is provided for commercial ion beam services.

The IBC pursues two strategic objectives for further development. On one hand, it is focused on the successful operation as an international user facility to sustain its position as a leading European ion beam center in the fields of materials and interdisciplinary research. This requires the continuous development and extension of ion beam technologies. Special emphasis is directed towards new R&D areas and communities which so far have not been aware of the advantages of ion technology. On the other hand, cutting edge scientific challenges, in particular for the modification and understanding of the function of materials at the nanoscale down to the atomic level, are addressed in order to achieve new functionalities and to design novel materials. These challenges comprise:

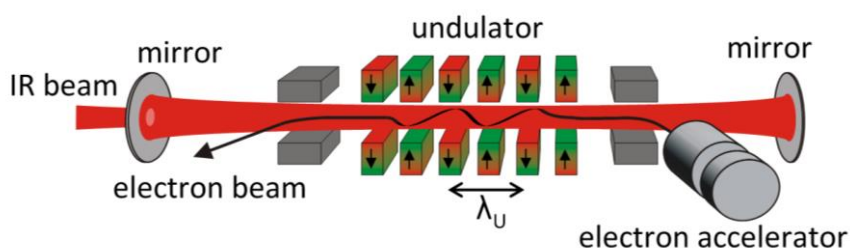
- the extended application of low-energy ions for modification and analysis of ultra-thin films, surfaces, 2D materials and molecular layers based on a new low-energy ion nano-engineering technology platform which has recently started with the installation of first tools,
- the investigation of material states and modifications far from equilibrium induced by high energy density excitations with cluster ions and highly-charged ions,
- the exploration of new IBA approaches with unprecedented lateral resolution, ultimate detection limit and high sample throughput, e.g. for resource technology. With projects like “PIXE-Camera” and “Super-SIMS”, both in close collaboration with the HIF, the interdisciplinary work of IBC will be substantially extended towards the application of ion beam analysis methods in geosciences and resource technology.

Recently, some new ion beam tools and end-stations have been commissioned which will attract new users by cutting-edge experimental instrumentation. The basically upgraded ion microprobe station at the 3 MV machine is now in routine and user friendly operation mode, delivering the possibility to use – in parallel or sequential – several IBA techniques with a spatial resolution of about 3 μm . An ion microscope *ORION NanoFab* (He/Ne ions, 10 – 40 keV) provides unique possibilities for surface imaging, nano-fabrication and, for the first time, elemental analysis based on ion beam analysis techniques. The cluster tool at the 6 MV accelerator allows *in situ* deposition and analysis investigations at temperatures of up to 800°C. Recently, first instruments for the new low-energy ions nano-engineering laboratory have been commissioned, including the installation of a 100 keV accelerator, a MEIS setup and a new low-energy electron microscope (LEEM) aiming to study low-energy ion interactions at surfaces.

For more detailed information, please contact Dr. Johannes von Borany (j.v.borany@hzdr.de) or Dr. Stefan Facsko (s.facsko@hzdr.de) and visit the IBC webpage: www.hzdr.de/IBC.

Free Electron Laser FELBE

FELBE is an acronym for the free-electron laser (FEL) at the Electron Linear accelerator with high Brilliance and low Emittance (ELBE) located at the Helmholtz-Zentrum Dresden-Rossendorf. The heart of ELBE is a superconducting linear accelerator operating in continuous-wave (cw) mode with a pulse repetition rate of 13 MHz. The electron beam (40 MeV, 1 mA max.) is guided to several laboratories where secondary beams (particle and electromagnetic) are generated. Two free-electron lasers (U37-FEL and U100-FEL) produce intense, coherent electromagnetic radiation in the mid and far infrared, which is tunable over a wide wavelength range (5 – 250 μm) by changing the electron energy or the undulator magnetic field. The previous U27 undulator has been replaced by the U37, in order to provide better coverage of the 20 – 35 μm region. Main parameters of the infrared radiation produced by FELBE are as follows:



Wavelength λ	5 – 40 μm 18 – 250 μm	FEL with undulator U37 FEL with undulator U100
Pulse energy	0.01 – 2 μJ	depends on wavelength
Pulse length	1 – 25 ps	depends on wavelength
Repetition rate	13 MHz	3 modes: <ul style="list-style-type: none"> • cw • macropulsed (> 100 μs, < 25 Hz) • single pulsed (Hz ... kHz)

The free electron laser is a user facility. Applications for beam time can be submitted twice a year, typically by April 15 and October 15. Users from EU countries are able to receive support through the HORIZON 2020 Integrated Infrastructure Initiative (I3) CALIPSOplus (Convenient Access to Light Sources Open to Innovation, Science and to the World) which started in May 2017.

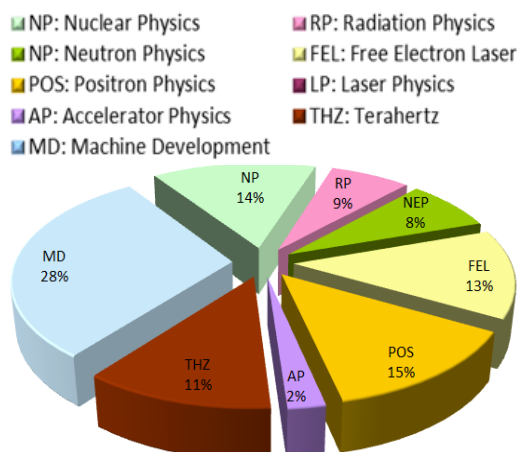
Typical applications are picosecond pump-probe spectroscopy (also in combination with several other femtosecond lasers, which are synchronized to the FEL), near-field microscopy, and nonlinear optics. The FELBE facility also serves as a far-infrared source for experiments at the Dresden High Magnetic Field Laboratory (HLD) involving pulsed magnetic fields up to 70 T.

The statistics shows that the FEL used 762 hours beam time of the ELBE accelerator. This corresponds to 13 % of total beam time, which is again distributed among internal and external users.

For further information, please contact Prof. Manfred Helm (m.helm@hzdr.de) or visit the FELBE webpage www.hzdr.de/FELBE.



Beamtime Distribution at ELBE



Experimental equipment

Accelerators, ion implanters and other ion processing tools

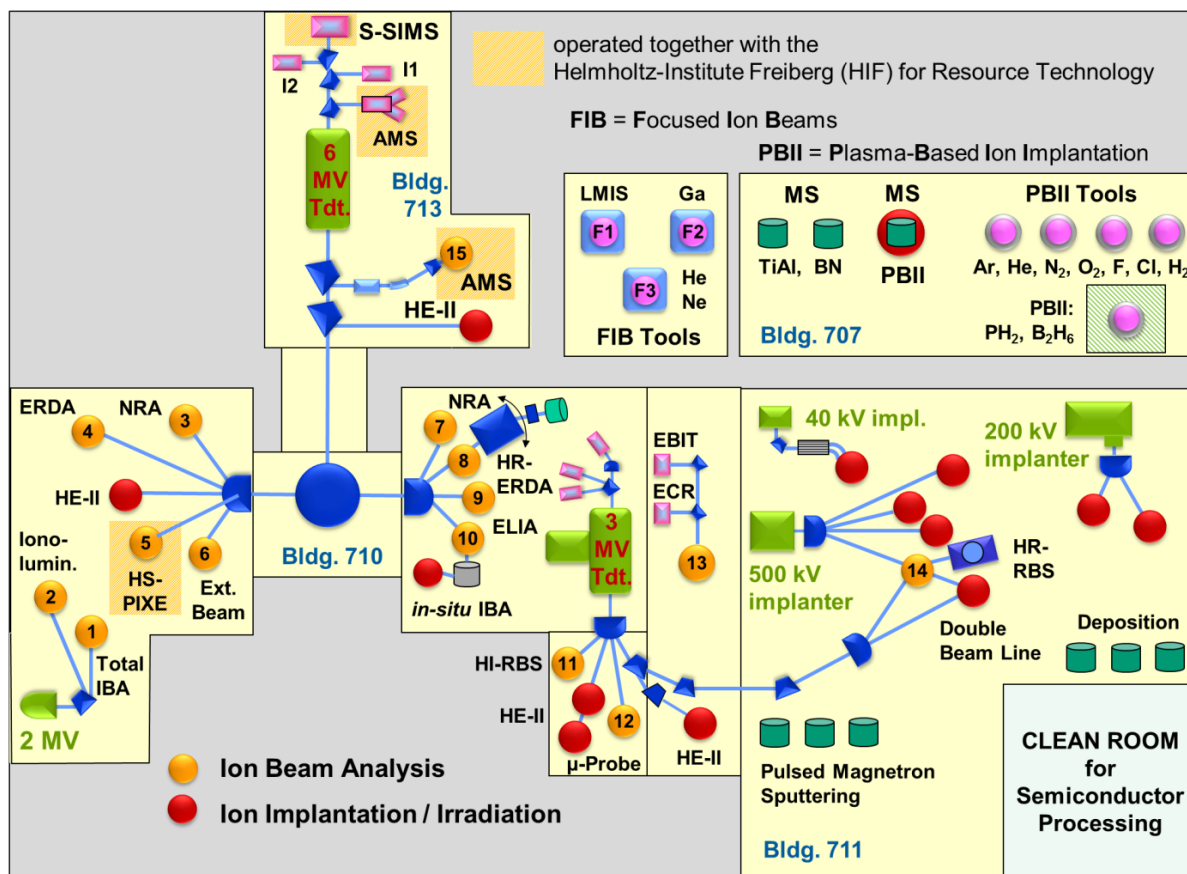
Van de Graaff Accelerator (VdG)	2 MV	<i>TuR Dresden, DE</i>
Tandetron Accelerator (T1)	3 MV	<i>HVEE, NL</i>
Tandetron Accelerator (T2)	6 MV	<i>HVEE, NL</i>
Low-Energy Ion Implanter	0.1 – 40 kV	<i>Danfysik, DK</i>
High-Current Ion Implanter	20 – 200 kV	<i>Danfysik, DK</i>
High-Energy Ion Implanter	20 – 500 kV	<i>HVEE, NL</i>
Plasma Immersion Ion Implantation	5 – 30 kV	<i>UK, DE; Home-built</i>
Mass-Separated Focused Ion Beam (FIB) (15 nm, variable ions)	10 – 30 keV >10 A/cm ²	<i>Orsay Physics, FR</i>
ORION NanoFab FIB Tool (including GIS and Nanopatterning)	He, Ne ions, 10 – 35 kV, Resolution < 2 nm	<i>Carl Zeiss Microscopy, DE</i>
Highly-Charged Ion Facility	25 eV – 25 keV × Q Q = 1 ... 40 (Xe)	<i>Home-built</i>
Ion-Beam Sputtering	200 – 2000 V	<i>Home-built</i>
UHV Ion Irradiation (Ar, He, etc.)	0 – 5 kV Scan 10 × 10 mm ²	<i>Cremer, DE; VG, USA</i>

Ion beam analysis (IBA)

A wide variety of advanced IBA techniques are available at the MV accelerators (see figure).

RBS	Rutherford Backscattering Spectrometry	(1), (10), (11), (12)	<i>VdG, T1, T2, HIM</i>
RBS/C	RBS + Channelling	(1), (2), (11), (12)	<i>VdG, T1, T2</i>
HR-RBS	High-Resolution RBS	(10), (14)	<i>T1</i>
ERDA	Elastic Recoil Detection Analysis	(1), (4)	<i>VdG, T2</i>
PIXE	Particle-Induced X-ray Emission	(1), (2), (5), (6), (12)	<i>VdG, T1, T2</i>
PIGE	Particle-Induced γ Emission	(6), (12)	<i>T1, T2</i>
NRA	Nuclear Reaction Analysis	(3), (7), (11), (12)	<i>T1, T2</i>
NRRA	Nuclear Resonance Reaction Analysis	(3), (7), (11)	<i>T1, T2</i>
NMP	Nuclear Microprobe	(12)	<i>T1</i>
AMS	Accelerator Mass Spectrometry (focused to long-lived radionuclides: ⁷ Be, ¹⁰ Be, ²⁶ Al, ³⁶ Cl, ⁴¹ Ca, ¹²⁹ I)	(15)	<i>T2</i>

Some stations are equipped with additional process facilities enabling *in-situ* IBA investigations during ion irradiation, sputtering, deposition, annealing, investigations at solid-liquid interfaces, etc.



Schematic overview of the HZDR Ion Beam Center

Other particle-based analytical techniques

SEM	Scanning Electron Microscope (S4800 II)	1 – 30 keV + EDX	Hitachi, JP
TEM	Transmission Electron Microscope (Titan 80-300 with Image Corrector)	80 – 300 keV + EDX, EELS	FEI, NL
TEM	Transmission Electron Microscope (Talos F200X)	20 – 200 keV + SuperX EDX	FEI, NL
HIM	Scanning Ion Microscope (ORION NanoFab with He, Ne ions)	He, Ne ions 10 – 35 kV + RBS, SIMS	Carl Zeiss Microscopy, DE
FIB/SEM	Focused Ion/Electron Cross Beam (NVision 40 with Elphy Plus Litho)	0.5 – 30 keV + EDX, EBSD	Carl Zeiss Microscopy, DE
AES	Auger Electron Spectroscopy	+ XPS	Thermo Fisher Scientific, UK
LEEM	Low-Energy Electron Microscope (Spec-LEEM-III)	0 eV – 4.5 keV Resolution < 6 nm + AES	Elmitec, DE
CEMS	Mössbauer Spectroscopy	⁵⁷ Fe source	Home-built

Photon-based analytical techniques

XRD/XRR	X-Ray Diffractometers	Cu-K α	
	θ - θ Powder D8		<i>Bruker, DE</i>
	θ -2 θ 4-Circle D5005		<i>Siemens, DE</i>
	θ - θ 4-Circle Empyrean		<i>PANalytical, NL</i>
	θ -2 θ 4+2-Circle SEIFERT XRD3003-HR		<i>General Electric, US</i>
SE	Spectroscopic Ellipsometry	250 – 1700 nm	<i>Woollam, US</i>
UV-Vis	Solid Spec 3700 DUV	190 – 3300 nm	<i>Shimadzu, JP</i>
FTIR	Fourier-Transform Infrared Spectrometer	600 – 7000 cm ⁻¹	<i>Nicolet, US</i>
FTIR	Fourier-Transform Infrared Spectrometer	50 – 15000 cm ⁻¹	<i>Bruker, DE</i>
	Ti:Sapphire Femtosecond Laser	78 MHz	<i>Spectra Physics, US</i>
	Femtosecond Optical Parametric Osci.		<i>APE, DE</i>
	Ti:Sapphire Femtosecond Amplifier	1 kHz, 250 kHz	<i>Coherent, US</i>
	Femtosecond Optical Parametric Amplifier		<i>Light Conversion, LT</i>
THz-TDS	Terahertz Time-Domain Spectroscopy	0.1 – 4 THz	<i>Home-built</i>
Raman	Raman Spectroscopy	> 45 cm ⁻¹	<i>Jobin-Yvon-Horiba, FR</i>
	In-situ Raman Spectroscopy	> 100 cm ⁻¹	<i>Jobin-Yvon-Horiba, FR</i>
PL	Photoluminescence (10 – 300 K)	300 – 1600 nm	<i>Jobin-Yvon-Horiba, FR</i>
TRPL	Time-Resolved Photoluminescence	$\tau = 3$ ps – 2 ns $\tau > 5$ ns	<i>Hamamatsu Phot., JP</i> <i>Stanford Research, US</i>
EL	Electroluminescence	300 – 1600 nm	<i>Jobin-Yvon-Horiba, FR</i>
	Optical Split-Coil Supercond. Magnet	7 T	<i>Oxford Instr., UK</i>
PR	Photomodulated Reflectivity	300 – 1600 nm	<i>Jobin-Yvon-Horiba, FR</i>
PLE	Photoluminescence Excitation	300 – 1600 nm	<i>Jobin-Yvon-Horiba, FR</i>
OES	Optical Emission Spectroscopy	250 – 800 nm	<i>Jobin-Yvon-Horiba, FR</i>

Magnetic thin film deposition and analysis

PLD	Pulsed Laser Deposition		<i>SURFACE, DE</i>
MFM	Magnetic Force Microscope	~ 50 nm resol.	<i>VEECO; DI, US</i>
SQUID MPSM	Supercond. Quantum Interference Device	± 7 T	<i>Quantum Design, US</i>
SQUID VSM	Vibrating Sample Magnetometer	± 7 T	<i>Quantum Design, US</i>
MOKE	Magneto-Optic Kerr Effect (in-plane)	± 0.35 T	<i>Home-built</i>
MOKE	Magneto-Optic Kerr Effect (perpend.)	± 2 T	<i>Home-built</i>
FR-MOKE	Frequency-Resolved Magneto-Optic KE	± 1.1 T	<i>Home-built</i>
SKM	Scanning Kerr Microscope		<i>Home-built</i>
	Kerr Microscope		<i>Evico Magnetics, DE</i>
TR-MOKE	Time-Resolved MOKE (Pump-Probe)		<i>Home-built</i>
VNA-FMR	Vector Network Analyzer Ferromagnetic Resonance	50 GHz	<i>Agilent, DE;</i> <i>Home-built</i>
Cryo-FMR	Variable-Temperature Ferromagnetic Resonance	3 – 300 K	<i>Attocube, DE;</i> <i>Home-built</i>

ME	Magnetoellipsometer		<i>LOT, DE; AMAC, US</i>
μ BLS	Brillouin Light Scattering Microscope	± 0.8 T, 532 nm & 491 nm	<i>Home-built</i>
SKM	Scanning Kerr Microscope with RF Detection (Spectrum Analyzer)	± 0.5 T, 40 GHz	<i>Home-built</i>
MT-50G	High Frequency Magneto-Transport Setup	± 1.5 T, 50 GHz 250 ps	<i>Home-built</i>

Other analytical and measuring techniques

STM/AFM	UHV Scanning Probe Microscope (variable T)		<i>Omicron, DE</i>
AFM	Atomic Force Microscope (Contact, Tapping, Spreading)		<i>Bruker, US</i>
AFM	Atomic Force Microscope (with c-AFM, SCM-Module)		<i>Bruker, US</i>
	Dektak Surface Profilometer		<i>Bruker, US</i>
	Micro Indenter/Scratch Tester		<i>Shimatsu, JP</i>
MPMS	Mechanical Properties Measurement System – Stretcher		<i>Home-built</i>
MS	Mass Spectrometers (EQP-300, HPR-30)		<i>HIDEN, DE/US</i>
	Wear Tester (pin-on disc)		<i>Home-built</i>
LP	Automated Langmuir Probe		<i>Impedans, IE</i>
HMS	Hall Measurement System	2 – 400 K, ≤ 9 T	<i>LakeShore, US</i>
	Van-der-Pauw HMS Ecopia	300 K & LNT, 0.5 T	<i>Bridge Technol., US</i>
MTD	Magneto-Transport Device	300 K, ≤ 3 T	<i>Home-built</i>
RS	Sheet-Rho-Scanner		<i>AIT, KOR</i>
RMAG	Redmag Tensormeter System	240 – 350 K, 1.5 T	<i>Home-built</i>
GMAG	Greymag Tensormeter System	300 K, 0.7 T	<i>Home-built</i>
DLTS	Deep Level Transient Spectroscopy	+ I-U/C-V 10 – 300 K, 1 MHz	<i>PhysTech, DE</i>
IV / CV	Photocapacitance (+I-V/G-V)	250 – 2500 nm	<i>Home-built</i>
IV / CV	I-V and C-V Analyzer		<i>Keithley, US</i>
IV / CV	I-V and C-V Semi-Automatic Prober	-60 – 300 °C	<i>Süss, DE; Keithley, US</i>
IV	I-V Prober	4.2 – 600 K	<i>LakeShore, Agilent, US</i>
GC	Gas Chromatography (GC-2010)		<i>Shimadzu, JP</i>
ECW	Electrochemical workstation (CHI 760e)		<i>CH instruments, US</i>
FDA	Force-displacement analysis machine		<i>Sauter, DE</i>
IV / VNA	I-V and VNA Prober for VHF, LCR and frequency analysis measurements	20-120 MHz	<i>Süss, DE; Cascade, US; Keysight, US</i>
OSCI	4-channel real time oscilloscope	1,5 GHz (BW), 5 GSa/s	<i>Keysight, US</i>
IR-Cam	TrueIR Thermal Imager	-20 – 350 °C	<i>Keysight, US</i>
CM	Confocal Microscope (Smartproof 5)	405 nm LED, z drive res. ~ 1 nm	<i>Carl Zeiss, DE</i>
FAS	Fluidic Analytic Setup – microscope, high speed camera, and fluidic pumps	2 GB 120 kfps, 5 modules	<i>Zeiss, DE; Photron, US; Cetoni, DE</i>

Deposition and processing techniques

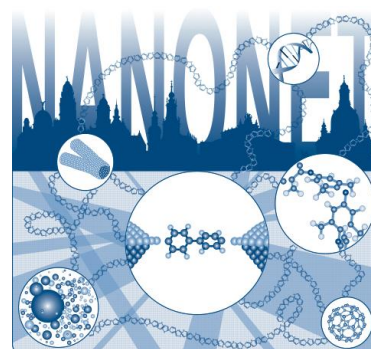
Physical Deposition	Sputtering DC/RF, Evaporation	<i>Nordiko, UK</i>
	Electron Beam Evaporation System	<i>Leybold Optics, DE</i>
	Thermal Evaporation	<i>Bal-Tec, LI</i>
	DC/RF magnetron sputter system, 6x 4" magnetrons, substrate heating: RT – 950 °C, up to 4" wafers	<i>BESTEC, DE</i>
	High Power Impulse Magnetron Sputtering	<i>Melec, DE</i>
Molecular Beam Epitaxy	III-V Semiconductors	<i>Riber, FR</i>
Chemical Vapour Deposition	Plasma Enhanced CVD: a-Si, a-Ge, SiO ₂ , SiON, Si ₃ N ₄	<i>Oxford Instr., UK</i>
Atomic Layer Deposition	Al ₂ O ₃ , HfO ₂ , SiO ₂	<i>Ultratech, US</i>
Dry Etching	ICP-RIE: CF ₄ , SF ₆ , C ₄ F ₈	<i>Sentech, DE</i>
	RIBE, Ø 6": Ar, CF ₄	<i>Roth & Rau, DE</i>
	Barrel reactor, Ø 4": O ₂ , SF ₆	<i>Diener electronic, DE</i>
Etching/Cleaning	incl. Anisotropic Selective KOH Etching	
Photolithography	Mask-Aligner MJB3, 2 µm accur.; Ø 3"	<i>Süss, DE</i>
	Direct Laser Writer DWL 66FS, 2 µm accuracy, Ø 8"x8"	<i>Heidelberg Instr., DE</i>
	Laser Micro Writer ML, 10 µm accuracy	<i>Durham Magneto Optics, UK</i>
Electron Beam Lithography	Raith 150-TWO: Ø 6", 10 nm resol.	<i>Raith, DE</i>
	e-Line Plus: Ø 4", 10 nm resol.	<i>Raith, DE</i>
Thermal Treatment	Room Temperature – 2000 °C	
	Furnace	<i>InnoTherm, DE</i>
	Rapid Thermal Annealing JETFIRST 100	<i>JIPELEC, FR</i>
	Rapid Thermal Annealing AW 610	<i>Allwin21, USA</i>
	Flash-Lamp Units (0.5 – 20 ms)	<i>Home-built;FHR/DTF, DE</i>
	RF Heating (Vacuum)	<i>JIPELEC, FR</i>
	Laser Annealing (CW, 808 nm, 450 W)	<i>LIMO, DE;</i>
	Laser Annealing (30 ns pulse, 10 Hz, 308 nm, 500 mJ)	<i>COHERENT, USA</i>
	CVD Tube furnace (RT– 1200 °C, three channel gas)	<i>NBD, CN</i>
	Vacuum oven (RI – 250 °C, Vacuum < 133 Pa)	<i>LAB-KITS, CN</i>
Bonding Techniques	Ultrasonic Wire Bonding	<i>Kulicke & Soffa, US</i>
	Semi-automatic Wire-bonder: Gold-ball and wedge-wedge bonding	<i>F & S Bondtec, AT</i>
	Ultrasonic generator: 60 kHz, 140 kHz	
	Wire deformation control software	
Cutting, Grinding, Polishing		<i>Bühler, DE</i>
TEM Sample Preparation	Plan View and Cross Section incl. Ion Milling Equipment	<i>Gatan, US</i>
Disperse and mixer	Mixer for pastes and emulsions	<i>IKA, DE</i>
Centrifuge	Max. 17850 rpm, -10 ... +40 °C	<i>Thermo Scientific, US</i>

Doctoral training programme

International Helmholtz Research School NANONET

The Institute of Ion Beam Physics and Materials Research is coordinating the International Helmholtz Research School for Nanoelectronic Networks (IHRS NANONET) supported by the Initiative and Networking Fund of the Helmholtz Association. The project started in October 2012. The total funding is 1.2 Mio. € for a period of six years.

The IHRS NANONET is an international, interdisciplinary and thematically focused doctoral programme in the field of molecular electronics. The research school aims at attracting and promoting excellence by educating promising doctoral candidates with backgrounds in physics, chemistry, materials science and electrical engineering. During a period of three years, PhD candidates benefit from well-structured, comprehensive training curricula and multiple mentorship, while performing cutting edge research projects within one of the 15 NANONET research groups. Under the supervision of outstanding scientists leading the field of nanoelectronics, the doctoral candidates have the unique opportunity to contribute to the advancement of molecular electronics by developing strategies for the integration of single nano-sized building blocks into large interconnected networks.



The IHRS NANONET fosters not only professional qualification but also personal development by equipping young graduates with competencies for successful careers in a wide variety of positions in academia and industry. The NANONET Annual Workshop 2017 was conducted in the vicinity of Dresden and was attended by 32 participants from 9 countries. Two senior students concluded their PhD degrees in 2017 at the TU Dresden: Congratulations to Dr. Gözde Öktem and Dr. Jonas Nawroth.

The consortium

- Helmholtz-Zentrum Dresden-Rossendorf (HZDR)
- Technische Universität (TU) Dresden
- Leibniz Institute of Polymer Research (IPF) Dresden
- Fraunhofer Institute for Ceramic Technologies and Systems (IKTS) Dresden
- Nanoelectronic Materials Laboratory (NaMLab) gGmbH Dresden



For further information, please contact the NANONET coordinator, Dr. Peter Zahn (nanonet@hzdr.de), or visit the IHRS NANONET website: www.hzdr.de/nanonet.

Publications

Books and chapters

1. Möller, W.
Fundamentals of Ion-Solid Interaction - A Compact Introduction
Wissenschaftlich-Technische Berichte / Helmholtz-Zentrum Dresden-Rossendorf; HZDR-073 (2017)
2. Schultheiss, K.; Wagner, K.; Kákay, A.; Schultheiss, H.
Steering magnons by non-collinear spin textures
Sergej Demokritov: Spin Wave Confinement: Propagating Waves (2nd Edition), Singapore: Pan Stanford Publishing Pte. Ltd. (2017) ISBN 9789814774352

Publications in journals

Magnetism

1. Arora, M.; Hübner, R.; Suess, D.; Heinrich, B.; Girt, E.
Origin of perpendicular magnetic anisotropy in Co/Ni multilayers
Physical Review B **96**, 024401 (2017)
2. Arora, M.; Lee-Hone, N. R.; Mckinnon, T.; Coutts, C.; Hübner, R.; Heinrich, B.; Broun, D. M.; Girt, E.
Magnetic properties of Co/Ni multilayer structures for use in STT-RAM
Journal of Physics D: Applied Physics **50**, 505003 (2017)
3. Ball, D. K.; Günther, S.; Fritzsche, M.; Lenz, K.; Varvaro, G.; Laureti, S.; Makarov, D.; Mücklich, A.; Facsko, S.; Albrecht, M.; Fassbender, J.
Out-of-plane magnetized cone-shaped magnetic nanoshells
Journal of Physics D: Applied Physics **50**, 115004 (2017)
4. Banerjee, C.; Gruszecki, P.; Klos, J. W.; Hellwig, O.; Krawczyk, M.; Barman, A.
Magnonic band structure in a Co/Pd stripe domain system investigated by Brillouin light scattering and micromagnetic simulations
Physical Review B **96**, 024421 (2017)
5. Chumak, A. V.; Schultheiss, H.
Magnonics: Spin waves connecting charges, spins and photons
Journal of Physics D: Applied Physics **50**, 300201 (2017)
6. Dev, B. N.; Banu, N.; Fassbender, J.; Grenzer, J.; Schell, N.; Bischoff, L.; Grötzschel, R.; McCord, J.
Ion irradiation effects on a magnetic Si/Ni/Si trilayer and lateral magnetic-nonmagnetic multistrip patterning by focused ion beam
Indian Journal of Physics **91**, 1167 (2017)
7. Drovosekova, A. B.; Kreines, N. M.; Savitsky, A. O.; Kapelnitsky, S. V.; Rylkov, V. V.; Tugushev, V. V.; Prutskov, G. V.; Novodvorskii, O. A.; Shorokhova, A. V.; Wang, Y.; Zhou, S.
Magnetic anisotropy of polycrystalline high-temperature ferromagnetic Mn_xSi_{1-x} ($x \approx 0.5$) alloy films
Journal of Magnetism and Magnetic Materials **429**, 305 (2017)
8. Erb, D.; Schlage, K.; Bocklage, L.; Hübner, R.; Merkel, D. G.; Ruffer, R.; Wille, H.-C.; Röhlberger, R.
Disentangling magnetic order on nanostructured surfaces
Physical Review Materials **1**, 023001(R) (2017)
9. Finizio, S.; Wintz, S.; Kirk, E.; Suszka, A.; Gliga, S.; Wohlhüter, P.; Zeissler, K.; Raabe, J.
Control of the gyration of magnetic vortices by the magneto-elastic effect
Physical Review B **96**, 054438 (2017)

10. Heidarian, A.; Stienen, S.; Semisalova, A.; Hübner, R.; Salamon, S.; Wende, H.; Gallardo, R.; Grenzer, J.; Potzger, K.; Lindner, J.; Bali, R.
Ferromagnetic resonance of MBE-grown FeRh thin films through the metamagnetic phase transition
Physica Status Solidi (B) **254**, 1700145 (2017)
11. Körber, L.; Wagner, K.; Kákay, A.; Schultheiß, H.
Spin-wave reciprocity in the presence of Néel walls
IEEE Magnetics Letters **8**, 4109804 (2017)
12. Kosub, T.; Kopte, M.; Hühne, R.; Appel, P.; Shields, B.; Maletinsky, P.; Hübner, R.; Liedke, M. O.; Fassbender, J.; Schmidt, O. G.; Makarov, D.
Purely Antiferromagnetic Magnetoelectric Random Access Memory
Nature Communications **8**, 13985 (2017)
13. Kriegner, D.; Reichlova, H.; Grenzer, J.; Schmidt, W.; Ressouche, E.; Godinho, J.; Wagner, T.; Martin, S.; Shick, A.; Volobuev, V.; Springholz, G.; Holy, V.; Wunderlich, J.; Jungwirth, T.; Vyborny, K.
Magnetic anisotropy in antiferromagnetic hexagonal MnTe
Physical Review B **96**, 214418 (2017)
14. Langer, M.; Röder, F.; Gallardo, R. A.; Schneider, T.; Stienen, S.; Gatel, C.; Hübner, R.; Bischoff, L.; Lenz, K.; Lindner, J.; Landeros, P.; Fassbender, J.
The role of the internal demagnetizing field for the dynamics of a magnonic crystal
Physical Review B **95**, 184405 (2017)
15. Lee-Hone, N. R.; Thanhoffer, R.; Neu, V.; Schäfer, R.; Arora, M.; Hübner, R.; Suess, D.; Broun, J. M.; Girt, E.
Roughness-induced domain structure in perpendicular Co/Ni multilayers
Journal of Magnetism and Magnetic Materials **441**, 283 (2017)
16. Lin, G.; Makarov, D.; Schmidt, O. G.
Magnetic sensing platform technologies for biomedical applications
Lab on a Chip **17**, 1884 (2017)
17. Liu, Y.; Yuan, Y.; Liu, F.; Böttger, R.; Anwand, W.; Wang, Y.; Semisalova, A.; Ponomaryov, A.; Lu, X.; N'Diaye, A. T.; Arenholz, E.; Heera, V.; Skorupa, W.; Helm, M.; Zhou, S.
Interaction between magnetic moments and itinerant carriers in d0 ferromagnetic SiC
Physical Review B **95**, 195309 (2017)
18. Liu, Yu; Li, Z.; Guo, L.; Chen, X.; Yuan, Y.; Xu, C.; Hübner, R.; Akhmedaliev, S.; Krasheninnikov, A. V.; N'Diaye, A. T.; Arenholz, E.; Helm, M.; Zhou, S.
Towards diluted magnetism in TaAs
Physical Review Materials **1**, 044203 (2017)
19. Otálora, J. A.; Yan, M.; Schultheiss, H.; Hertel, R.; Kákay, A.
Asymmetric spin-wave dispersion in ferromagnetic nanotubes induced by surface curvature
Physical Review B **95**, 184415 (2017)
20. Pfau, B.; Günther, C. M.; Hauet, T.; Eisebitt, S.; Hellwig, O.
Thermally induced magnetic switching in bit-patterned media
Journal of Applied Physics **122**, 043907 (2017)
21. Safranski, C.; Barsukov, I.; Lee, H. K.; Schneider, T.; Jara, A. A.; Smith, A.; Chang, H.; Lenz, K.; Lindner, J.; Tserkovnyak, Y.; Wu, M.; Krivorotov, I. N.
Spin caloritronic nano-oscillator
Nature Communications **8**, 117 (2017)
22. Sander, D.; Valenzuela, S. O.; Makarov, D.; Marrows, C. H.; Fullerton, E. E.; Fischer, P.; McCord, J.; Vavassori, P.; Mangin, S.; Pirro, P.; Hillebrands, B.; Kent, A. D.; Jungwirth, T.; Gutfleisch, O.; Kim, C. G.; Berger, A.
The 2017 Magnetism Roadmap
Journal of Physics D: Applied Physics **50**, 363001 (2017)

23. Schneider, T.; Langer, M.; Alekhina, J.; Kowalska, E.; Oelschlägel, A.; Semisalova, A.; Neudert, A.; Lenz, K.; Potzger, K.; Kostylev, M. P.; Fassbender, J.; Adeyeye, A. O.; Lindner, J.; Bali, R. **Programmability of Co-antidot lattices of optimized geometry** Scientific Reports **7**, 41157 (2017)
24. Ünal, A. A.; Parabas, A.; Arora, A.; Ehrler, J.; Barton, C.; Valencia, S.; Bali, R.; Thomson, T.; Yildiz, F.; Kronast, F. **Laser-driven formation of transient local ferromagnetism in FeRh thin films** Ultramicroscopy **108**, 104 (2017)
25. Wang, C.; Xu, C.; Wang, M.; Yuan, Y.; Liu, H.; Dillemans, L.; Homm, P.; Menghini, M.; Locquet, J.-P.; Haesendonck, C. V.; Zhou, S.; Ruan, S.; Zeng, Y.-J. **Coupling of ferromagnetism and structural phase transition in V₂O₃/Co bilayers** Journal of Physics D: Applied Physics **50**, 495002 (2017)
26. Wawro, A.; Kurant, Z.; Tekielak, M.; Jakubowski, M.; Pietruczik, A.; Böttger, R.; Maziewski, A. **Modifications of the magnetization ordering in Co/Mo/Co layers by Ga⁺ ion irradiation** Applied Physics Letters **110**, 252405 (2017)
27. Yildirim, O.; Tozkoparan, O.; Yuzuak, E.; Elerman, Y.; Dincer, I. **Magnetocaloric Effect with Very Small Magnetic Hysteresis Losses of CoMn_{1-x}Ti_xGe Alloys** Metallurgical and Materials Transactions A **48**, 5733 (2017)
28. Younas, M.; Xu, C.; Arshad, M.; Ho, L.; Zhou, S.; Azad, F.; Akhtar, M.; Su, S.; Azeem, W.; Ling, F. **Reversible Tuning of Ferromagnetism and Resistive Switching in ZnO/Cu Thin Films** ACS Omega **2**, 8810 (2017)
29. Yuan, Y.; Xu, C.; Hübner, R.; Jakiela, R.; Böttger, R.; Helm, M.; Sawicki, M.; Dietl, T.; Zhou, S. **Interplay between localization and magnetism in (Ga,Mn)As and (In,Mn)As** Physical Review Materials **1**, 054401 (2017)
30. Zhang, G.; Samuely, T.; Xu, Z.; Jochum, J. K.; Volodin, A.; Zhou, S.; May, P. W.; Onufriienko, O.; Kačmarčík, J.; Steele, J. A.; Li, J.; Vanacken, J.; Vacík, J.; Szabó, P.; Yuan, H.; Roeffaers, M. B. J.; Cerbu, D.; Samuely, P.; Hofkens, J.; Moshchalkov, V. V. **Superconducting Ferromagnetic Nanodiamond** ACS Nano **11**, 5358 (2017)
31. Zhang, Z. T.; Dmytriieva, D.; Molatta, S.; Wosnitza, J.; Wang, Y.; Helm, M.; Zhou, S.; Kühne, H. **Defect-induced magnetism in SiC probed by nuclear magnetic resonance** Physical Review B **95**, 085203 (2017)
32. Zhang, Z. T.; Xu, C.; Dmytriieva, D.; Molatta, S.; Wosnitza, J.; Wang, Y. T.; Helm, M.; Zhou, S.; Kühne, H. **Monovacancy paramagnetism in neutron-irradiated graphite probed by ¹³C NMR** Journal of Physics: Condensed Matter **29**, 465801 (2017)
33. Zhu, J. J.; Li, L.; Chen, L.; Prucnal, S.; Grenzer, J.; Zhao, J. H.; Helm, M.; Zhou, S. Q. **Annealing effect on ferromagnetic properties, hole concentration and electronic band structure of GaMnAs epitaxial layers** Journal of Materials Science **28**, 17622 (2017)

Nanoscience and materials for information technologies

34. Abbe, E.; Schüler, T.; Klosz, S.; Starruß, E.; Pilz, W.; Böttger, R.; Kluge, O.; Schmiel, T.; Tajmar, M. **Electrical behaviour of carbon nanotubes under low-energy proton irradiation** Journal of Nuclear Materials **295**, 299 (2017)
35. Acquah, S.F.A.; Penkova, A.V.; Markelov, D.A.; Semisalova, A. S.; Leonhardt, B. E.; Magi, J. M. **The Beautiful Molecule: 30 Years of C₆₀ and its Derivatives** ECS Journal of Solid State Science and Technology **6**, M3155 (2017)
36. Berencén, Y.; Mundet, B.; Rodríguez, J. A.; Montserrat, J.; Domínguez, C.; Garrido, B. **Hot electron engineering for boosting electroluminescence efficiencies of silicon-rich nitride light emitting devices** Journal of Luminescence **183**, 26 (2017)

37. Berencén, Y.; Prucnal, S.; Liu, F.; Skorupa, I.; Hübner, R.; Rebohle, L.; Zhou, S.; Schneider, H.; Helm, M.; Skorupa, W.
Room-temperature short-wavelength infrared Si photodetector
Scientific Reports **7**, 43688 (2017)
38. Berseneva, N.; Komsa, H.-P.; Vierimaa, V.; Björkman, T.; Fan, Z.; Harju, A.; Todorovic, M.; Krasheninnikov, A. V.; Nieminen, R. M.
Substitutional carbon doping of free-standing and Ru-supported BN sheets: A first-principles study
Journal of Physics: Condensed Matter **29**, 415301 (2017)
39. Bruchhaus, L.; Mazarov, P.; Bischoff, L.; Gierak, J.; Wieck, A. D.; Hövel, H.
Comparison of Technologies for Nano Device Prototyping with a Special Focus on Ion Beams - A review
Applied Physics Reviews **4**, 011302 (2017)
40. Bühler, J.; Schmidt, C.; Fischer, J.; Leitenstorfer, A.; Schneider, H.; Helm, M.; Pashkin, A.; Seletskiy, D. V.
Quantum Interference Controlled Current in InSb Injected by intense Terahertz Radiation
Journal of Infrared, Millimeter and Terahertz Waves **38**, 808 (2017)
41. Bürger, D.; Baunack, S.; Thomas, J.; Oswald, S.; Wendrock, H.; Rebohle, L.; Schumann, T.; Skorupa, W.; Blaschke, D.; Gemming, T.; Schmidt, O. G.; Schmidt, H.
Evidence for self-organized formation of logarithmic spirals during explosive crystallization of amorphous Ge:Mn layers
Journal of Applied Physics **121**, 184901 (2017)
42. Dell'Anna, R.; Masciullo, C.; Iacob, E.; Barozzi, M.; Giubertoni, D.; Böttger, R.; Cecchini, M.; Pepponi, G.
Multiscale structured germanium nanoripples as templates for bioactive surfaces
RSC Advances **7**, 9024 (2017)
43. Deßmann, N.; Pavlov, S. G.; Tsyplenkov, V. V.; Orlova, E. E.; Pohl, A.; Shastin, V. N.; Zhukavin, R. K.; Winnerl, S.; Mittendorff, M.; Klopf, J. M.; Abrosimov, N. V.; Schneider, H.; Hübers, H.-W.
Dynamics of non-equilibrium charge carriers in p-germanium doped by gallium
Physica Status Solidi (B) **254**, 1600803 (2017)
44. Dhal, S.; Chatterjee, S.; Facsko, S.; Möller, W.; Böttger, R.; Satpati, B.; Ratha, S.; Hübner, R.
Discrete Single Crystalline Titanium Oxide Nanoparticle Formation from a Two-Dimensional Nanowelded Network
Crystal Growth & Design **17**, 2660 (2017)
45. Förster, A.; Gemming, S.; Seifert, G.; Tománek, D.
Chemical and Electronic Repair Mechanism of Defects in MoS₂ Monolayers
ACS Nano **11**, 9989 (2017)
46. Förster, A.; Günther, F.; Gemming, S.; Seifert, G.
Influence of Electric Fields on the Electron Transport in Donor–Acceptor Polymers
Journal of Physical Chemistry C **121**, 3714 (2017)
47. Gago, R.; Prucnal, S.; Perez-Casero, R.; Caretti, I.; Jimenez, I.; Lungwitz, F.; Cornelius, S.
Structural impact of chromium incorporation in as-grown and flash-lamp-annealed sputter deposited titanium oxide films
Journal of Alloys and Compounds **729**, 438 (2017)
48. Ghorbani-Asl, M.; Kretschmer, S.; Spearot, D. E.; Krasheninnikov, A. V.
Two-dimensional MoS₂ under ion irradiation: from controlled defect production to electronic structure engineering
2D Materials **4**, 025078 (2017)
49. Gkogkou, D.; Shaykhtudinov, T.; Oates, T. W. H.; Gernert, U.; Schreiber, B.; Facsko, S.; Hildebrandt, P.; Weidinger, I. M.; Esser, N.; Hinrichs, K.
Characterization of anisotropically shaped silver nanoparticle arrays via spectroscopic ellipsometry supported by numerical optical modeling
Applied Surface Science **421**, 460 (2017)

50. Gokhan, U. C.; Acet, M.; Tekgul, A.; Farle, M.; Atakan, S.; Lindner, J.
The Production of Cu Nanoparticles on Large Area Graphene by Sputtering and in-Flight Sintering
Crystal Research and Technology **52**, 1700149 (2017)
51. Hashemi, A.; Komsa, H.-P.; Puska, M.; Krasheninnikov, A. V.
Vibrational properties of metal phosphorus trichalcogenides from first principles
Journal of Physical Chemistry C **121**, 27207 (2017)
52. Herbig, C.; Knispel, T.; Simon, S.; Schröder, U. A.; MartíNez-Galera, A. J.; Arman, M. A.; Teichert, C.; Knudsen, J.; Krasheninnikov, A. V.; Michely, T.
From Permeation to Cluster Arrays: Graphene on Ir(111) Exposed to Carbon Vapor
Nano Letters **17**, 3105 (2017)
53. Holland-Moritz, H.; Johannes, A.; Möller, W.; Ronning, C.
Addendum: Ion beam irradiation of nanostructures: sputtering, dopant incorporation, and dynamic annealing
Semiconductor Science and Technology **32**, 109401 (2017)
54. Janke, D.; Hulman, M.; Wenisch, R.; Gemming, S.; Rafaja, D.; Krause, M.
Influence of Nickel Catalyst Morphology on Layer-Exchange-Based Carbon Crystallisation of Ni/a-C Bilayers
Physica Status Solidi (B) **254**, 1700234 (2017)
55. Josten, E.; Wetterskog, E.; Glavic, A.; Boesecke, P.; Feoktystov, A.; Brauweiler-Reuters, E.; Rücker, U.; Salazar-Alvarez, G.; Brückel, T.; Bergström, L.
Superlattice growth and rearrangement during evaporation induced nanoparticle self-assembly
Scientific Reports **7**, 2802 (2017)
56. Karlušić, M.; Jakšić, M.; Lebius, H.; Ban-D'Etat, B.; Wilhelm, R. A.; Heller, R.; Schleberger, M.
Swift heavy ion track formation in SrTiO₃ and TiO₂ under random, channeling and near-channeling conditions
Journal of Physics D: Applied Physics **50**, 205302 (2017)
57. Kehr, S.; Doering, J.; Gensch, M.; Helm, M.; Eng, L. M.
FEL-Based Near-Field Infrared to THz Nanoscopy
Synchrotron Radiation News **30**, 31 (2017)
58. Kelling, J.; Ódor, G.; Gemming, S.
Suppressing correlations in massively parallel simulations of lattice models
Computer Physics Communications **220**, 205 (2017)
59. Kelling, J.; Ódor, G.; Gemming, S.
Local scale-invariance of the 2+1 dimensional Kardar-Parisi-Zhang model
Journal of Physics A **50**, 12LT01 (2017)
60. Kelling, J.; Zahn, P.; Schuster, J.; Gemming, S.
Elastic and Piezoresistive Properties of Nickel Carbides from First-Principles
Physical Review B **95**, 024113 (2017)
61. Khomenkova, L.; Lehninger, D.; Kondatenko, O.; Ponomaryov, S.; Gudymenko, O.; Tsybrii, Z.; Yukhymchuk, V.; Kladko, V.; von Borany, J.; Heitmann, J.
Effect of Ge content on the formation of Ge nanoclusters in magnetron-sputtered GeZrO_x-based structures
Nanoscale Research Letters **12**, 196 (2017)
62. Kirch, J. D.; Kim, H.; Boyle, C.; Chang, C.-C.; Mawst, L. J.; Lindberg Iii, D.; Earles, T.; Botez, D.; Helm, M.; von Borany, J.; Akhmadaliev, S.; Böttger, R.; Reyner, C.
Proton implantation for electrical insulation of the InGaAs/InAlAs superlattice material used in 8–15 μm-emitting quantum cascade lasers
Applied Physics Letters **110**, 082102 (2017)
63. Komsa, H.-P.; Krasheninnikov, A. V.
Engineering the Electronic Properties of Two-Dimensional Transition Metal Dichalcogenides by Introducing Mirror Twin Boundaries
Advanced Electronic Materials **3**, 1600468 (2017)

64. Komsa, H.-P.; Senga, R.; Suenaga, K.; Krasheninnikov, A. V.
Structural Distortions and Charge Density Waves in Iodine Chains Encapsulated inside Carbon Nanotubes
Nano Letters **17**, 3694 (2017)
65. König-Otto, J. C.; Wang, Y.; Belyanin, A.; Berger, C.; de Heer, W. A.; Orlita, M.; Pashkin, A.; Schneider, H.; Helm, M.; Winnerl, S.
Four-Wave Mixing in Landau-Quantized Graphene
Nano Letters **17**, 2184 (2017)
66. Krause, M.; Melkhanova, S.; Hübner, R.; Haluska, M.; Gemming, S.
Phase Transitions in C:Ni Nanocomposite Templates during Diameter-Selective CVD Synthesis of SWCNTs
Physica Status Solidi (B) **254**, 1700228 (2017)
67. Kretschmer, S.; Komsa, H.-P.; Bøggild, P.; Krasheninnikov, A. V.
Structural transformations in two-dimensional transition-metal dichalcogenide MoS₂ under electron beam: insights from first-principles calculations
Journal of Physical Chemistry Letters **8**, 3061 (2017)
68. Krzyszkowska, E.; Walkowiak-Kulikowska, J.; Stienen, S.; Wojcik, A.
Thionine-graphene oxide covalent hybrid and its interaction with light
Physical Chemistry Chemical Physics **19**, 14412 (2017)
69. Lehninger, D.; Rafaja, D.; Wünsche, J.; Schneider, F.; von Borany, J.; Heitmann, J.
Formation of orthorhombic (Zr,Ta)O₂ in thin Zr-Ta-O films
Applied Physics Letters **110**, 262903 (2017)
70. Liu, F.; Prucnal, S.; Berencén, Y.; Zhang, Z.; Yuan, Y.; Liu, Y.; Heller, R.; Böttger, R.; Rebohle, L.; Skorupa, W.; Helm, M.; Zhou, S.
Realizing the insulator-to-metal transition in Se-hyperdoped Si via non-equilibrium material processing
Journal of Physics D: Applied Physics **50**, 415102 (2017)
71. Macková, A.; Malinský, P.; Jagerová, A.; Sofer, Z.; Klímová, K.; Sedmidubský, D.; Mikulics, M.; Lorinčík, J.; Veselá, D.; Böttger, R.; Akhmadaliev, S.
Structural and optical properties of vanadium ion-implanted GaN
Nuclear Instruments and Methods in Physics Research B **406A**, 53 (2017)
72. Macková, A.; Malinský, P.; Jagerová, A.; Sofer, Z.; Klímová, K.; Sedmidubský, D.; Pristovsek, M.; Mikulics, M.; Lorinčík, J.; Böttger, R.; Akhmadaliev, S.
Structural and optical properties of Gd implanted GaN with various crystallographic orientations
Thin Solid Films **638**, 63 (2017)
73. Malic, E.; Winzer, T.; Wendler, F.; Brem, S.; Jago, R.; Knorr, A.; Mittendorff, M.; König-Otto, J. C.; Plötzing, T.; Neumaier, D.; Schneider, H.; Helm, M.; Winnerl, S.
Carrier Dynamics in Graphene: Ultrafast Many-Particle Phenomena
Annalen der Physik **529**, 170038 (2017)
74. Masciullo, C.; Dell'Anna, R.; Tonazzini, I.; Böttger, R.; Pepponi, G.; Cecchini, M.
Hierarchical thermoplastic rippled nanostructures regulate Schwann Cell adhesion, morphology and spatial organization
Nanoscale **9**, 14861 (2017)
75. Milowska, K.; Ghorbani-Asl, M.; Burda, M.; Wolanicka, L.; Catic, N.; Bristowe, P.; Koziol, K.
Breaking the Electrical Barrier between Copper and Carbon Nanotubes
Nanoscale **9**, 8458 (2017)
76. Nanda, G.; Hlawacek, G.; Goswami, S.; Watanabe, K.; Taniguchi, T.; Alkemade, P. F. A.
Electronic transport in helium-ion-beam etched encapsulated graphene nanoribbons
Carbon **119**, 419 (2017)

77. Nekić, N.; Sancho-Parramon, J.; Bogdanović-Radović, I.; Grenzer, J.; Hübner, R.; Bernstorff, S.; Ivanda, M.; Buljan, M.
Ge/Si core/shell quantum dots in alumina: Tuning the optical absorption by the core and shell size
Nanophotonics **6**, 1055 (2017)
78. Nguyen, L.; Komsa, H.-P.; Khestanova, E.; Kashtiban, R.; Peters, J. P.; Lawlor, S.; Sanchez, A. M.; Sloan, J.; Gorbachev, R.; Grigorieva, I.; Krasheninnikov, A. V.; Haigh, S. J.
Atomic defects and doping of monolayer NbSe₂
ACS Nano **11**, 2894 (2017)
79. Panzer, R.; Guhrenz, C.; Haubold, D.; Hübner, R.; Gaponik, N.; Eychmüller, A.; Weigand, J. J.
Versatile Tri(pyrazolyl)phosphanes as Phosphorus Precursors for the Synthesis of Highly Emitting InP/ZnS Quantum Dots - Tri(pyrazolyl)phosphane als Vorstufen für die Synthese von stark emittierenden InP/ZnS-Quantenpunkten
Angewandte Chemie - International Edition **56**, 14737 (2017)
80. Penkova, A. V.; Acquah, S. F. A.; Piotrovskiy, L. B.; Markelov, D.; Semisalova, A.; Kroto, H. W.
Fullerene Derivatives as Nano-Additives in Polymer Composites
Russian Chemical Reviews **86**, 530 (2017)
81. Piętka, B.; Bobrovska, N.; Stephan, D.; Teich, M.; Król, M.; Winnerl, S.; Pashkin, A.; Mirek, R.; Lekenta, K.; Morier-Genoud, F.; Schneider, H.; Deveaud, B.; Helm, M.; Matuszewski, M.; Szczytko, J.
Doubly dressed bosons: Exciton polaritons in a strong terahertz field
Physical Review Letters **119**, 077403 (2017)
82. Posselt, M.; Devaraj, M.; Schiwarth, M.
Influence of phonon and electron excitations on the free energy of defect clusters in solids: A first-principles study
Computational Materials Science **127**, 284 (2017)
83. Potzger, K.; Molholt, T. E.; Fenta, A. S.; Pereira, L. M. C.
Surface science using radioactive ions at ISOLDE: from metal surfaces to 2-dimensional materials
Journal of Physics G: Nuclear and Particle Physics **44**, 064001 (2017)
84. Prucnal, S.; Frigerio, J.; Napolitani, E.; Ballabio, A.; Berencén, Y.; Rebohle, L.; Wang, M.; Böttger, R.; Voelskow, M.; Isella, G.; Hübner, R.; Helm, M.; Zhou, S.; Skorupa, W.
In situ ohmic contact formation for n-type Ge via non-equilibrium processing
Semiconductor Science and Technology **32**, 115006 (2017)
85. Prucnal, S.; Rebohle, L.; Skorupa, W.
Doping by flash lamp annealing
Materials Science in Semiconductor Processing **62**, 115 (2017)
86. Prucnal, S.; Wu, J.; Berencen, Y.; Liedke, M. O.; Wagner, A.; Liu, F.; Wang, M.; Rebohle, L.; Zhou, S.; Cai, H.; Skorupa, W.
Engineering of optical and electrical properties of ZnO by non-equilibrium thermal processing: The role of zinc interstitials and zinc vacancies
Journal of Applied Physics **122**, 035303 (2017)
87. Ratajczak, R.; Mieszczynski, C.; Prucnal, S.; Guziewicz, E.; Stachowicz, M.; Snigurenko, D.; Gaca, J.; Böttger, R.; Wojcik, M.; Heller, R.; Skorupa, W.; Borany, J. V.; Turos, A.
Structural and optical studies of Pr implanted ZnO films subjected to a long-time or ultra-fast thermal annealing
Thin Solid Films **643**, 24 (2017)
88. Ratajczak, R.; Prucnal, S.; Guziewicz, E.; Mieszczynski, C.; Snigurenko, D.; Stachowicz, M.; Skorupa, W.; Turos, A.
The photoluminescence response to structural changes of Yb implanted ZnO crystals subjected to non-equilibrium processing
Journal of Applied Physics **121**, 075101 (2017)

89. Rebohle, L.; Wutzler, R.; Prucnal, S.; Hübner, R.; Georgiev, Y. M.; Erbe, A.; Böttger, R.; Glaser, M.; Lugstein, A.; Helm, M.; Skorupa, W.
Local formation of InAs nanocrystals in Si by masked ion implantation and flash lamp annealing
Physica Status Solidi (C) **14**, 1700188 (2017)
90. Röder, F.; Vogel, K.; Wolf, D.; Hellwig, O.; Wee, S. H.; Wicht, S.; Rellinghaus, B.
Model-based magnetization retrieval from holographic phase images
Ultramicroscopy **176**, 177 (2017)
91. Ruffenach, S.; Kadykov, A.; Rumyantsev, V. V.; Torres, J.; Coquillat, D.; But, D.; Krishtopenko, S. S.; Consejo, C.; Knap, W.; Winnerl, S.; Helm, M.; Fadeev, M. A.; Mikhailov, N. N.; Dvoretiskii, S. A.; Gavrilenko, V. I.; Morozov, S. V.; Teppe, F.
HgCdTe-based heterostructures for Terahertz photonics
APL Materials **5**, 035503 (2017)
92. Saini, C. P.; Barman, A.; Banerjee, D.; Grynko, O.; Prucnal, S.; Gupta, M.; Phase, D. M.; Sinha, A. K.; Kanjilal, D.; Skorupa, W.; Kanjilal, A.
Impact of Self-Trapped Excitons on Blue Photoluminescence in TiO₂ Nanorods on Chemically Etched Si Pyramids
Journal of Physical Chemistry C **121**, 11448 (2017)
93. Saravanan, K.; Jayalakshmi, G.; Panigrahi, B. K.; Hübner, R.
Strain and particle size analysis in ion beam synthesized SiC nanoparticles using Raman scattering studies
Crystal Research and Technology **52**, 1600391 (2017)
94. Schnepf, M. J.; Mayer, M.; Kuttner, C.; Tebbe, M.; Wolf, D.; Dulle, M.; Altantzis, T.; Formanek, P.; Förster, S.; Bals, S.; König, T. A. F.; Fery, A.
Nanorattles with tailored electric field enhancement
Nanoscale **9**, 9376 (2017)
95. Seifert, T.; Jaiswal, S.; Sajadi, M.; Jakob, G.; Winnerl, S.; Wolf, M.; Kläui, M.; Kampfrath, T.
Ultrabroadband single-cycle terahertz pulses with peak fields of 300 kV cm⁻¹ from a metallic spintronic emitter
Applied Physics Letters **110**, 252402 (2017)
96. Skorupa, W.; Schumann, T.; Rebohle, L.
Millisecond thermal processing using flash lamps for the advancement of thin layers and functional coatings
Surface & Coatings Technology **314**, 169 (2017)
97. Sutter, P.; Komsa, H.-P.; Krasheninnikov, A. V.; Huang, Y.; Sutter, E.
Luminescence of defects in the structural transformation of layered tin dichalcogenides
Applied Physics Letters **111**, 262102 (2017)
98. Tan, L. N.; Tan, Y.; Ghorbani-Asl, M.; Boettger, R.; Kretschmer, S.; Zhou, S. Q.; Huang, Z. Y.; Krasheninnikov, A. V.; Chen, F.
Tailoring Optical Properties of Atomically-Thin WS₂ via Ion Irradiation
Nanoscale **9**, 11027 (2017)
99. Tauchnitz, T.; Nurmamytov, T.; Hübner, R.; Engler, M.; Facsko, S.; Schneider, H.; Helm, M.; Dimakis, E.
Decoupling the two roles of Ga droplets in the self-catalyzed growth of GaAs nanowires on SiO_x/Si(111) substrates
Crystal Growth & Design **17**, 5276 (2017)
100. Tokel, O.; Turnalı, A.; Makey, G.; Elahi, P.; Çolakoğlu, T.; Ergeçen, E.; Yavuz, Ö.; Hübner, R.; Zolfaghari Borra, M.; Pavlov, I.; Bek, A.; Turan, R.; Koray Kesim, D.; Tozburun, S.; Ilday, S.; Ilday, F. Ö.
In-chip microstructures and photonic devices fabricated by nonlinear laser lithography deep inside silicon
Nature Photonics **11**, 639 (2017)
101. Tyschenko, I. E.; Cherkov, V. A.; Volodin, V. A.; Voelskow, M.
Specific Features of the Ion-Beam Synthesis of Ge Nanocrystals in SiO₂ Thin Films
Semiconductors **51**, 1240 (2017)

102. Vasin, A. V.; Rusavsky, A. V.; Kysil, D. V.; Prucnal, S.; Piryatinsky, Y.; Starik, S. P.; Nasieka, I.; Strelchuk, V. V.; Lysenko, V. S.; Nazarov, A. N.
The effect of deposition processing on structural and luminescent properties of a-SiOC: H thin films fabricated by RF-magnetron sputtering
Journal of Luminescence **191**, 102 (2017)
103. Vazquez, H.; Ahlgren, E. H.; Ochedowski, O.; Leino, A. A.; Mirzayev, R.; Kozubek, R.; Lebius, H.; Karlusic, M.; Jaksic, M.; Krasheninnikov, A. V.; Kotakoski, J.; Schleberger, M.; Nordlund, K.; Djurabekova, F.
Creating nanoporous graphene with swift heavy ions
Carbon **114**, 511 (2017)
104. Wendler, F.; Mittendorff, M.; König-Otto, J. C.; Brem, S.; Berger, C.; de Heer, W. A.; Böttger, R.; Schneider, H.; Helm, M.; Winnerl, S.; Malic, E.
Symmetry-Breaking Supercollisions in Landau-Quantized Graphene
Physical Review Letters **119**, 067405 (2017)
105. Winnerl, S.; Mittendorff, M.; König-Otto, J. C.; Schneider, H.; Helm, M.; Winzer, T.; Knorr, A.; Malic, E.
Ultrafast processes in graphene: from fundamental manybody interactions to device applications
Annalen der Physik **529**, 1700022 (2017)
106. Winzer, T.; Mittendorff, M.; Winnerl, S.; Mittenzwey, H.; Jago, R.; Helm, M.; Malic, E.; Knorr, A.
Unconventional double-banded saturation of optical transmission in graphene due to many-particle interactions
Nature Communications **8**, 15042 (2017)
107. Wutzler, R.; Rebohle, L.; Prucnal, S.; Grenzer, J.; Hübner, R.; Böttger, R.; Skorupa, W.; Helm, M.
Formation of $\text{In}_x\text{Ga}_{1-x}\text{As}$ nanocrystals in thin Si layers by ion implantation and flash lamp annealing
New Journal of Physics **19**, 063019 (2017)
108. Zhao, X.; Kotakoski, J.; Meyer, J. C.; Sutter, E.; Sutter, P.; Krasheninnikov, A. V.; Kaiser, U.; Zhou, W.
Engineering and modifying two-dimensional materials by electron beams
MRS Bulletin **42**, 667 (2017)
109. Zhukavin, R. K.; Kovalevskii, K. A.; Sergeev, S. M.; Choporova, Y. Y.; Gerasimov, V. V.; Tsyplenkov, V. V.; Knyazev, B. A.; Abrosimov, N. V.; Pavlov, S. G.; Shastin, V. N.; Schneider, H.; Deßmann, N.; Shevchenko, O. A.; Vinokurov, N. A.; Kulipanov, G. N.; Hübers, H.-W.
Low-temperature intracenter relaxation times of shallow donors in germanium
JETP Letters **106**, 571 (2017)

Other topics and external users of ion beam center and free-electron laser

110. Alarcon-Diez, V.; Vickridge, I.; Jakšić, M.; Grilj, V.; Schmidt, B.; Lange, H.
Charge Collection Efficiency in a segmented semiconductor detector interstrip region
Nuclear Instruments and Methods in Physics Research B **406**, 148 (2017)
111. Bakaev, A.; Terentyev, D.; Grigorev, P.; Posselt, M.; Zhurkin, E. E.
Ab initio study of interaction of helium with edge and screw dislocations in tungsten
Nuclear Instruments and Methods in Physics Research B **393**, 150 (2017)
112. Beck, M.; Klammer, M.; Rousseau, I.; Obergfell, M.; Leiderer, P.; Helm, M.; Kabanov, V. V.; Diamant, I.; Rabinowicz, A.; Dagan, Y.; Demsar, J.
Energy dependence of the electron-boson coupling strength in the electron-doped cuprate superconductor $\text{Pr}_{1.85}\text{Ce}_{0.15}\text{CuO}_{4-\delta}$
Physical Review B **95**, 085106 (2017)
113. Belianinov, A.; Burch, M. J.; Kim, S.; Tan, S.; Hlawacek, G.; Ovchinnikova, O.
Noble gas ion beams in materials science for future applications and devices
MRS Bulletin **42**, 660 (2017)

114. Berova, M.; Sandulov, M.; Tsvetkova, T.; Kitova, S.; Bischoff, L.; Böttger, R.
Ion Beam Induced Surface Modification of ta-C Thin Films
Acta Physica Polonica A **132**, 299 (2017)
115. Berova, M.; Sandulov, M.; Tsvetkova, T.; Szekeres, A.; Terziyska, P.; Kitova, S.; Böttger, R.; Bischoff, L.
Optical contrast formation in ta-C films by ion implantation
Revue Roumaine de Chimie **62**, 761 (2017)
116. Bonny, G.; Bakaev, A.; Olsson, P.; Domain, C.; Zhurkin, E. E.; Posselt, M.
Interatomic potential to study the formation of NiCr clusters in high Cr ferritic steels
Journal of Nuclear Materials **484**, 42 (2017)
117. Bracht, H.; Radek, M.; Posselt, M.; Liedke, B.; Schmidt, B.; Voelskow, M.; Bischoff, L.; Böttger, R.; Prucnal, S.; Hansen, J. L.; Larsen, A. N.; Bougeard, D.
Ion-Beam-Induced Atomic Mixing in Ge, Si, and SiGe, Studied by Means of Isotope Multilayer Structures
Materials **10**, 813 (2017)
118. Braun, M.; Georgiev, Y.; Schönherr, T.; Wilsenach, H.; Zuber, K.
A new precision measurement of the α -decay half-life of ^{190}Pt
Physics Letters B **768**, 317 (2017)
119. Cai, B.; Dianat, A.; Hübner, R.; Liu, W.; Wen, D.; Benad, A.; Sonntag, L.; Gemming, T.; Cuniberti, G.; Eychmüller, A.
Multimetallic Hierarchical Aerogels: Shape Engineering of the Building Blocks for Efficient Electrocatalysis
Advanced Materials **29**, 1605254 (2017)
120. Cajzl, J.; Nekvindová, P.; Mackova, A.; Malinský, P.; Sedmidubsky, D.; Hušák, M.; Remeš, Z.; Varga, M.; Kromka, A.; Böttger, R.; Oswald, J.
Erbium ion implantation into diamond – measurement and modelling of the crystal structure
Physical Chemistry Chemical Physics **19**, 6233 (2017)
121. Chen, C.; Akhmadaliev, S.; Romero, C.; de Aldana, J.; Zhou, S.; Chen, F.
Ridge Waveguides and Y-Branch Beam Splitters in KTiOAsO_4 Crystal by 15 MeV Oxygen Ion Implantation and Femtosecond Laser Ablation
Journal of Lightwave Technology **35**, 225 (2017)
122. Di Pietro, R.; Erdmann, T.; Carpenter, J. H.; Wang, N.; Shivhare, R. R.; Formanek, P.; Heintze, C.; Voit, B.; Neher, D.; Ade, H.; Kiriya, A.
Synthesis of High-Crystallinity DPP Polymers with Balanced Electron and Hole Mobility
Chemistry of Materials **29**, 10220 (2017)
123. Duan, B.; Heintze, C.; Bergner, F.; Ulbricht, A.; Akhmadaliev, S.; Oñorbe, E.; de Carlan, Y.; Wang, T.
The effect of the initial microstructure in terms of sink strength on the ion-irradiation-induced hardening of ODS alloys studied by nanoindentation
Journal of Nuclear Materials **495**, 118 (2017)
124. England, J.; Möller, W.; van den Berg, J. A.; Rossall, A.; Min, W. J.; Kim, J.
Combining dynamic modelling codes with medium energy ion scattering measurements to characterise plasma doping
Nuclear Instruments and Methods in Physics Research B **409**, 60 (2017)
125. Grinenko, V.; Materne, P.; Sarkar, R.; Luetkens, H.; Kihou, K.; Lee, C. H.; Akhmadaliev, S.; Efremov, D. V.; Drechsler, S.-L.; Klauss, H.-H.
Superconductivity with broken time-reversal symmetry in ion irradiated $\text{Ba}_{0.27}\text{K}_{0.73}\text{Fe}_2\text{As}_2$ single crystals
Physical Review B **95**, 214511 (2017)
126. Gruber, W.; Baehtz, C.; Geue, T.; Stahn, J.; Schmidt, H.
Isothermal differential dilatometry based on X-ray analysis applied to stress relaxation in thin ion-beam-sputtered Pt films
Journal of Materials Science **52**, 1647 (2017)

127. Günther, F.; Möbius, A.; Schreiber, M.
Structure optimisation by thermal cycling for the hydrophobic-polar lattice model of protein folding
European Physical Journal - Special Topics **226**, 639 (2017)
128. Gupta, P.; Becker, H.-W.; Williams, G. V. M.; Hübner, R.; Heinig, K.-H.; Markwitz, A.
Collision cascades enhanced hydrogen redistribution in cobalt implanted hydrogenated diamond-like carbon films
Nuclear Instruments and Methods in Physics Research B **394**, 6 (2017)
129. Gupta, P.; Williams, G. V. M.; Hübner, R.; Vajandar, S.; Osipowicz, T.; Heinig, K.-H.; Becker, H.-W.; Markwitz, A.
Self-assembly of magnetic nanoclusters in diamond-like carbon by diffusion processes enhanced by collision cascades
Applied Physics Letters **110**, 141901 (2017)
130. Gupta, P.; Williams, G. V. M.; Vajandar, S.; Osipowicz, T.; Becker, H.-W.; Heinig, K.-H.; Hübner, R.; Leveneur, J.; Kennedy, J.; Markwitz, A.
Positioning of cobalt atoms in amorphous carbon films by pre-selecting the hydrogen concentration
Nuclear Instruments and Methods in Physics Research B **409**, 116 (2017)
131. Haye, E.; Bruyère, S.; André, E.; Boulet, P.; Barrat, S.; Capon, F.; Miska, P.; Migot, S.; Carteret, C.; Coustel, R.; Gendarme, C.; Munnik, F.
LaFeO_xN_y perovskite thin films: Nitrogen location and its effect on morphological, optical and structural properties
Journal of Alloys and Compounds **724**, 74 (2017)
132. Henning, S.; Kühn, L.; Herranz, J.; Nachtegaal, M.; Hübner, R.; Werheid, M.; Eychmüller, A.; Schmidt, T. J.
Effect of Acid Washing on the Oxygen Reduction Reaction Activity of Pt-Cu Aerogel Catalysts
Electrochimica Acta **233**, 210 (2017)
133. Jang, J.; Friedrich, D.; Müller, S.; Lamers, M.; Hempel, H.; Lardhi, S.; Cao, Z.; Harb, M.; Cavallo, L.; Heller, R.; Eichberger, R.; van de Krol, R.; Abdi, F. F.
Enhancing Charge Carrier Lifetime in Metal Oxide Photoelectrodes through Mild Hydrogen Treatment
Advanced Energy Materials **7**, 1701536 (2017)
134. Karpov, Y.; Erdmann, T.; Stamm, M.; Lappan, U.; Guskova, O.; Malanin, M.; Raguzin, I.; Beryozkina, T.; Bakulev, V.; Günther, F.; Gemming, S.; Seifert, G.; Hamsch, M.; Mannsfeld, S.; Voit, B.; Kiriya, A.
Molecular Doping of a High Mobility Diketopyrrolopyrrole- Dithienylthieno[3,2-b]thiophene Donor-Acceptor Copolymer with F6TCNNQ
Macromolecules **50**, 914 (2017)
135. Koitzsch, A.; Habenicht, C.; Müller, E.; Knupfer, M.; Büchner, B.; Kretschmer, S.; Richter, M.; van den Brink, J.; Börrnert, F.; Nowak, D.; Isaeva, A.; Doert, T.
Nearest-neighbor Kitaev exchange blocked by charge order in electron-doped α -RuCl₃
Physical Review Materials **1**, 052001 (2017)
136. Kovalev, S.; Green, B.; Golz, T.; Maehrlin, S.; Stojanovic, N.; Fisher, A. S.; Kampfrath, T.; Gensch, M.
Probing ultra-fast processes with high dynamic range at 4th-generation light sources: arrival time and intensity binning at unprecedented repetition rates
Structural Dynamics **4**, 024301 (2017)
137. Lebedev, O. I.; Hébert, S.; Roddatis, V.; Martin, C.; Turner, S.; Krasheninnikov, A. V.; Grin, Y.; Maignan, A.
Revisiting hollandites: channels filling by main-group elements together with transition metals in Bi_{2-y}V_yV₈O₁₆
Chemistry of Materials **29**, 5558 (2017)

138. Legrand, M.; Preunkert, S.; Weller, R.; Zipf, L.; Elsässer, C.; Merchel, S.; Rugel, G.; Wagenbach, D. **Year-round record of bulk and size-segregated aerosol composition in central Antarctica (Concordia site) Part 2: Biogenic sulfur (sulfate and methanesulfonate) aerosol** *Atmospheric Chemistry and Physics* **17**, 14055 (2017)
139. Li, C.; Krauß, N.; Schäfer, G.; Ebner, L.; Kliebisch, O.; Schmidt, J.; Winnerl, S.; Hettich, M.; Dekorsy, T. **High-speed asynchronous optical sampling based on GHz Yb:KYW oscillators** *Optics Express* **25**, 9204 (2017)
140. Li, L.; Yuan, Y.; Qi, Y.; Wang, Q.; Zhou, S. **Achievement of a table-like magnetocaloric effect in the dual-phase ErZn₂/ErZn composite** *Materials Research Letters* **6**, 67 (2017)
141. Li, L.; Yuan, Y.; Xu, C.; Qi, Y.; Zhou, S. **Observation of large magnetocaloric effect in equiatomic binary compound ErZn** *AIP Advances* **7**, 056401 (2017)
142. Li, R.; Dong, N.; Cheng, C.; Ren, F.; Hübner, R.; Wang, J.; Zhou, S.; Chen, F. **Giant Enhancement of Nonlinear Optical Response in Nd:YAG Single Crystals by Embedded Silver Nanoparticles** *ACS Omega* **2**, 1279 (2017)
143. Linge, K. L.; Bédard, L. P.; Bugoi, R.; Enzweiler, J.; Jochum, K. P.; Kilian, R.; Jingao, L.; Marin-Carbone, J.; Merchel, S.; Munnik, F.; Morales, L. F. G.; Rollion-Bard, C.; Souders, A. K.; Sylvester, P. J.; Weis, U. **GGR Biennial Critical Review: Analytical Developments Since 2014** *Geostandards and Geoanalytical Research* **41**, 493 (2017)
144. Ma, L.; Tan, Y.; Wang, S.; Akhmadaliev, S.; Zhou, S.; Yu, H.; Zhang, H.; Chen, F. **Continuous-Wave and Q-Switched Yb:YSGG Waveguide Laser** *Journal of Lightwave Technology* **35**, 2642 (2017)
145. Nganou, C.; Lackner, G.; Teschome, B.; Deen, M. J.; Adir, N.; Pouhe, D.; Lupascu, D. C.; Mkandawire, M. **Energy Transfer Kinetics in Photosynthesis as an Inspiration for Improving Organic Solar Cells** *ACS Applied Materials and Interfaces* **9**, 19030 (2017)
146. Pilz, W.; Laufer, P.; Tajmar, M.; Böttger, R.; Bischoff, L. **Polyatomic Ions from Liquid Metal Ion Source driven High Current Ion Implanter** *Review of Scientific Instruments* **88**, 123302 (2017)
147. Prencipe, I.; Fuchs, J.; Pascarelli, S.; Schumacher, D. W.; Stephens, R. B.; Alexander, N. B.; Briggs, R.; Büscher, M.; Cernaianu, M. O.; Choukourov, A.; de Marco, M.; Erbe, A.; Fassbender, J.; Fiquet, G.; Fitzsimmons, P.; Gheorghiu, C.; Hund, J.; Huang, L. G.; Harmand, M.; Hartley, N.; Irman, A.; Kluge, T.; Konopkova, Z.; Kraft, S.; Kraus, D.; Leca, V.; Margarone, D.; Metzkes, J.; Nagai, K.; Nazarov, W.; Lutoslawski, P.; Papp, D.; Passoni, M.; Pelka, A.; Perin, J. P.; Schulz, J.; Smid, M.; Spindloe, C.; Steinke, S.; Torchio, R.; Vass, C.; Wiste, T.; Zaffino, R.; Zeil, K.; Tschentscher, T.; Schramm, U.; Cowan, T. E. **Targets for high repetition rate laser facilities: needs, challenges and perspectives** *High Power Laser Science and Engineering* **5**, e17 (2017)
148. Raja, N.; Murali, D.; Posselt, M.; Satyanarayana, S. V. M. **High Temperature Stability of BaZrO₃: An Ab Initio Thermodynamic Study** *Physica Status Solidi (B)* **255**, 1700398 (2017)
149. Richter, A.; Anwand, W.; Chen, C.-L.; Böttger, R. **Evaluation of defect formation in helium irradiated Y₂O₃ doped W-Ti alloys by positron annihilation and nanoindentation** *Journal of Nuclear Materials* **494**, 294 (2017)
150. Rosenwinkel, S.; Landgraf, A.; Korup, O.; Schwanghart, W.; Volkmer, F.; Dzhumabaeva, A.; Merchel, S.; Rugel, G.; Preusser, F. **Late Pleistocene outburst floods from Issyk Kul, Kyrgyzstan?** *Earth Surface Processes and Landforms* **42**, 1535 (2017)

151. Smith, T.; Hofmann, B. A.; Leya, I.; Merchel, S.; Pavetich, S.; Rugel, G.; Scharf, A.
The cosmic-ray exposure history of the Twannberg iron meteorite (IIG)
Meteoritics & Planetary Science **52**, 2241 (2017)
152. Song, W.; Lin, G.; Ge, J.; Fassbender, J.; Makarov, D.
Encoding micro-reactors with droplet chains in microfluidics
ACS Sensors **2**, 1839 (2017)
153. Su, Y.; Falgenhauer, J.; Leichtweiß, T.; Geiß, M.; Lupó, C.; Polity, A.; Zhou, S.; Obel, J.; Schlettwein, D.; Janek, J.; Meyer, B.
Electrochemical properties and optical transmission of high Li⁺ conducting LiSiPON electrolyte films
Physica Status Solidi (B) **254**, 1600088 (2017)
154. Ueda, M.; Silva, A. R.; Pillaca, E. J. D. M.; Mariano, S. F. M.; Rossi, J. O.; Oliveira, R. M.; Pichon, L.; Reuther, H.
New possibilities of plasma immersion ion implantation (PIII) and deposition (PIII&D) in industrial components using metal tube fixtures
Surface & Coatings Technology **312**, 37 (2017)
155. Švecová, B.; Vařák, P.; Vytkáčová, S.; Nekvindová, P.; Macková, A.; Malinský, P.; Böttger, R.
A study of the behaviour of copper in different types of silicate glasses implanted with Cu⁺ and O⁺ ions
Nuclear Instruments and Methods in Physics Research B **406**, 193 (2017)
156. von Albedyll, L.; Opel, T.; Fritzsche, D.; Merchel, S.; Laepple, T.; Rugel, G.
¹⁰Be in the Akademii Nauk ice core – first results for CE 1590-1950 and and implications for future chronology validation
Journal of Glaciology **63**, 514 (2017)
157. Wagner, A.; Anwand, W.; Attallah, A. G.; Dornberg, G.; Elsayed, M.; Enke, D.; Hussein, A. E. M.; Krause-Rehberg, R.; Liedke, M. O.; Potzger, K.; Trinh, T. T.
Positron Annihilation Lifetime Spectroscopy at a Superconducting Electron Accelerator
Journal of Physics: Conference Series **791**, 012004 (2017)
158. Wang, X. F.; Zhang, Z. T.; Wang, W. K.; Zhou, Y. H.; Kan, X. C.; Chen, X. L.; Gu, C. C.; Zhang, L.; Pi, L.; Yang, Z. R.; Zhang, Y. H.
Enhancement of superconductivity in FeSe thin crystals induced by biaxial compressive strain
Physica C **537**, 1 (2017)
159. Wilhelm, R. A.; Gruber, E.; Schwestka, J.; Kozubek, R.; Madeira, T. I.; Marques, J. P.; Kobus, J.; Krasheninnikov, A. V.; Schleberger, M.; Aumayr, F.
Interatomic coulombic decay - the mechanism for rapid deexcitation of hollow atoms
Physical Review Letters **119**, 103401 (2017)
160. Zhu, J. J.; Li, C. Q.; Jiang, K.; Zhang, P.; Tong, W. Y.; Liu, A. Y.; Shi, W. Z.; Liu, Y.; Huang, Y. P.; Li, W. W.; Hu, Z. G.
Higher wavenumber shift of Pb (Al_{1/2}Nb_{1/2})O₃ substitution in relaxor ferroelectric Pb(Zr_{0.52}Ti_{0.48})O₃-Pb(Zn_{1/3}Nb_{2/3})O₃ ceramics
Materials Letters **188**, 284 (2017)

Popular-science publications

161. Schultheiss, H.
Spins in Formation
Physik Journal **16** (09), 59 (2017)

Patents

1. Bali, R.; Kolesar, V.; Vazquez, M.
P1513 - Procedure and apparatus for measuring a d.c. magnetic field based on magnetostrictive effect in magnetic wires
EP3171189 - Offenlegung: 24.05.2017
2. Klingner, N.; Heller, R.; Hlawacek, G.; Facsko, S.; von Borany, J.; Wilhelm, R. A.
P1608 - Ionenmikroskopievorrichtung
DE102016112328 - Erteilung: 05.01.2017
3. Singh, A.; Winnerl, S.; Schneider, H.; Helm, M.
P1609 - THz-Antenne und Vorrichtung zum Senden und/oder Empfangen von THz-Strahlung
DE102016116900 - Erteilung: 02.08.2017, Nachanmeldungen: WO

Concluded scientific degrees

PhD theses

1. Bogusz, A.
Development of novel YMnO_3 -based memristive structures
TU Chemnitz, 23.08.2017
2. Klingner, N.
Ionenstrahlanalytik im Helium-Mikroskop
TU Dresden, 31.01.2017
3. Kopte, M.
Spin-orbit effects in asymmetrically sandwiched ferromagnetic thin films
TU Dresden, 16.11.2017
4. Langer, M.
Spin waves: the transition from a thin film to a full magnonic crystal
TU Dresden, 31.07.2017
5. Wensch, R.
In-situ and ex-situ investigation of transition metal catalyzed crystallization of carbon and silicon thin films
TU Chemnitz, 08.11.2017
6. Wutzler, R.
Integration of III-V compound nanocrystals in silicon via ion beam implantation and flash lamp annealing
TU Dresden, 26.09.2017
7. Yuan, Y.
The interplay between localization and magnetism in III-Mn-V dilute ferromagnetic semiconductors
TU Dresden, 23.10.2017

Bachelor/Master/Diploma theses

1. Koladi Mootheri, V.
Fabrication and electrical characterization of transistor structures based on ultrathin layers of indium selenide
TU Dresden, KU Leuven, 04.10.2017
2. Kruv, A.
Multifunctional flexible electronics on ultra-thin polymeric foils
TU Dresden, 21.09.2017
3. Leipoldt, J.
Optoelektronische Eigenschaften von Phosphor-hochdotierten und mittels Ionenstrahlsynthese und Blitzlampenausheilung hergestellten Germaniumverbindungen
TU BA Freiberg, 13.04.2017
4. Matthies, P.
Non-reciprocal behavior of spin waves in coupled layers
TU Dresden, 30.10.2017
5. Nurmamyrov, T.
Gallium-induced surface modification of SiO_x/Si(111) substrates for the subsequent growth of GaAs nanowires by molecular beam epitaxy
Universität Kiel, 06.03.2017
6. Pineda Gomez, R.
Fabrication and electrical characterization of electronic devices based on 2D materials
TU Dresden, KU Leuven, 04.10.2017
7. Strunck, T.
Untersuchung des Energieeintrags hochgeladener Ionen in ultradünnen Membranen
TU Dresden, 09.02.2017
8. Weinhold, T.
Magneto-optische Charakterisierung von Spinwellen-Autooszillationen
TU Dresden, 22.09.2017

Appointments and honors

Appointments

1. **Schultheiß, Helmut**

Head of the Emmy Noether Junior Research Group “Magnonics: Spin waves bridging Spintronics and Photonics” was appointed as **Chair** of the German Chapter of the IEEE Magnetics Society.

Awards and honors

1. **Schultheiß, Helmut**

Head of the Emmy Noether Junior Research Group “Magnonics: Spin waves bridging Spintronics and Photonics” received the **Walter Schottky Prize 2017** of the Deutsche Physikalische Gesellschaft (DPG) for „his fundamental research about understanding spin wave propagation in nanostructures and their application in new functional devices for transport and logic processing of information“.

2. **Hache, Toni**

Master student in the department “Magnetism” was announced as the **Georg Simon Ohm Laureate 2018** of the Deutsche Physikalische Gesellschaft (DPG) “... for the outstanding Master’s thesis ‘Preparation and Characterization of Spin-Hall Effect-based nano Microwave Oscillators’ within the course Nanotechnology“ at the Westsächsische Hochschule Zwickau. The prize was handed over at the DPG Spring Meeting in Erlangen in March 2018.

3. **Krasheninnikov, Arkady**

Head of the “Atomistic Simulations of Irradiation-induced Phenomena” group received the **HZDR Research Award 2017** “... for his theoretical analysis of defects in 2-dimensional materials”. In addition, he was announced as **Highly Cited Researcher 2017** by Clarivate Analytics, Philadelphia, PA, USA.

4. **Kosub, Tobias**

PhD student in the department “Magnetism” won the **HZDR PhD Award 2017** for his dissertation on “Ferromagnet-free magnetoelectric thin film elements”. Additionally, he received the **2nd Prize** of the **HZDR Innovation Competition 2017**.

5. **Chava, Phanish**

Master student in the department “Scaling Phenomena” received a **Cfaed Inspire Grant** by the Center for Advancing Electronics Dresden (cfaed) to collaborate with Dr. Quentin Smets at IMEC, Leuven, Belgium for a 6-months stay “Towards the fabrication of Tunnel Field Effect Transistors using 2-Dimensional Materials“.

6. **Xu, Xiaomo**

PhD student in the department “Ion Beam Center” was finalist of the **Graduate Student Award** at the AVS 64th International Symposium and Exhibition, Nanometer-Scale Science and Technology Division (NSTD), Tampa, FL, USA, 29.10. - 3.11.2017.

Invited conference contributions, colloquia, lectures and talks

Invited conference talks

1. Deac, A. M.
Ultrahigh anisotropy Heusler alloys for THz spin-torque oscillators
62nd Annual Conference on Magnetism and Magnetic Materials, 06.-10.11.2017, Pittsburgh, USA
2. Facsko, S.; Heinig, K. H.; Stegemann, K. H.; Pruefer, T.; Xu, X.; Hlawacek, G.; Huebner, R.; Wolf, D.; Bischoff, L.; Moeller, W.; von Borany, J.
Ion Beam-Enabled CMOS-Compatible Manufacturing of SETs Operating at Room Temperature
Ion-Surface Interactions 2017, 21.-25.08.2017, Moscow, Russia
3. Facsko, S.; Ou, X.; Engler, M.; Erb, D.; Skeren, T.; Bradley, R. M.
Nanoscale surface patterning of crystalline semiconductor surfaces by broad ion beam irradiation
MRS Fall Meeting, 26.11.-1.12.2017, Boston, USA
4. Facsko, S.; Ou, X.; Engler, M.; Erb, D.; Skeren, T.; Bradley, R. M.
Nanoscale surface patterning by non-equilibrium self-assembly of ion-induced vacancies and ad-atoms
20th International Conference on Surface Modification of Materials by Ion Beams, 09.-14.07.2017, Lisbon, Portugal
5. Facsko, S.; Wilhelm, R. A.; Gruber, E.; Heller, R.; Götzhäuser, A.; Beyer, A.; Turchanin, A.; Aumayr, F.
Nanomembranes Modified by Highly Charged Ions
Towards Reality in Nanoscale Materials IX, 13.-16.02.2017, Levi, Finland
6. Fassbender, J.
Ion Beam Modification of Magnetic Materials
International Conference on 'Accelerators in Materials and Medical Sciences' 2017, 05.-07.10.2017, Dubai, United Arab Emirates
7. Fassbender, J.
Nanomagnet fabrication by ion beams
Moscow International Symposium on Magnetism, 01.-05.07.2017, Moscow, Russia
8. Fowley, C.; Rode, K.; Gallardo, R.; Thiyagarajah, N.; Lau, Y.-C.; Borisov, K.; Betto, D.; Atcheson, G.; Kampert, E.; Wang, Z.; Lindner, J.; Coey, M.; Stamenov, P.; Deac, A. M.
Spin-transfer driven dynamics in hybrid structures
Moscow International Symposium on Magnetism, 01.-05.07.2017, Moscow, Russia
9. Gago, R.; Prucnal, S.; Palomares, J.; Jiménez, I.; Hübner, R.
Phase Formation and Selectivity on Cr (co-)Doped TiO₂+2082 through Interface Engineering and Post-Deposition Flash Lamp Annealing
2017 MRS Fall Meeting & Exhibit, 26.11.-01.12.2017, Boston, MA, USA
10. Georgiev, Y. M.
High Resolution Nanofabrication
5th International workshop "Nano-Fabrication, Devices & Metrology", 19.-20.06.2017, Eindhoven, The Netherlands
11. Gruber, E.; Wilhelm, R. A.; Petuya, R.; Smejkal, V.; Kozubek, R.; Hierzenberger, A.; Bayer, B. C.; Aldazabal, I.; Kazansky, A. K.; Libisch, F.; Krasheninnikov, A. V.; Schleberger, M.; Facsko, S.; Borisov, A. G.; Arnau, A.; Aumayr, F.
Ultrafast electronic response of graphene to a strong and localized electric field
Optical NanoSpectroscopy IV, 28.-31.03.2017, Lisbon, Portugal

12. Heinig, K.-H.; Prüfer, T.; Möller, W.; Hlawacek, G.; Xu, X.; Bischoff, L.; Hübner, R.; Wolf, D.; Facsko, S.; von Borany, J.
Ion-Beam-Induced Self-Organisation of Nanostructures at Interfaces
FOR3NANO: Formation of 3D Nanostructures by Ion Beams, 28.-30.06.2017, Helsinki, Finland
13. Helm, M.
THz spectroscopy of solids with a free electron laser
2nd German THz Conference, 29.-31.03.2017, Bochum, Germany
14. Helm, M.; König-Otto, J.; Schmidt, J.; Dimakis, E.; Winnerl, S.; Schneider, H.
Nonlinear THz spectroscopy of low-dimensional materials
MTSA 2017 & TeraNano-8, 19.-23.11.2017, Okayama, Japan
15. Hlawacek, G.
Nanofabrication with the Helium Ion Microscope
Chemistry for Electron-Induced Nanofabrication (CELINA), 15.09.2017, Porto, Portugal
16. Hlawacek, G.
Spatially controlled formation of nanostructures for magnetic and electronic applications
The Japan Society of Applied Physics (JASP) Autumn Meeting, 07.09.2017, Fukuoka, Japan
17. Hlawacek, G.
Structuring magnetic and electronic materials using GFIS noble gas focused beams
MRS Fall Meeting, 28.11.2017, Boston, USA
18. Hlawacek, G.; Klingner, N.; Heller, R.; Facsko, S.
Analytic approaches with focused ion beams
Meeting on Focused Ion Beams in Berlin (FIBiB), 06.11.2017, Berlin, Germany
19. Josten, E.; Glavic, A.; Meertens, D.; Wetterskog, E.; Bersgröm, L.; Brückel, T.; Lindner, J.
Magnetic nanomaterials
Jülich Center for Neutron Science (JCNS) Workshop 2017, 10.-13.10.2017, Tutzing, Germany
20. Klingner, N.; Heller, R.; Hlawacek, G.; Facsko, S.
SIMS on smallest scale
23-rd International Conference of Ion-Surface Interactions 2017, 21.-25.08.2017, Moscow, Russia
21. Klingner, N.; Heller, R.; Hlawacek, G.; Möller, W.; Facsko, S.
Nanoscale imaging and compositional analysis in the helium ion microscope
23rd International Conference on Ion Beam Analysis IBA-2017, 11.10.2017, Shanghai, China
22. Kosub, T.
Purely Antiferromagnetic Magnetoelectric Random Access Memory
Spin X Seminar Mainz/Kaiserslautern, 08.06.2017, Mainz, Germany
23. Krause, M.; Wensch, R.; Heras, I.; Lungwitz, F.; Janke, D.; Guillén, E.; Erbe, A.; Gemming, S.; Escobar Galindo, R.
New solar-selective CSP receiver coatings studied by environmental in situ methods
12th Pacific Rim Conference on Ceramic and Glass Technology including Glass & Optical Materials Division Meeting 2017, 21.-26.05.2017, Waikoloa, USA
24. Lenz, K.; Narkowicz, R.; Reiche, C. F.; Kákay, A.; Mühl, T.; Büchner, B.; Suter, D.; Lindner, J.; Fassbender, J.
Magnetization dynamics of a single Fe-filled carbon nanotube detected by ferromagnetic resonance
Intermag Europe 2017, IEEE International Magnetism Conference, 24.-28.04.2017, Dublin, Ireland
25. Liedke, M. O.; Bali, R.; Hübner, R.; Gradauskaitė, E.; Ehrler, J.; Wang, M.; Potzger, K.; Zhou, S.; Wagner, A.
Magnetic phase transitions in ns-laser irradiated FeAl systems: the role of open volume defects
The International Workshop on Positron Studies and Defects 2017 (PSD-17), 03.-08.09.2017, Dresden, Germany
26. Makarov, D.
ERC grant SMaRT at the Helmholtz-Zentrum Dresden-Rossendorf
Eastern Partnership PLUS Workshop "Science Connects", 15.05.2017, Kyiv, Ukraine

27. Makarov, D.
Flexible und ultradünne Magnetfeldsensorik
Science Match: Future Technologies, 26.01.2017, Dresden, Germany
28. Makarov, D.
Magnetic coupling phenomena in curved nanomagnets
Magnetic Coupling in Nanostructured Materials, 23.-25.10.2017, Rome, Italy
29. Makarov, D.
Flexible electronics: from interactive on-skin devices to in vivo applications
LII Zakopane School of Physics, 26.05.2017, Zakopane, Poland
30. Makarov, D.
Intelligent materials and devices
Special workshop at the Institute of Mathematics, National Academy of Sciences of Ukraine, 14.05.2017, Kyiv, Ukraine
31. Makarov, D.
Spintronics of thin film granular antiferromagnets
Workshop on antiferromagnetic spintronics, 25.-27.10.2017, Grenoble, France
32. Makarov, D.
Electronic proprioception
NanoBioSensor Conference, 04.-05.09.2017, Dresden, Germany
33. Makarov, D.
Flexible and ultrathin magnetic field sensorics
12. Silicon Saxony Day, 20.06.2017, Dresden, Germany
34. Menendez, E.; Surinach, S.; Baro, M. D.; Liedke, M. O.; Fassbender, J.; Nogues, J.; Sort, J.
Structure, composition and magnetism in FeAl alloys
Frontiers in Materials Processing Applications, Research and Technology, 09.-12.07.2017, Bordeaux, France
35. Nanda, G.; Hlawacek, G.; Goswami, S.; Watanabe, K.; Taniguchi, T.; Alkemade, P. F. A.
Electronic transport in helium-ion-beam etched encapsulated graphene nanoribbons
User Meeting Kleindiek, 25.-26.04.2017, Reutlingen, Germany
36. Otalora, J. A.; Lindner, J.; Schultheiss, H.; Hertel, R.; Thomas, A.; Nielsch, K.; Kákay, A.
Curvilinear magnonics
62nd Annual Conference on Magnetism and Magnetic Materials, 06.-10.11.2017, Pittsburgh, USA
37. Prucnal, S.
Doping of Ge via nonequilibrium processing
18th AGATA week and 2nd Position Sensitive Germanium Detectors and Application Workshop, 11.-15.09.2017, Milan, Italy
38. Prucnal, S.
Strategies for high doping of Ge
EMRS Fall Meeting 2017, 18.-21.09.2017, Warsaw, Poland
39. Rugel, G.; Akhmadaliev, S.; Belokonov, G.; Böttger, R.; von Borany, J.; Gutzmer, J.; Kaefer, P.; Meyer, M.; Noga, P.; Renno, A. D.; Scharf, A.; Tiessen, C. J.; Voigtländer, J.; Wagner, N.; Wiedenbeck, M.; Winter, A.; Wu, H. S.; Ziegenrücker, R.
Status report of Super-SIMS for resource technology
23rd International Conference on Ion Beam Analysis IBA-2017, 08.-13.10.2017, Shanghai, China
40. Schneider, H.; Schmidt, J.; Stephan, D.; Bhattacharyya, J.; Winnerl, S.; Dimakis, E.; Helm, M.
THz-spectroscopic studies on electron dynamics in a GaAs single quantum well and an InAs single quantum dot
14-th International Conference on Intersubband Transitions in Quantum Wells (ITQW2017), 10.-15.09.2017, Singapore, Singapore
41. Schultheiss, H.
Spins in Formation
DPG Frühjahrstagung, 22.3.2017, Dresden, Germany

42. Semisalova, A. S.; Bali, R.; Wintz, S.; Barton, C.; Thomson, T.; Hlawacek, G.; Fowley, C.; Ehrler, J.; Bottger, R.; Potzger, K.; Lindner, J.; Fassbender, J.
Structural disorder induced magnetization in FeAl and FeRh: The perspectives for laterally patterned magnetic metamaterials
META'17, The 8th International Conference on Metamaterials, Photonic Crystals and Plasmonics, 25.-28.07.2017, Incheon - Seoul, South Korea
43. Semisalova, A.; Stienen, S.; Barton, C. W.; Boettger, R.; Bali, R.; Thomson, T.; Farle, M.; Fassbender, J.; Potzger, K.; Lindner, J.
Ferromagnetic resonance in FeRh thin films near the antiferromagnetic-ferromagnetic phase transition
AMP 2017, Interdisciplinary workshop "Acousto-magneto-plasmonics meets quantum optics", 28.-30.06.2017, Versailles, France
44. Tauchnitz, T.; Balaghi, L.; Hübner, R.; Bischoff, L.; Schneider, H.; Helm, M.; Dimakis, E.
What Ga droplets can and cannot do in the growth of GaAs nanowires on Si
19th European Workshop on Molecular Beam Epitaxy, 19.-22.03.2017, Korobitsyno, St. Petersburg, Russia
45. Wagner, A.; Butterling, M.; Hirschmann, E.; Krause-Rehberg, R.; Liedke, M. O.; Potzger, K.
Positron Annihilation Studies using a Superconducting Electron LINAC
International Workshop on Positron Studies of Defects 2017 (PSD-17), 03.-08.09.2017, Dresden, Germany
46. Wagner, A.; Butterling, M.; Hirschmann, E.; Krause-Rehberg, R.; Liedke, M. O.; Potzger, K.
Positron Annihilation Studies using a Superconducting Electron LINAC
International Workshop on Physics with Positrons at Jefferson Lab, 12.-15.09.2017, Newport News, VA, USA
47. Wallner, A.; Kinoshita, N.; Feige, J.; Froehlich, M.; Hotchkis, M.; Paul, M.; Fifield, L. K.; Golser, R.; Honda, M.; Kivel, N.; Linnemann, U.; Matsuzaki, H.; Merchel, S.; Pavetich, S.; Rugel, G.; Schumann, D.; Tims, S. G.; Steier, P.; Winkler, S. R.; Yamagata, T.
Interstellar ⁶⁰Fe detected on Earth - but where is the r-process nuclide ²⁴⁴Pu?
14th International Conference on Accelerator Mass Spectrometry (AMS-14), 14.-18.08.2017, Ottawa, Canada
48. Wiesenhütter, K.; Skorupa, I.; Neubert, M.; Rebohle, L., Schmidt, H.
PolCarr® - intelligente Trägerlösungen für eine effektive Immobilisierung von Biomaterialien
Science Match: Future Technologies, 26.01.2017, Dresden, Germany
49. Wiesenhütter, K.; Skorupa, I.; Neubert, M.; Rebohle, L., Schmidt, H.
Fabrication of silicon BioChips with charge pattern and surface-near electrostatic forces
12. Silicon Saxony Day, 20.06.2017, Dresden, Germany
50. Wiesenhütter, K.; Skorupa, I.; Neubert, M.; Rebohle, L., Schmidt, H.
Fabrication of silicon BioChips with charge pattern and surface-near electrostatic forces
Jahrestagung der Biomedizinischen Technik und Dreiländertagung der Medizinischen Physik, 10.-13.09.2017, Dresden, Germany
51. Winnerl S.
Unusual Coulomb effects in graphene
Finite Systems in Nonequilibrium: From Quantum Quench to the Formation of Strong Correlations, 10.-30.09.2017, Natal, Brasil
52. Wintz, S.; Sluka, V.; Dieterle, G.; Weigand, M.; Tiberkevich, V.; Schneider, T.; Gallardo, R. A.; Finizio, S.; Erbe, A.; Lindner, J.; Schütz, G. A.; Slavin, A. N.; Raabe, J.; Fassbender, J.
Spin textures as local and tunable spin-wave emitters
62nd Annual Magnetism & Magnetic Materials Conference, 06.-10.11.2017, Pittsburgh, USA
53. Wintz, S.; Sluka, V.; Schneider, T.; Kakay, A.; Weigand, M.; Schultheiss, K.; Warnatz, T.; Mattheis, R.; Gallardo, R. A.; Roldan-Molina, A.; Landeros, P.; Tiberkevich, V.; Slavin, A.; Erbe, A.; Deac, A.; Lindner, J.; Fassbender, J.; Raabe, J.
Spin Wave Emission from Topological Spin Textures
Moscow International Symposium on Magnetism, 01.-05.07.2017, Moscow, Russia

Colloquia, lectures and talks (without conference talks)

54. Fassbender, J.
Ion beams for the creation of magnonic circuits
Magnonics - quo vadis?, 27.10.2017, Kaiserslautern, Germany
55. Froideval, A.
ESUO activities: an update
3rd Meeting of the European User Offices, 23.-24.10.2017, Lund, Sweden
56. Helm, M.
Nanoelectronics Research in Dresden
Kolloquium der Fakultät für Elektrotechnik und Informationstechnik, 05.05.2017, Vienna, Austria
57. Hlawacek, G.; Krasheninnikov, A.; Klingner, N.; Möller, W.; Munnik, F.; Facsko, S.
Scanning Transmission Ion Microscopy
npSCOPE Kick off meeting, 16.-17.01.2017, Belvaux, Luxembourg
58. Hlawacek, G.
Helium and Neon ion based microscopy and nanofabrication
Physik Kolloquium, 03.07.2017, Leoben, Austria
59. Kelling, J.
Efficient Parallel Monte-Carlo Simulations for Large-Scale Studies of Surface Growth Processes
Seminar Topical Problems, 14.06.2017, Chemnitz, Germany
60. Kelling, J.; Heinig, K. H.; Weigel, M.; Gemming, S.
GPU-Accelerated Kinetic Lattice Monte Carlo for Experimental-Scale Studies
TYC@Imperial, 16.10.2017, London, UK
61. Kretschmer, S.; Komsa, H.-P.; Bøggild, P.; Krasheninnikov, A. V.
Phase Transitions in Two-Dimensional Transition Metal Dichalcogenides under Electron Beam
Seminar, 15.-19.05.2017, Helsinki, Finland
62. Makarov, D.
Electronic proprioception
Invited talk at the Microsoft Applied Sciences Group, 04.12.2017, Redmond, USA
63. Osten, J.; Hula, T.; Wagner, K.; Henschke, A.; Lenz, K.; Schultheiss, H.; Lindner, J.; Fassbender, J.
The influence of local ion implantation on magnetic domains, magnetoresistance and spin wave propagation
Hard Condensed Matter Theory Seminar, 24.01.2017, Mainz, Germany
64. Schneider, H.
Terahertz spectroscopy of semiconductor nanostructures with a free-electron laser
Seminarvortrag, University of Wollongong, 02.03.2017, Wollongong, Australia
65. Schultheiss, H.
Spins in Formation
Kolloquium Walther Meissner Institut, 27.01.2017, Garching, Germany
66. Schultheiss, H.
Spins in Formation
Physikalisches Kolloquium TU Dresden, 13.06.2017, Dresden, Germany
67. Schultheiss, H.
Spins in Formation
Physikalisches Kolloquium TU Chemnitz, 15.11.2017, Chemnitz, Germany
68. Schultheiss, H.
Spins in Formation
SFB Seminar Uni Regensburg, 26.01.2017, Regensburg, Germany
69. Schultheiss, H.
Spins in Formation
Physikalisches Kolloquium Universität Augsburg, 27.11.2017, Augsburg, Germany

70. Skorupa, W.; Pelic, B.; Werner, H.; Eule, D.
Materialwissenschaftliche Untersuchungen für den Orgelbau: Von Bleigieß-Rezepten des 17. Jh. zu antikorrosiver Nanotechnologie
Eingeladener Seminarvortrag, 26.04.2017, Steinfurt, Germany
71. Wiesenhütter, K.; Skorupa, I.; Neubert, M.; Rebohle, L., Schmidt, H.
PolCarr® - smart carrier solutions for effective immobilization of biomaterials
Invited talk at the Thermo Fisher Scientific Innovation Day Europe, 11.05.2017, Darmstadt, Germany
72. Winnerl, S.
Teilchenphysik in Bleistiftstaub: das Wundermaterial Graphen
Seniorenakademie Dresden, 26.11.2017, Dresden, Germany

Conferences, workshops, colloquia and seminars

Organization of conferences and workshops

1. Azkona, I.; Endrino, J.L.; Escobar-Galindo, R.; Krause, M.
**“Surfaces, Coatings and Interfaces in Concentrated Solar Energy Applications”
Symposium at the MRS Spring Meeting**
17. – 21.04.2017, Phoenix, USA
2. Astakhov, G; Zhou, S.; Gali, A.
International Workshop on SiC defects for quantum technology
07. – 08.12.2017, Dresden, Germany
3. Bittencourt, C.; Ewels, C.; Foster, A.; Holmström, E.; Hynninen, T.; Krasheninnikov, A.; Nordlund, K.
Workshop “Towards Reality in Nanoscale Materials IX”
13. – 16.02.2017, Levi, Finland
4. Erbe, A.; Zahn, P.
NANONET Annual Workshop 2017
16. – 18.08.2017, Klingenberg, Germany
5. Facsko, S.; Heller, R.; Hlawacek, G.; Krasheninnikov, A.; Wilhelm, R. A.
22th International Workshop on Inelastic Ion Surface Collisions (IISC-22)
17. – 22.09.2017, Dresden, Germany
6. Hlawacek, G.
**Advanced ion microscopy focus topic (HI-FT) at the AVS (American Vacuum Society)
International Symposium & Exhibition**
29.10. – 03.11.2017, Tampa, USA
7. Hlawacek, G.
FIBiB: Focused Ion Beams in Berlin
06. – 07.11.2017, Berlin, Germany
8. Hübner, R.
5. Sächsisches TEM-Präparatorentreffen
06.04.2017, Dresden, Germany
9. Schramm, B.; Winnerl, S.; Pashkin, A.; Klopff, J. M.
First FELBE User Workshop
24. – 25.04.2017, Dresden, Germany
10. Sutter, P.; Alem, N.; Krasheninnikov, A.; Weber-Bargioni, A.
**“2D Materials—Macroscopic Perfection vs. Emerging Nanoscale Functionality”
Symposium at the MRS Spring Meeting**
17. – 21.04.2017, Phoenix, USA
11. Wilhelm, R.; Facsko, S.; Hlawacek, G.; Heller, R.; Krasheninnikov, A.
IISC 1st Summer School
13. – 15.09.2017, Dresden, Germany

Colloquia

1. Farle, Michael
University of Duisburg-Essen, Germany, and Immanuel Kant Baltic Federal University, Russia
Functionalized hybrid nanomagnets: New materials for innovations in energy storage and medical theranostics
27.11.2017
2. Fischer, Inga A.
Institute for Semiconductor Engineering/University of Stuttgart, Germany
Spin injection into Si and Ge with manganese-based ferromagnetic electrodes
02.11.2017
3. Hong, Minghwei
Department of Physics and Graduate Institute of Applied Physics/National Taiwan University
Scientific elegance of perfecting oxide/InGaAs and metal/InGaAs interfaces in pushing high-performance devices
23.11.2017
4. Jin, Xiaofeng
Fudan University, China
The Hall effects Edwin Hall never imagined
06.03.2017
5. Kaltenbrunner, Martin
Linz Institute of Technology, Department of Soft Matter Physics, Soft Electronics Laboratory, Johannes Kepler University, Austria
Soft Electronics
12.04.2017
6. Knoch, Joachim
Institute of Semiconductor Electronics, RWTH Aachen, Germany
Alternative for dopants in semiconducting field-effect transistors
11.05.2017
7. Liu, Kai
Experimental Condensed Matter Physics, Physics Department, UC Davis, USA
Nanomagnetic playground: Magnetic skyrmions, magneto-ionics and HAMR media
23.08.2017
8. Metzger, Robert
Molecular Electronics/Department of Chemistry, University of Alabama, USA
The smallest unimolecular rectifier, Coulomb blockades and other results
24.08.2017
9. Ohshima, Takeshi
Directorate National Institutes for Quantum and Radiological Science and Technology, Japan
Creation of color centers acting as single photon sources in silicon carbide using particle beams
12.06.2017
10. Patane, Amalia
University of Nottingham, UK
InSe rediscovered: A van der Waals crystal for electronics and optoelectronics
30.06.2017
11. Tegenkamp, Christoph
Institut für Physik/Technische Universität Chemnitz, Germany
Spin-charge transport phenomena on the atomic scale
09.11.2017
12. Yakobson, Boris
Department of Materials Science & NanoEngineering, Department of Chemistry, and the Richard E. Smalley Institute, Rice University, Houston, USA
Predictive modeling of 2D materials, synthesis to properties
27.07.2017

Seminars

1. Arrott, Anthony S.
Simon Fraser University, Canada
Visualization and interpretation of magnetic states based on the concept of magnetic charges
14.06.2017
2. Astakhov, Georgy
Universität Würzburg, Germany
Microwave, terahertz and optical spectroscopy of low dimensional quantum systems
10.03.2017
3. Awad, Ahmad
Physics Department, University of Gothenburg, Sweden
Long-range mutual synchronization of spin Hall nano-oscillators
28.02.2017
4. Bastard, Gérald
École Normale Supérieure, Paris, France
Impurities in semiconductor heterostructures
17.10.2017
5. Bauer, Peter
Johannes Kepler University, Linz, Austria
Fundamentals of ion-solid interaction and ion stopping
13.09.2017
6. Chang, Ching-Hao
IFW Dresden, Germany
Carrier driven magnetic coupling and anisotropy in ferromagnetic oxide heterostructures
26.06.2017
7. Eswara Moorthy, Santhana
Institute of Science and Technology (LIST), Advanced Instrumentation for Ion Nano-Analytics (AINA), Belvaux, Luxembourg
New in-situ techniques for correlative microscopy: TEM-SIMS and HIM-SIMS
16.11.2017
8. Forstner, Oliver
Friedrich-Schiller-Universität Jena und GSI Helmholtzzentrum für Schwerionenforschung, Germany
Laser interaction studies with negative and highly-charged positive ions
06.04.2017
9. Ganesh, Ramachandran
Institute of Mathematical Science, Chennai, India
Impurity induced current in Chern insulators
14.09.2017
10. Haglund, Richard
Vanderbilt University, USA
Tunable metasurfaces for switching and imaging using a metal-insulator transition
11.08.2017
11. Holland-Moritz, Henry
Friedrich-Schiller-Universität Jena, Germany
Ion-nanostructure interaction
10.03.2017
12. Iwase, Akihiro
Department of Materials Science, Osaka Prefecture University, Japan
Materials modifications and their analysis by using ion accelerators and synchrotron radiation facilities
30.06.2017

13. Jobst, Johannes
Huygens-Kamerlingh Onnes Laboratorium, Leiden Center for Ultramicroscopy (LCU), Leiden University, The Netherlands
Probing band structure and charge transport in two-dimensional materials with low-energy electron microscopy
15.12.2017
14. Kaiser, Andreas
Argonne National Laboratory, USA
Active micromagnets
29.03.2017
15. Kobus, Jacek
Instytut Fizyki, Uniwersytet Mikołaja Kopernika, Toruń, Poland
Finite difference Hartree-Fock method. Algorithm, implementation and application
27.09.2017
16. König, Dirk
Integrated Materials Design Centre, University of New South Wales/Australia and Chair of Nanotechnology, IMTEK, Albert Ludwigs University Freiburg, Germany
Modulation doping of Si nanostructures
15.06.2017
17. Kudrawiec, Robert
Wrocław University of Science and Technology, Poland
Electronic band structure and optical properties of highly mismatched alloys
26.10.2017
18. Michely, Thomas
University of Cologne, Germany
Ion beam damage in 2D materials
13.09.2017
19. Nastasi, Michael
University of Nebraska/Nebraska Center for Energy Science Research, USA
Ion beam mixing
14.09.2017
20. Nemeč, Hynek
Institute of Physics, Academy of Sciences of the Czech Republic
Linear and non-linear terahertz conductivity spectra of nanostructures
01.12.2017
21. Pétuya, Rémi
Institut des Sciences Analytiques et de Physico-Chimie pour l'Environnement (IPREM), France
Ultrafast electronic response of graphene to the strong and localized electric field of a slow highly charged ion-Time Dependent Density Functional Theory (TD-DFT) simulations
20.09.2017
22. Radek, Manuel
Universität Münster, Germany
Experimental and numerical investigations of atomic mixing in silicon, germanium, and their alloys
07.04.2017
23. Rensberg, Jura
Friedrich-Schiller-Universität Jena, Germany
Ion beam modification of phase transition materials – A method to turn VO₂ films into optical metasurfaces
26.10.2017
24. Schmidt, Matthias
UFZ Leipzig, Germany
Scanning electron and helium-ion microscopy at ProVIS - Centre for Chemical Microscopy
12.05.2017

25. Seiler, Martin
The National Laboratory for Age Determination NTNU Trondheim, Sweden
Developments at small AMS instruments
05.04.2017
26. Stier, Andreas
National High Magnetic Field Laboratory/Los Alamos National Laboratory, USA
Magneto-spectroscopy of 2D excitons in pulsed magnetic fields up to 65 Tesla
06.09.2017
27. Stolterfoht, Nikolaus
Helmholtz-Zentrum Berlin für Materialien und Energie, Germany
Guiding of highly charged ions through capillaries in insulating materials: milestones in experiments and simulations
03.05.2017
28. Teichert, Christian
Montanuniversität Leoben, Austria
Functionalizing 2D materials by organic molecules
02.05.2017
29. Tretiakov, Oleg
Tohoku University, Japan
Large curvature effects on ferromagnetic structures and skyrmions
25.09.2017
30. Turchanin, Andrey
Institut für Physikalische Chemie, Friedrich-Schiller-Universität Jena und Jena Center for Soft Matter (JCSM), Germany
Functional 2D materials via electron irradiation induced conversion of aromatic monolayers and thin films
04.05.2017
31. Urbánek, Michal
CEITEC - Central European Institute of Technology/Brno University of Technology, Czech Republic
Multicomponent magnonic crystals and waveguides with graded transitions
22.05.2017
32. Vandervorst, Wilfried
KU Leuven and imec, Belgium
Novel techniques in ion beam analysis (MEIS/LEIS/SIMS)
15.09.2017
33. Vantomme, André
KU Leuven, Belgium
Ion beam analysis of crystals - the channeling effect
13.09.2017
34. Vojta, Thomas
Missouri University of Science and Technology, USA
Quantum phase transitions and disorder - Griffiths singularities, infinite randomness, and smearing
04.12.2017
35. Wolff, Annalena
Queensland University of Technology, Australia
Helium Ion Microscopy: From ion solid interactions to real world applications at QUT
14.06.2017
36. Zingsem, Benjamin
University Duisburg-Essen, Faculty of Physics and Center for Nanointegration, Germany
Standing waves that won't stand still – Magneto-dynamic properties of chiral magnets
11.05.2017

Exchange of researchers

Guests at our institute

1. Bohovicova, J.
Bratislava University of Technology, Slovakia; 24.07. - 04.08.2017
2. Drozdziel, A.
University Lublin, Poland; 17.05. - 23.05.2017
3. El-Said, A. S.
Mansoura University, Egypt; 22.03. - 08.04.2017
4. Escobar Galindo, R.
Abengoa Research, Spain; 17.09. - 29.09.2017
5. Granell, P. N.
Universidad Nacional de San Martin, Argentina; 01.06. - 30.11.2017
6. Huang, K.
SIMIT Shanghai, P.R. China; 07.08. - 31.08.2017
7. Huang, X.
Nanjing University, P. R. China; 25.08.2017 - 24.08.2018
8. Iastremskyi, I.
Kyiv University, Ukraine; 10.08. - 30.08.2017
9. Kaleniuk, O.
Institute for Metal Physics, Kyiv, Ukraine; 07.12. - 19.12.2017
10. Liu, C.
Harbin Institute of Technology, P. R. China; 12.09.2017 - 11.09.2018
11. Madeira Amorim, T. I.
Universidade de Lisboa, Portugal; 01.01. - 30.09.2017
12. Martinez Reyes, A.
Universidad Autonoma de Mexico; 14.08. - 14.09.2017
13. Mesko, M.
Bratislava University of Technology, Slovakia; 24.07. - 04.08.2017
14. Nazarov, A.
Kyiv University, Ukraine; 04.06. - 11.06.2017
15. Ou, X.
SIMIT Shanghai, P. R. China; 10.08. - 09.09.2017
16. Özbey, D. H.
Ankara University, Turkey; 15.06. - 14.09.2017
17. Pedroso, D.
Instituto Tecnológico de Aeronautica, Sao Jose dos Campos, Brazil; 01.08.2017 - 31.07.2018
18. Pyeshkova, V.
Kyiv University, Ukraine; 04.09. - 16.09.2017
19. Pylypovskyi, O.
Kyiv University, Ukraine; 15.01. - 11.02.; 02.07. - 16.08.2017
20. Pyszniak, K.
University Lublin, Poland; 17.05. - 23.05.2017
21. Qi, J.
SIMIT Shanghai, P. R. China; 07.08. - 31.08.2017

22. Sheka, D.
Kyiv University, Ukraine; 14.01. - 12.02.; 02.07. - 30.08.2017
23. Sloika, M.
Kyiv University, Ukraine; 15.01. - 11.02.2017
24. Suvorov, O.
Institute for Metal Physics, Kyiv, Ukraine; 07.12. - 19.12.2017
25. Turek, M.
University Lublin, Poland; 17.05. - 23.05.2017
26. Vojta, T.
Missouri University of Science and Technology, Rolla, USA; 04.12. - 08.12.2017
27. Yershov, K.
Institute for Theoretical Physics, Kyiv, Ukraine; 02.07. - 08.07.2017
28. Zabala, Y.
Institute of Nuclear Physics, Krakow, Poland; 05.11. - 16.11.2017
29. Zhang, X.
Harbin Institute of Technology, P. R. China; 15.03.2017 - 14.03.2018
30. Zuk, J.
University Lublin, Poland; 06.11. - 10.11.2017

Projects

The projects are listed by funding institution and project starting date. In addition, the institute has several bilateral service collaborations with industrial partners and research institutions. These activities are not included in the following overview.

European Projects

- | | | | |
|----|-------------------------|--|---------------------------|
| 1. | 01/2015 – 12/2018 | European Union | EU |
| | | FRIENDS² – Engineering of New Durable Solar Surfaces | |
| | <i>Prof. S. Gemming</i> | <i>Phone: 0351 260 2470</i> | <i>s.gemming@hzdr.de</i> |
| 2. | 10/2015 – 12/2017 | European Union | EU |
| | | SMaRT – Shapeable Magnetolectronics (ERC Starting Grant) | |
| | <i>Dr. D. Makarov</i> | <i>Phone: 0351 260 3273</i> | <i>d.makarov@hzdr.de</i> |
| 3. | 01/2016 – 05/2017 | European Union | EU |
| | | CNTQC – Curved Nanomembranes for Topological Quantum Computation | |
| | <i>Dr. D. Makarov</i> | <i>Phone: 0351 260 3273</i> | <i>d.makarov@hzdr.de</i> |
| 4. | 02/2016 – 01/2020 | European Union | EU |
| | | IONS4SET – Single Electron Transistor | |
| | <i>Dr. J. v. Borany</i> | <i>Phone: 0351 260 3378</i> | <i>j.v.borany@hzdr.de</i> |
| 5. | 01/2017 – 12/2020 | European Union | EU |
| | | TRANSPIRE – Terahertz Radio Communication | |
| | <i>Dr. A. Deac</i> | <i>Phone: 0351 260 3709</i> | <i>a.deac@hzdr.de</i> |
| 6. | 01/2017 – 12/2020 | European Union | EU |
| | | npSCOPE – Nanoparticle Characterization | |
| | <i>Dr. G. Hlawacek</i> | <i>Phone: 0351 260 3409</i> | <i>g.hlawacek@hzdr.de</i> |
| 7. | 05/2017 – 04/2021 | European Union | EU |
| | | CALIPSOplus – Coordinated Access to Lightsources | |
| | <i>Prof. M. Helm</i> | <i>Phone: 0351 260 2260</i> | <i>m.helm@hzdr.de</i> |
| 8. | 09/2017 – 02/2019 | European Union | EU |
| | | Analytics – All-electrical analytic platform for digital fluidics | |
| | <i>Dr. D. Makarov</i> | <i>Phone: 0351 260 3273</i> | <i>d.makarov@hzdr.de</i> |

Helmholtz Association Projects

- | | | | |
|----|-------------------------|---|--------------------------|
| 1. | 10/2012 – 12/2020 | Helmholtz-Gemeinschaft | HGF |
| | | NANONET – International Helmholtz Research School on Nanoelectronics | |
| | <i>Dr. A. Erbe</i> | <i>Phone: 0351 260 2366</i> | <i>a.erbe@hzdr.de</i> |
| 2. | 01/2013 – 12/2019 | Helmholtz-Gemeinschaft | HGF |
| | | W3-Professorship TU Chemnitz | |
| | <i>Prof. S. Gemming</i> | <i>Phone: 0351 260 2470</i> | <i>s.gemming@hzdr.de</i> |
| 3. | 01/2014 – 12/2018 | Helmholtz-Gemeinschaft | HGF |
| | | Spintronics – Helmholtz Young Investigator Group | |
| | <i>Dr. A.M. Deac</i> | <i>Phone: 0351 260 3709</i> | <i>a.deac@hzdr.de</i> |
| 4. | 03/2014 – 02/2017 | Helmholtz-Gemeinschaft | HGF |
| | | Functional Materials – HGF Postdoc Dr. Yu Liu | |
| | <i>Prof. M. Helm</i> | <i>Phone: 0351 260 2260</i> | <i>m.helm@hzdr.de</i> |

5.	11/2014 – 12/2019	Helmholtz-Gemeinschaft	HGF
	Magnetism – HGF Postdoc Dr. K. Schultheiß		
	<i>Prof. J. Fassbender</i>	<i>Phone: 0351 260 3096</i>	<i>j.fassbender@hzdr.de</i>
6.	04/2016 – 03/2017	Helmholtz-Gemeinschaft	HGF
	Helmholtz-Enterprise-Fonds – GridLab		
	<i>Dr. H. Schultheiß</i>	<i>Phone: 0351 260 3243</i>	<i>h.schultheiss@hzdr.de</i>
7.	05/2016 – 04/2019	Helmholtz-Gemeinschaft	HGF
	THz Spectroscopy – HGF Postdoc Dr. A. Singh		
	<i>Prof. M. Helm</i>	<i>Phone: 0351 260 2260</i>	<i>m.helm@hzdr.de</i>
8.	10/2016 – 09/2017	Helmholtz-Gemeinschaft	HGF
	Helmholtz Exzellenznetzwerk – cfaed 1		
	<i>Dr. A. Erbe</i>	<i>Phone: 0351 260 2366</i>	<i>a.erbe@hzdr.de</i>
9.	10/2017 – 09/2018	Helmholtz-Gemeinschaft	HGF
	Helmholtz Exzellenznetzwerk – cfaed 2		
	<i>Dr. A. Erbe</i>	<i>Phone: 0351 260 2366</i>	<i>a.erbe@hzdr.de</i>
10.	10/2017 – 09/2019	Helmholtz-Gemeinschaft	HGF
	Helmholtz ERC Recognition Award		
	<i>Dr. H. Schultheiß</i>	<i>Phone: 0351 260 3243</i>	<i>h.schultheiss@hzdr.de</i>
11.	11/2017 – 10/2018	Helmholtz-Gemeinschaft	HGF
	Helmholtz Exzellenznetzwerk – DCM-MatDNA 2		
	<i>Prof. S. Gemming</i>	<i>Phone: 0351 260 2470</i>	<i>s.gemming@hzdr.de</i>

German Science Foundation Projects

1.	09/2012 – 06/2017	Deutsche Forschungsgemeinschaft	DFG
	ATOMIX – Atomic mixing in semiconductor layers		
	<i>Dr. M. Posselt</i>	<i>Phone: 0351 260 3279</i>	<i>m.posselt@hzdr.de</i>
2.	01/2013 – 12/2018	Deutsche Forschungsgemeinschaft	DFG
	Cluster of Excellence – Center for Advancing Electronics Dresden (cfaed)		
	<i>Prof. M. Helm</i>	<i>Phone: 0351 260 2260</i>	<i>m.helm@hzdr.de</i>
3.	01/2014 – 11/2017	Deutsche Forschungsgemeinschaft	DFG
	Relaxation dynamics in graphene		
	<i>Dr. S. Winnerl</i>	<i>Phone: 0351 260 3522</i>	<i>s.winnerl@hzdr.de</i>
4.	04/2014 – 08/2017	Deutsche Forschungsgemeinschaft	DFG
	Dynano – Spin wave excitations in periodic nanostructures		
	<i>Dr. K. Lenz</i>	<i>Phone: 0351 260 2435</i>	<i>k.lenz@hzdr.de</i>
5.	05/2014 – 04/2019	Deutsche Forschungsgemeinschaft	DFG
	Emmy Noether Junior Research Group – Magnonics		
	<i>Dr. H. Schultheiß</i>	<i>Phone: 0351 260 3243</i>	<i>h.schultheiss@hzdr.de</i>
6.	11/2014 – 05/2018	Deutsche Forschungsgemeinschaft	DFG
	Thermal spin-transfer torques		
	<i>Dr. J. Lindner</i>	<i>Phone: 0351 260 3221</i>	<i>j.lindner@hzdr.de</i>
	<i>Dr. A. M. Deac</i>	<i>Phone: 0351 260 3709</i>	<i>a.deac@hzdr.de</i>
7.	11/2014 – 08/2018	Deutsche Forschungsgemeinschaft	DFG
	All Optical Switching		
	<i>Dr. H. Schultheiß</i>	<i>Phone: 0351 260 3243</i>	<i>h.schultheiss@hzdr.de</i>
8.	10/2015 – 09/2018	Deutsche Forschungsgemeinschaft	DFG
	Ferromagnetic Silicon		
	<i>Dr. S. Zhou</i>	<i>Phone: 0351 260 2484</i>	<i>s.zhou@hzdr.de</i>

- | | | | |
|-----|------------------------------|---|---------------------------------|
| 9. | 03/2017 – 02/2020 | Deutsche Forschungsgemeinschaft | DFG |
| | | MUMAGI – Disorder induced magnetism | |
| | <i>Dr. R. Bali</i> | <i>Phone: 0351 260 2919</i> | <i>r.bali@hzdr.de</i> |
| 10. | 07/2017 – 06/2020 | Deutsche Forschungsgemeinschaft | DFG |
| | | HELEX2D – Interaction of highly charged ions with 2D materials | |
| | <i>Dr. R. Wilhelm</i> | <i>Phone: 0351 260 3378</i> | <i>r.wilhelm@hzdr.de</i> |
| 11. | 08/2017 – 07/2020 | Deutsche Forschungsgemeinschaft | DFG |
| | | FlexCom – Magnetic field sensitive flexible communication system | |
| | <i>Dr. D. Makarov</i> | <i>Phone: 0351 260 3273</i> | <i>d.makarov@hzdr.de</i> |
| 12. | 09/2017 – 08/2020 | Deutsche Forschungsgemeinschaft | DFG |
| | | Lane Formation | |
| | <i>Dr. A. Erbe</i> | <i>Phone: 0351 260 2366</i> | <i>a.erbe@hzdr.de</i> |
| 13. | 09/2017 – 08/2020 | Deutsche Forschungsgemeinschaft | DFG |
| | | Confined Microswimmers | |
| | <i>Dr. A. Erbe</i> | <i>Phone: 0351 260 2366</i> | <i>a.erbe@hzdr.de</i> |
| 14. | 11/2017 – 10/2020 | Deutsche Forschungsgemeinschaft | DFG |
| | | ULTRACRITICAL – High-temperature superconductors | |
| | <i>Dr. A. Pashkin</i> | <i>Phone: 0351 260 3287</i> | <i>o.pashkin@hzdr.de</i> |
| 15. | 11/2017 – 10/2020 | Deutsche Forschungsgemeinschaft | DFG |
| | | IMASTE – Graphene encapsulated quasi-2D materials | |
| | <i>Dr. A. Krasheninnikov</i> | <i>Phone: 0351 260 3148</i> | <i>a.krasheninnikov@hzdr.de</i> |

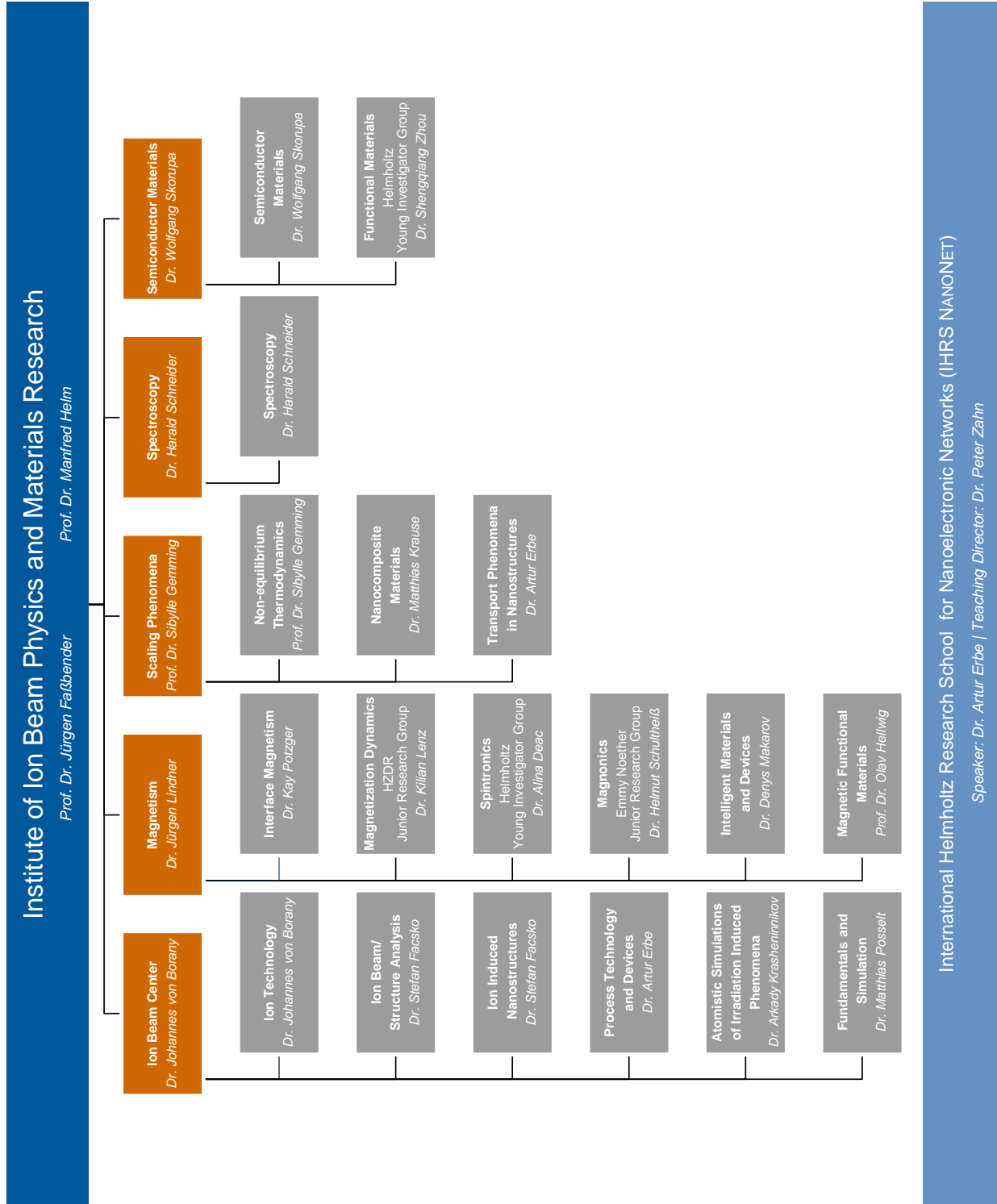
Federally and Saxony State Funded Projects

- | | | | |
|----|----------------------------|---|--------------------------------|
| 1. | 01/2014 – 06/2017 | Bundesministerium für Bildung und Forschung | BMBF |
| | | In-situ TEM | |
| | <i>Prof. J. Fassbender</i> | <i>Phone: 0351 260 3096</i> | <i>j.fassbender@hzdr.de</i> |
| 2. | 10/2014 – 09/2017 | Bundesministerium für Bildung und Forschung | BMBF |
| | | InTerFEL – High-Field Spectroscopy in the THz Regime | |
| | <i>Dr. H. Schneider</i> | <i>Phone: 0351 260 2880</i> | <i>h.schneider@hzdr.de</i> |
| 3. | 02/2016 – 12/2018 | Sächsische Aufbaubank | SAB |
| | | PolCarr-Sens – Electrically Polarizable Materials | |
| | <i>Dr. K. Wiesenhütter</i> | <i>Phone: 0351 260 3187</i> | <i>k.wiesenhuetter@hzdr.de</i> |
| 4. | 01/2017 – 06/2018 | Bundesministerium für Bildung und Forschung | BMBF |
| | | Elemental analytics with the Helium Ion Microscope | |
| | <i>Dr. R. Heller</i> | <i>Phone: 0351 260 3096</i> | <i>r.heller@hzdr.de</i> |
| 5. | 01/2017 – 06/2018 | Bundesministerium für Bildung und Forschung | BMBF |
| | | German-Ukrainian Center for Large Scale Experiment | |
| | <i>Dr. D. Makarov</i> | <i>Phone: 0351 260 3273</i> | <i>d.makarov@hzdr.de</i> |
| 6. | 08/2017 – 07/2019 | Sächsische Aufbaubank | SAB |
| | | PlatMOS – Plasma treatment of organ pipes | |
| | <i>Dr. W. Skorupa</i> | <i>Phone: 0351 260 3612</i> | <i>w.skorupa@hzdr.de</i> |
| 7. | 09/2017 – 08/2019 | Sächsische Aufbaubank | SAB |
| | | SiNergy – Si based battery electrodes | |
| | <i>Dr. S. Prucnal</i> | <i>Phone: 0351 260 2065</i> | <i>s.prucnal@hzdr.de</i> |
| 8. | 10/2017 – 03/2019 | Bundesministerium für Bildung und Forschung | BMBF |
| | | Resistance-Tensormeter | |
| | <i>Dr. T. Kosub</i> | <i>Phone: 0351 260 2900</i> | <i>t.kosub@hzdr.de</i> |
| 9. | 11/2017 – 12/2019 | Arbeitsgemeinschaft industrielle Forschung | AiF |
| | | Liquid metal ion source | |
| | <i>Dr. L. Bischoff</i> | <i>Phone: 0351 260 2866</i> | <i>l.bischoff@hzdr.de</i> |

Personnel Exchange Projects and Society Chairs

1. 01/2012 – 12/2018 Institute of Electrical and Electronics Engineers IEEE
Magnetics Society German Chapter Chair
Prof. J. Fassbender Phone: 0351 260 3096 j.fassbender@hzdr.de
2. 04/2015 – 03/2017 Deutscher Akademischer Austauschdienst DAAD
Personnel exchange with Chile – ChileConMagnon
Dr. K. Lenz Phone: 0351 260 2435 k.lenz@hzdr.de
3. 11/2015 – 04/2017 Deutscher Akademischer Austauschdienst DAAD
Visit of Dr. Zhu
Prof. M. Helm Phone: 0351 260 2260 m.helm@hzdr.de
4. 01/2016 – 12/2017 Deutscher Akademischer Austauschdienst DAAD
Personnel exchange with Poland – Magnetic Anisotropy
Dr. K. Potzger Phone: 0351 260 3244 k.potzger@hzdr.de
5. 01/2016 – 12/2017 Deutscher Akademischer Austauschdienst DAAD
Personnel exchange with Poland – BEGIN
Dr. S. Prucnal Phone: 0351 260 2065 s.prucnal@hzdr.de
6. 01/2016 – 12/2017 Deutscher Akademischer Austauschdienst DAAD
Personnel exchange with China – Semiconductors
Dr. S. Facsko Phone: 0351 260 2987 s.facsko@hzdr.de
7. 06/2016 – 05/2018 Alexander-von-Humboldt-Stiftung AvH
Humboldt fellowship Dr. Y. Berencen
Dr. L. Rebohle Phone: 0351 260 3368 l.rebohle@hzdr.de
8. 05/2017 – 07/2017 Deutscher Akademischer Austauschdienst DAAD
Visit of Prof. Subhankar
Dr. J. Lindner Phone: 0351 260 3221 j.lindner@hzdr.de
9. 06/2017 – 11/2017 Deutscher Akademischer Austauschdienst DAAD
Visit Dr. Granell
Dr. D. Makarov Phone: 0351 260 3273 d.makarov@hzdr.de
10. 06/2017 – 11/2017 Alexander-von-Humboldt-Stiftung AvH
Humboldt fellowship Prof. Sheka
Dr. D. Makarov Phone: 0351 260 3273 d.makarov@hzdr.de

Organization chart



List of personnel 2017

DIRECTORS		OFFICE
Prof. Dr. M. Helm, Prof. Dr. J. Faßbender		S. Gebel, S. Kirch
SCIENTIFIC STAFF		
Permanent staff	Non-permanent	
Dr. C. Akhmadaliev	Dr. R. Bali	Dr. A. Krasheninnikov
Dr. L. Bischoff	Dr. Y. Berencén (P)	Dr. M. Lenz
Dr. J. von Borany	Dr. R. Böttger	Dr. Y. Liu (P)
Dr. E. Dimakis	Dr. A. Deac	Dr. D. Makarov
Dr. A. Erbe	Dr. A. Eichler-Volf	Prof. Dr. W. Möller (P)
Dr. S. Facsko	Dr. H.-J. Engelmann (P)	Dr. I. Mönch (P)
Prof. Dr. S. Gemming	Dr. M. Engler	Dr. M. Neubert (P)
Dr. Y. Georgiev	Dr. D. Erb	Dr. N. Nishida (P)
Dr. J. Grenzer	Dr. L. Fallarino	Dr. J. Osten (P)
Dr. V. Heera	Dr. C. Fowley	Dr. P. Pandey (P)
Dr. R. Hübner	Dr. A. Froideval (P)	Dr. W. Pilz (P)
Dr. M. Krause	Dr. J. Ge (P)	Dr. R. Rana
Dr. K. Lenz	Dr. M. Ghorbani Asl	Dr. A. Scharf
Dr. J. Lindner	Dr. M. Grobosch (P)	Dr. H. Schultheiß (P)
Dr. F. Munnik	Dr. K.-H. Heinig (P)	Dr. K. Schultheiß (P)
Dr. A. Pashkin	Dr. R. Heller	Dr. A. Semisalova
Dr. M. Posselt	Prof. Dr. O. Hellwig	Dr. A. Singh (P)
Dr. K. Potzger	Dr. G. Hlawacek	Dr. S. Stienen
Dr. S. Prucnal	Dr. R. Illing	Dr. O. Volkov (P)
Dr. L. Rebohle	Dr. E. Josten	Dr. K. Wiesenhütter (P)
Dr. H. Schneider	Dr. J. Julin	Dr. R. Wilhelm
Dr. W. Skorupa	Dr. A. Kákay (P)	Dr. A. Wojcik (P)
Dr. M. Voelskow	R. Kaltofen (P)	Dr. D. Wolf (P)
Dr. S. Winnerl	Dr. N. Klingner (P)	Dr. O. Yildirim (P)
Dr. P. Zahn	Dr. T. Kosub	
Dr. S. Zhou		

(P) Projects

TECHNICAL STAFF**Permanent staff**

Rb. Aniol
 Rm. Aniol
 E. Christalle
 S. Eisenwinder
 B. Gebauer
 H. Gude
 D. Hanf
 J. Haufe
 A. Henschke
 H. Hilliges
 S. Klare
 J. Kreher
 A. Kunz

H. Lange
 U. Lucchesi
 F. Ludewig
 R. Mester
 Dr. R. Narkovic
 C. Neisser
 F. Nierobisch
 T. Putzke
 A. Reichel
 B. Scheumann
 G. Schnabel
 A. Schneider
 A. Scholz

Non-permanent

T. Schumann
 I. Skorupa
 M. Steinert
 A. Thiel
 K. Thiemig
 J. Wagner
 A. Weise
 A. Weißig
 J. Winkelmann
 L. Zimmermann
 J. Zscharschuch

L. Ehm
 A. Gerner
 S. Klengel
 T. Schönherr (P)
 I. Winkler
 A. Vetter
 T. Voitsekhivska (P)

PhD STUDENTS

H. Arora
 A. W. Awan
 N. Baghban Khojasteh
 L. Balaghi
 T. Bayrak
 J. Braun
 J. Buchriegler
 G.S.Canon Bermudez
 H. Cansever
 S. Creutzburg
 D. Deb
 J. Duan
 J. Ehrler

I. Fotev
 F. Fuchs
 S. Ghaderzadeh
 T. Hache
 D. Janke
 M. B. Khan
 F. Kilibarda
 N. Klingner
 J. König-Otto
 M. Kopte
 E. Kowalska
 S. Kretschmer
 D. Lang

M. Langer
 F. Liu
 F. Lungwitz
 T. Prüfer
 A. Schmeink
 J. Schmidt
 E. Schumann
 E. Serralta Hurtado
 Z. Shang
 M. Stöber
 A. Strobel
 T. Tauchnitz
 A. Titova

M. Vallinayagam
 T. Venanzi
 K. Wagner
 C. Wang
 M. Wang
 X. Wang
 Y. Xie
 C. Xu
 X. Xu
 Y. Yuan

STUDENTS (Diploma / MSc / BSc)

P. Chava
 J. Duan
 S. J. Ghamsari
 V. Joshi
 L. Koch
 V. Koladi Mootheri

A. Kruv
 J. Leipoldt
 V. Liersch
 P. Matthies
 M. Neumann
 T. Nurmamytov

R. Pineda Gomez
 L. Ramasubramanian
 R. Seifert
 S. Shan
 R. Sheldon
 N. Srinivasan

T. Strunck
 R. Thomas
 T. Weinhold

HZDR

 **HELMHOLTZ**
| ZENTRUM DRESDEN
| ROSSENDORF

Institute of Ion Beam Physics and Materials Research
Bautzner Landstrasse 400 · 01328 Dresden/Germany
Phone +49 351 260-2345
Fax +49 351 260-3285
<http://www.hzdr.de>

Member of the Helmholtz Association